The Effect of Entropy
on the Stability and Structure
of Complex Fluids

The Effect of Entropy
on the Stability and Structure
of Complex Fluids

Het effect van entropie
op de stabiliteit en de structuur
van complexe vloeistoffen
(met een samenvatting in het Nederlands)

Proefschrift

ter verkrijging van de graad van doctor aan de Universiteit Utrecht op gezag van de Rector Magnificus, Prof. dr. J.A. van Ginkel, ingevolge het besluit van het College van Decanen in het openbaar te verdedigen op maandag 12 september 1994 des namiddags te 4.15 uur

door

Marjolein Dijkstra

geboren op 26 september 1967 te 's-Gravenhage

Promotor :   Prof. dr. D. Frenkel

Faculteit der Scheikunde, Universiteit Utrecht en

FOM-Instituut voor Atoom- en Molecuulfysica te Amsterdam

CONTENTS

This thesis is based on the following papers:

Chapter 3: "Confinement Free Energy of Semiflexible Polymers",
M. Dijkstra, D. Frenkel and H.N.W. Lekkerkerker,
Physica A **193**, 374 (1993).

Chapter 4: "Simulation Study of a Two-Dimensional System of Semiflexible Polymers",
M. Dijkstra and D. Frenkel,
Phys. Rev. E, (1994) accepted for publication.

Chapter 5: M. Dijkstra and D. Frenkel,
to be published.

Chapter 6: "Evidence for Entropy-Driven Demixing in Hard-Core Fluids",
M. Dijkstra and D. Frenkel,
Phys. Rev. Lett. **72**, 298 (1994).

"Phase Separation in Binary Hard-Core Mixtures",
M. Dijkstra, D. Frenkel and J.P. Hansen,
J. Chem. Phys., (1994) accepted for publication.

Other publications to which the author of this thesis has contributed:

- "Velocity autocorrelation function in a four-dimensional lattice gas",
  M.A. van der Hoef, M. Dijkstra and D. Frenkel,
  Europhys. Lett. **17**, 39 (1992).

- "A Simple Lattice Model for the Mixing Properties of Molten
  $K_x(KCl)_{1-x}$ Solutions", M. Dijkstra, J.P. Hansen and A. Meroni,
  J. Phys.: Condens. Matter **6**, 2129 (1994).

1 GENERAL INTRODUCTION

This chapter gives a brief historical overview of statistical mechanics in the context of computer simulations of many-body systems. Particular attention is paid to the effect of entropy on the stability and structure of complex fluids, which is the subject of this thesis.

It is *impossible* to describe a macroscopic system, like a glass of water or a bar of metal, by solving the equations of motion of all individual molecules or atoms. In the 18th century, it was already known that the three-body problem could not be solved exactly and one liter of water under normal conditions consists of at least 10^{25} molecules. All we can do is to specify or to measure average properties of the system, like the temperature, density or magnetisation. This is exactly what statistical mechanics is concerned with. It attempts to predict the relations between the macroscopic properties of the system, if one only knows the microscopic forces between the individual components.

The basis for statistical mechanics as we know it, was laid in the second half of the nineteenth century, mainly through the pioneering work of Maxwell, Boltzmann, and Gibbs. In 1860, Maxwell proposed, besides his work on color blindness and the rings of Saturn, the distribution law of molecular velocities in statistical equilibrium [1, 2]. Boltzmann described the features of the energy distribution function in 1872 [3] and completed the so-called Maxwell-Boltzmann statistics for classical systems. The more general "ensemble theory" of statistical mechanics was subsequently developed by J.W. Gibbs. His papers were first published in the transactions of the Connecticut Academy of 1876 and 1879, but became generally known only after publication in German in 1902 [4]. In the nineteentwenties the classical Maxwell-Boltzmann statistics were

modified for quantum systems. In the summer of 1924, Einstein received a letter from Bose, an Indian physicist, on "the Hypothesis of Light Quanta". Einstein was very enthusiastic, because he saw immediately that it was possible to extend Bose's statistics to ordinary atoms. Einstein translated this letter in German and the Bose-Einstein statistics was established [5, 6]. The statistics for electrons was developed independently by Fermi and Dirac [7, 8] and is now called the Fermi-Dirac statistics. The ensemble theory can now be used for many quantum systems. Debye and Hückel applied statistical mechanics to electrolyte solutions in 1923 [9] and Langevin, Debye, Brillouin, Heisenberg, and others to dielectric and magnetic materials [10–13]. For liquids and dense gases, it was initiated by van der Waals in 1873 [14] and this work was followed by Ornstein, Zernike, Yvon, Kirkwood, Bogolyubov, Born, Green, and others [15–19]. In the forties Onsager used the theory for liquid crystals [20, 21] and application to polymer systems was first proposed by Kuhn and Flory [22–24].

How does one calculate now with the ensemble theory the thermodynamic or average properties of the system? The key quantity in statistical mechanics is the so-called partition function, which is a sum over all possible microstates of the system. If we consider a canonical ensemble, i.e., a system of N particles in a volume V at temperature T, which can be in several states s with energy $U(s)$, the partition function Z is

$$Z = \sum_s \exp(-U(s)/k_B T) \tag{1.1}$$

The sum is over all accessible states s of the system and k_B is Boltzmann's constant. The link with thermodynamics is now made through the relation:

$$F = -k_B T \log Z \tag{1.2}$$

where F is the Helmholtz free energy, i.e., the thermodynamic potential for a system with fixed values for N, V, and T. Note that this relation only holds in the thermodynamic limit, i.e., $N \to \infty$, $V \to \infty$ and $N/V = \rho$ remains fixed. The probability $P(s)$ of the system being in state s is

$$P(s) = \frac{1}{Z} \exp(-U(s)/k_B T) \tag{1.3}$$

The averaged thermodynamic value of a property A of the system is now given by

$$\langle A \rangle = \frac{1}{Z} \sum_s A(s) \exp(-U(s)/k_B T) \tag{1.4}$$

where $A(s)$ is its value in a state s. As we already know from thermodynamics, the observables can be obtained by differentiation of the thermodynamic potential [25]. For instance, the energy E can be calculated as follows

$$
\begin{aligned}
E &= \;<U> \\
&= \;\frac{1}{Z}\sum_s U(s)\exp(-U(s)/k_B T) \\
&= \;k_B T^2\frac{\partial \log Z}{\partial T} = (\frac{\partial F/T}{\partial 1/T})
\end{aligned} \tag{1.5}
$$

Thus when the sum-over-all-states or partition function is known, one can calculate all thermodynamic properties of the system simply by differentiation. Unfortunately, for a realistic system we almost never know this partition function. There are now several possibilities to proceed. We can either replace the system by a simpler, but less realistic one, for which we know the partition function exactly or we can approximate the partition function. In the early fifties, at the beginning of the computer era, another tool to study many-body systems became available, namely computer simulations.

In a computer simulation, we mimic the real world. We define a model for the system we like to study and we tell the computer the physical laws that should be satisfied. The computer calculates now how the system evolves in time. The thermodynamic observable can now directly be measured and averaged in time without knowing the partition function at all. There are two ways in which the system can evolve. The first simulation technique is called Monte Carlo (MC) simulation because of the extensive use of random numbers in the calculation. In a MC simulation we perform a random walk through configuration space in such a way that each state s of the system is visited with a probability that is proportional to its Boltzmann factor $\exp[-U(s)/k_B T]$ (see Eq. 1.3). The observables of the system can now be obtained by averaging its value over many configurations. However, the order of the states that are subsequently visited has no physical meaning and therefore a MC simulation does not yield dynamical information. A technique that does give dynamical properties is Molecular Dynamics (MD) simulations . A MD simulation follows the natural time evolution of a many-body system, as the equations of motion are solved numerically in discrete time steps for all particles. Hence, a MD simulation yields time-averaged quantities rather than ensemble-averages.

That computer simulations have indeed played an important role in the study of many-body systems can be illustrated by some examples. For a long time it was not clear what the causes are for freezing. Some people believed that repulsion between the particles was enough for a freezing transition, others thought that without attraction the system will not freeze. In 1957 Alder and Wood showed by computer simulations that a system with purely repulsive hard spheres has a well-defined freezing point [26, 27]. After a long discussion of 17 eminent physicists on the new results, the situation was not clearer at all. The idea arose to vote and the vote was evenly split [28]. Nowadays, it is

generally accepted that a hard sphere system has a fluid-solid transition. The reason for this transition will be explained below in more detail when we discuss the role of entropy in phase transitions. Another example of the role of computer simulations in statistical physics is the complete overhaul of the kinetic theory of dense fluids. For more than a hundred years it was generally believed that the collisions between the particles in a fluid were uncorrelated. The velocity autocorrelation function $\langle \mathbf{v}(t)\mathbf{v}(0) \rangle$ was expected to decay exponentially to zero. In 1970 Alder and Wainwright showed in their MD simulation a much slower decay of the velocity autocorrelation function in a fluid of hard disks and hard spheres [29]. The discovery of this algebraic decay stimulated the development of several theories that could explain this behaviour.

The examples mentioned above have shown that computer simulations are indeed able to test and verify old theories. And, if the theories seem to be incorrect, computer simulations can be a good guideline to improve the theories. Another application of computer simulations is that they can predict qualitatively or quantitatively the properties of new materials, without doing expensive or time-consuming experiments.

In this thesis, we exploit the fact that computer simulation is a convenient tool to study many-body problems. In particular, we study the effect of entropy on the stability and structure of complex fluids. Of course, from thermodynamics, we know that a phase transformation will take place in a system of N particles at constant volume and temperature T, if this results in lowering the Helmholtz free energy $F = E - TS$, where S is the entropy. There are two ways to lower the free energy of such a system: one is to lower the energy E, the other is to increase the entropy S. Most theories of fluids are based on the assumption that phase transitions that increase the visible order in a system result in a lowering of E and, at the same time, an increase of $-TS$. However, in this thesis we restrict ourselves to hard-core systems, i.e., systems in which the particles have only excluded volume interactions. Clearly, in this case, the potential energy of the system is always zero, as only configurations with non-overlapping particles have non-zero Boltzmann factors. A phase transition can then occur only if this results in an increase of the entropy. In order to understand how the entropy can be increased, we have to look at the statistical mechanical interpretation of entropy. Boltzmann's expression for the entropy of a system of N particles in a volume V and at an energy E is simply:

$$S = k_B \log \Omega \tag{1.6}$$

where Ω is the number of microstates accessible to the system. Thus the larger Ω, the less we know of the system: the system can be in any one of a large number of states. Our intuitive interpretation of entropy suggests now, that entropy is a measure for the amount

of disorder in the system. Usually, we call a crystal ordered and a fluid disordered and our intuitive interpretation of entropy suggests that a crystal has a lower entropy than the fluid. It was therefore a great surprise that in the fifties computer simulations showed a freezing transition in a fluid of hard spheres. This can only occur, if the entropy of the crystalline phase is higher than for the fluid phase, which is in conflict with our intuitive notion of entropy. But how can we then understand this freezing transition in a hard sphere system? In order to answer this question, we have to return to Boltzmann's definition of entropy (Eq. 1.6). If the entropy of the solid phase is higher than for the fluid phase, the number of microstates must be higher for the solid phase. A simple picture of a solid is that all the molecules are confined in cells centered around lattice sites. Confining molecules to cells results in a decrease in entropy. However, at sufficiently high density, the molecules in a dense fluid will be more jammed than in a solid, where the molecules can move freely within cells. This increase in free volume per molecule in a solid results in a gain in entropy (more microstates) that can outweigh the loss in entropy by confining the molecules to cells. When this occurs, entropy will induce crystallisation. It is now known that several phase transitions can be induced by entropy alone. An example of another entropy-driven phase transition was already given in the forties by Onsager [20, 21]. He showed that, on compression, a fluid of thin hard rods must undergo an orientational ordering transition. This so-called isotropic to nematic phase transition will be explained in more detail in chapter 2.

In this thesis, we study several entropy-driven phase transitions. In chapter 3, 4, and 5, we consider systems consisting of semiflexible polymers. A good and elegant theoretical description of these polymeric systems is hard to develop, as these systems are enormously complicated. Up to now, several theoretical approaches have been made. However, the basic assumptions of these theories have never been verified. It is therefore interesting to test these assumptions and the predictions of these theories in more detail by computer simulations. Another phenomenon, still not well understood, deals with the causes of phase separation in a binary mixture. In particular, it is still an unresolved question if demixing can be driven by entropic effects alone. It is therefore interesting, if we can settle this matter unambiguously by computer simulations. In chapter 6, we present the observation of a demixing transition in a hard-core mixture.

2 LIQUID CRYSTALS

In this chapter, we give a brief overview of liquid crystals. We describe Onsager's theory, that predicts an isotropic-nematic phase transition for rigid rods. Next, we discuss the theory of Khokhlov and Semenov for semiflexible polymers that provides an approximate description of the influence of molecular flexibility on the stability of these liquid crystalline phases.

2.1 Introduction

Although liquid crystals have been known since 1888, [30] they were initially only considered as a scientific curiosity. However, during the past few decades many important applications of liquid crystalline materials have been found. In particular, the fabrication of Liquid Crystal displays has developed into a multi-billion dollar industry. The term *liquid crystal* denotes a state that is intermediate between the crystalline solid (Fig. 2.1d) and the isotropic fluid phase (Fig. 2.1a). The essential requirement for the existence of these intermediate phases is a pronounced geometrical anisotropy of the molecules. In a liquid crystal, these asymmetric molecules are orientationally ordered, but long-range translational order is either absent or only partly present. To visualise this, we describe the two main liquid crystalline phases.

- The *nematic* phase is the simplest type. The molecules exhibit long-range orientational order, but do not show any long-range translational order (Fig. 2.1b), and hence the centers of mass of these molecules are randomly distributed.

- The *smectic* phase has a higher degree of order than the nematic phase. In addition to the long-range orientational order of the molecules, this phase has

a. isotropic phase   **b. nematic phase**

c. smectic phase   **d. solid phase**
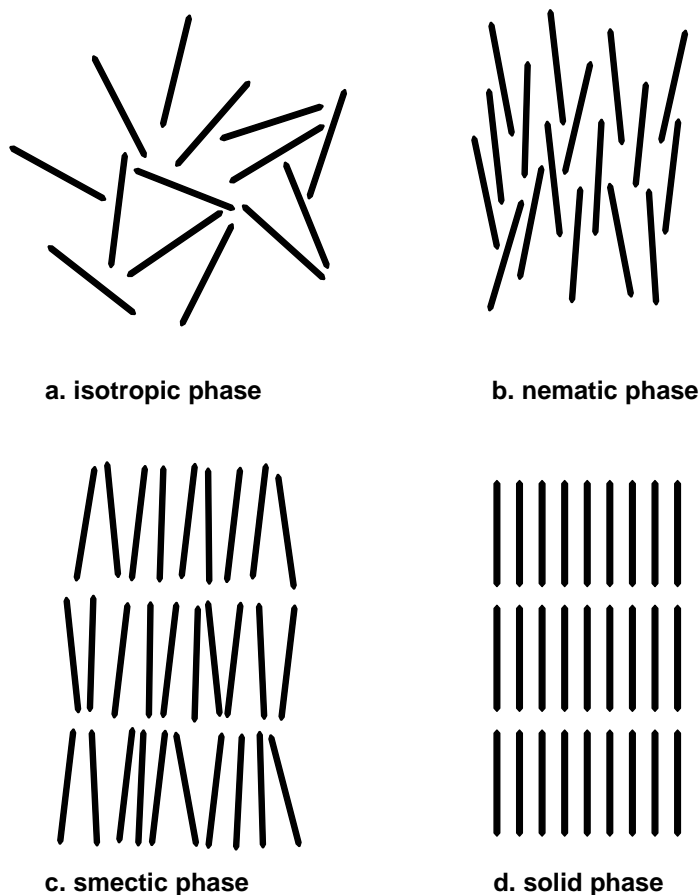
FIGURE 2.1   Schematic representation of the isotropic, nematic, smectic, and crystalline phases of rod-like molecules.

a stratified structure (like a crystal), but within each layer the molecules are randomly distributed (like a liquid) (Fig. 2.1c). The smectic phase can therefore be considered as a one-dimensional crystal and a two-dimensional liquid.

Because of the anisotropy of these phases, these compounds have peculiar light scattering and dielectric properties and can therefore be used in device applications such as displays. This is one of the reasons of the upsurge in interest in liquid crystals. But they are also of considerable interest because of the unique phases and phase transitions that they exhibit [31].

The statistical mechanical theory of phase transitions of liquid crystals starts with the seminal work of Onsager [20, 21], who showed that infinitely thin hard rods have an entropy-induced isotropic-nematic phase transition above a certain concentration.

The phase behaviour of such infinitely thin hard rods can be solved essentially exactly [20, 21]. However, for particles with a finite length-to-width ratio, no such exact solution are possible and computer simulations were essential to elucidate the phase behaviour. These simulations confirmed that liquid crystalline behaviour can be obtained in systems of rod-like particles without the inclusion of attractive interactions [32–41]. One important limitation of the original Onsager theory was that it applied only to rigid particles. The extension to semiflexible rod-like molecules has been presented by Khokhlov and Semenov [42, 43]. The Onsager theory, as well as the extension by Khokhlov and Semenov will be discussed below. Most simulations of liquid crystal formation in systems of hard particles were similarly limited to rigid molecules. In this thesis, we present a computational scheme to simulate semiflexible polymers: This allows us to study by computer simulation the influence of flexibility on liquid crystal formation.

2.2 Virial Expansion of the Free Energy of Rod-like Particles

We have already mentioned that the non-spherical shape of molecules is an essential factor for the existence of liquid crystalline phases. In this section, we consider a fluid consisting of long hard rods, which are impenetrable to each other. In the previous chapter, we concluded that in a hard-core system phase transitions can only occur if this results in an increase of the entropy. At first sight, it may seem strange that a system of hard rods can increase its entropy by going from a disordered fluid phase to an orientationally ordered nematic phase. However, at sufficiently high density, a molecule in the aligned phase has more free volume than in an isotropic phase, where the particles are strongly hindered by the other molecules. Due to the increase in available space per rod, the system gains translational entropy, that outweighs the loss in orientational entropy by confining the orientations of the rods. Thus, at low densities, the molecules can point in all possible directions and the fluid will be isotropic. If the density increases, it will be unfavourable for the molecules to have random orientations and the molecules align along one direction. Below, we describe the Onsager theory in some detail.

We start with the virial expansion in the density ρ of the Helmholtz free energy ΔF for a gas of N particles.

$$\frac{\Delta F}{Nk_BT} = \log(\Lambda^3 \rho) - 1 + B_2\rho + \frac{1}{2}B_3\rho^2 + \cdots \tag{2.1}$$

where T is the absolute temperature, Λ equals $\sqrt{h^2/2\pi mk_BT}$, h is Planck's constant

and $\log(\Lambda^3\rho) - 1$ the ideal gas term. The subsequent terms are the two-, three-, and more particle interactions that can be seen as corrections to the ideal gas term. The virial coefficients B_n are proportional to the irreducible cluster integrals of the Mayer functions Φ_{12} [44]:

$$\Phi_{12} = \exp(-\beta u_{12}) - 1 \tag{2.2}$$

where β is the inverse temperature, i.e., $1/k_B T$ and u_{12} is the two-body potential. Higher-body potentials are absent for hard-core particles. The second and third virial coefficients contain, respectively, interactions between two particles and three particles and can be obtained by integration of the Mayer functions over all possible coordinates of the particles.

$$
\begin{aligned}
B_2 &= -\frac{1}{2V} \iint \Phi_{12} d\mathbf{r}_1 d\mathbf{r}_2 \\
B_3 &= -\frac{1}{3V} \iiint \Phi_{12}\Phi_{23}\Phi_{31} d\mathbf{r}_1 d\mathbf{r}_2 d\mathbf{r}_3
\end{aligned}
\tag{2.3}
$$

For a derivation of the virial expansion, the reader is referred to a standard textbook on statistical mechanics [44, 45]. Onsager discovered, inspired by the discovery of liquid crystalline phases in solutions of TMV (Tobacco Mosaic Virus) [46], that this virial expansion could be used to predict the isotropic-nematic phase transition in solutions of rod-like particles. He assumed that particles of different orientations could be regarded as particles of different species.

For a mixture of n different gases with number fractions x_i and $\sum_{i=1}^{n} x_i = 1$, an extra term appears in the expression of the Helmholtz free energy, that stems from the entropy of mixing. The partition function for the ideal mixture is

$$Z = \frac{V^N}{\Lambda^{3N} N_1! N_2! \cdots N_n!} \tag{2.4}$$

where $N_i = x_i N$ the number of particle of species i. Using Stirling's formula, we find the following free energy expression

$$F = N k_B T \left[\log(\Lambda^3\rho) - 1 + \sum_{i=1}^{n} x_i \log x_i \right] \tag{2.5}$$

The last term in this expression is the entropy of mixing. The virial expression for a mixture of n different gases is now similar to the virial expansion for the gas:

$$\frac{\Delta F}{N k_B T} = \log(\Lambda^3\rho) - 1 + \sum_{i=1}^{n} x_i \log x_i + B_2\rho + \frac{1}{2}B_3\rho^2 + \cdots \tag{2.6}$$

However the virial coefficients are now more complicated, as we have different cluster integrals for various possible combinations of particles. For instance, the second virial coefficient reads

$$B_2 = -\frac{1}{2V} \sum_{i,j=1}^{n} x_i x_j \iint \Phi_{12}(i,j) d\mathbf{r}_1 \, d\mathbf{r}_2 \tag{2.7}$$

Note that the Mayer function is now dependent on type i and j of the particles. The next step is to identify mole fraction x_i with the fraction of the molecules that have an orientation within a solid angle $d\Omega_i$ around Ω_i. If we denote the orientational probability density by $f(\Omega)$, then we can make the identification $x_i \leftrightarrow f(\Omega_i)d\Omega_i$. Thus with $\int f(\Omega)d\Omega = 1$, we get

$$
\begin{aligned}
\frac{\Delta F}{N k_B T} &= \log(\Lambda^3 \rho) - 1 + \int f(\Omega)\log(4\pi f(\Omega))d\Omega + B_2\rho + \\
&\quad \frac{1}{2}B_3\rho^2 + \cdots
\end{aligned}
\tag{2.8}
$$

with

$$B_2 = -\frac{1}{2V} \iint f(\Omega)f(\Omega') \left[\iint \Phi_{12}(\mathbf{r}_1, \mathbf{r}_2; \Omega, \Omega')d\mathbf{r}_1 d\mathbf{r}_2 \right] d\Omega d\Omega' \tag{2.9}$$

The factor 4π in $\int f(\Omega)\log(4\pi f(\Omega))d\Omega$ is introduced for convenience to make this orientational entropy zero for an isotropic distribution, where $f(\Omega) = 1/4\pi$.

Onsager truncated the virial expansion after the second virial term. He made it plausible that this approximation is exact for infinitely long rods ($L \gg D$). For hard particles the Mayer functions are simple

$$
\begin{aligned}
u_{12} = \infty &\rightarrow \Phi_{12} = -1 \quad \text{for overlapping particles} \\
u_{12} = 0 &\rightarrow \Phi_{12} = 0 \quad \text{for non-overlapping particles}
\end{aligned}
\tag{2.10}
$$

With these values for Φ_{12}, we find that the integral between square brackets in Eq. 2.9 is related to the negative of the orientation dependent excluded volume. For two rods of length L, diameter D, and at an angle γ, this integral becomes for $L \gg D$ (Fig. 2.2)

$$\frac{1}{V} \iint \Phi_{12}(\mathbf{r}_1, \mathbf{r}_2; \Omega, \Omega')d\mathbf{r}_1 d\mathbf{r}_2 = -2L^2 D \, |\sin\gamma| \tag{2.11}$$
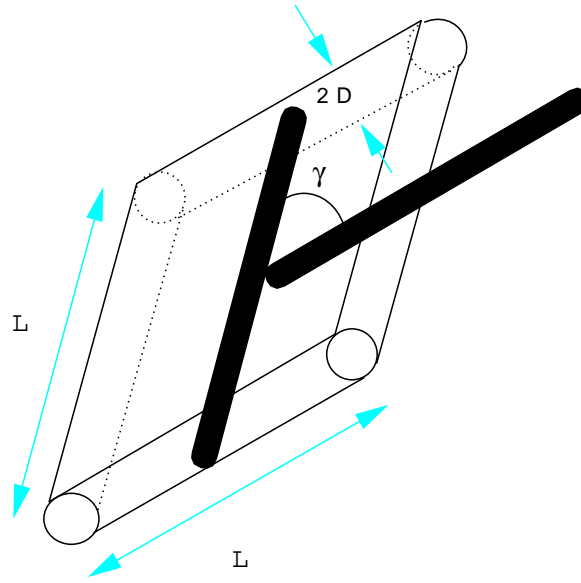
FIGURE 2.2   Excluded volume of two hard rods of diameter D, length L, and at an angle γ.

The expression for the Helmholtz free energy reads now in the Onsager approximation

$$
\frac{\Delta F}{N k_B T} = \log(\Lambda^3 \rho) - 1 + \int f(\Omega) \log(4\pi f(\Omega)) d\Omega
$$

$$
+ \rho L^2 D \int f(\Omega) f(\Omega') |\sin \gamma| \, d\Omega d\Omega' \tag{2.12}
$$

We see now that two rods hinder each other more, i.e., exclude more volume for each other, at large mutual angles γ. The excluded volume interactions can therefore be minimised by means of alignment. On the other hand the orientational entropy favours an isotropic distribution. If we consider the competition between these two opposing effects, we can argue that above a certain density the gain in translational entropy, due to alignment outweighs the resulting loss in orientational entropy. When this happens a nematic phase will be formed.

2.3   Free Energy of Partially Flexible Chains

In reality, most long particles possess some degree of flexibility. It is therefore interesting to investigate the influence of flexibility of these particles on the liquid crystalline phases.

A very useful model for such a particle or semiflexible polymer is the so-called worm-like chain, proposed by Kratky and Porod in 1949 [47]. This model has been tested extensively in case of dilute polymer solutions and has been shown to account well for the equilibrium and dynamical properties of long, slightly flexible polymers [48, 49]. During the past decade, the worm-like chain has been used as a model for liquid crystals, gels, and semiflexible polymers in confined geometries [42, 43, 50–52]. An important feature of the model is that the flexibility is homogeneously distributed along the chain contour. The characteristic length scale on which the direction of the tangent vector $\hat{u}$ along the chain alters is the persistence length l_P:

$$\langle \hat{u}(s) \cdot \hat{u}(s + \Delta s) \rangle = \exp(-|\Delta s|/l_P) \tag{2.13}$$

where s is the distance along the contour of the chain (see Fig. 2.3) and the brackets denote an average over polymer conformations. The persistence length is also directly related to the elastic bending constant C:

$$l_P = \frac{C}{k_B T} \tag{2.14}$$

The bending energy of the chain F_b can now be given in terms of the total curvature along the polymer:

$$F_b = \frac{1}{2} \int C \left| \frac{\partial \hat{u}(s')}{\partial s'} \right|^2 ds' \tag{2.15}$$

If some gradual flexibility is admitted in the rigid rod model, the orientational entropy will alter. In the nematic phase, all segments of all polymers are more or less aligned along the nematic director. This alignment corresponds with a considerable loss in orientational entropy, which becomes now a function of the number of persistent lengths per chain, i.e., L/l_P, where L is the contour length of the polymer. Using a method, that was earlier proposed by Lifshitz [53, 54], Khokhlov and Semenov [42] derived an expression for this orientational entropy per chain:

$$S_{\text{worm}} = \frac{k_B L}{2 l_P} \int f^{1/2}(\Omega) \Delta f^{1/2}(\Omega) d\Omega \tag{2.16}$$

where $f(\Omega)$ is the angular distribution function of the segments of the chains and Δ is equal to the Laplacian restricted to a unit sphere:

$$\Delta = \frac{1}{\sin \theta} \frac{\partial}{\partial \theta} \left(\sin \theta \frac{\partial}{\partial \theta} \right) \tag{2.17}$$

$\widehat{\boldsymbol{u}}(s+\Delta s)$
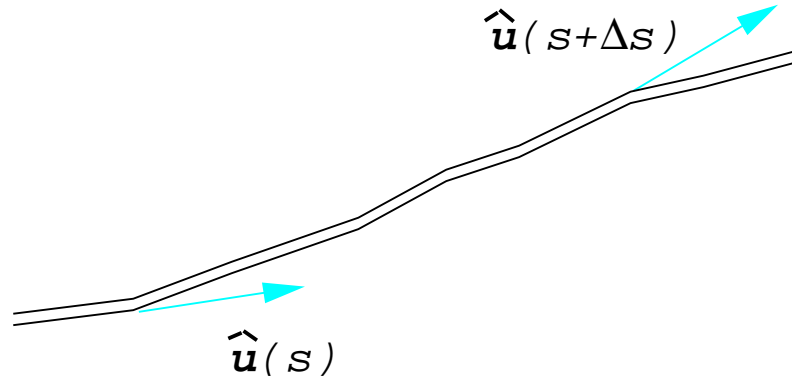
$\widehat{\boldsymbol{u}}(s)$

FIGURE 2.3   Schematic representation of a small part of a worm-like chain.

This expression for the orientational entropy is appropriate for long persistent polymers, i.e., $L \gg l_P \gg D$, where D is the diameter of the chain. In this so-called semiflexible limit the chains are locally very stiff, but are so long that they form coils in dilute solutions. In the Appendix of this chapter, we sketch this derivation of the orientational entropy in more detail. For an isotropic distribution, i.e., $f(\Omega) = 1/4\pi$, this orientational entropy is zero. However, in the nematic phase, S_{worm} is always less than zero, which can be seen by partial integration of Eq. 2.16.

Let us now consider how the interaction term changes when we admit some degree of flexibility in the hard rod model. For a fluid of N hard rods of length L, diameter D, and density ρ, the interaction term reads for $L \gg D$ (see Eqs. 2.9 and 2.11)

$$NB_2\rho = \frac{N^2L^2D}{V} \iint f(\Omega)f(\Omega')\,|\sin\gamma|\,d\Omega d\Omega' \tag{2.18}$$

If we now divide each rod in M segments of length L/M, the number of rods becomes NM. The interaction term $NB_2\rho$ for a fluid of NM rods of length L/M remains now the same as the one for the original system. Worm-like chains can be considered as being built up from independent local rigid segments ($l_P \gg L/M \gg D$) that interact locally as thin rods. Therefore Eq. 2.18 can also be used in the case of worm-like chains. The Helmholtz free energy for worm-like chains reads now

$$\begin{aligned}\frac{\Delta F}{Nk_BT} &= \log(\Lambda^3\rho) - 1 - \frac{L}{2l_P}\int f^{1/2}(\Omega)\Delta f^{1/2}(\Omega)d\Omega \\ &\quad + \rho L^2D \int f(\Omega)f(\Omega')\,|\sin\gamma|\,d\Omega d\Omega'\end{aligned} \tag{2.19}$$

In summary, the inclusion of flexibility in the rigid rod model leads only to a change in orientational entropy. We have derived the expressions for the contributions to the free energy due to the orientational entropy $\sigma(f)$ for two extreme cases, namely the rod limit ($l_P \gg L \gg D$) in Sec. 2.2

$$\sigma_{\mathrm{rod}}(f) = \int f(\Omega) \log(4\pi f(\Omega)) d\Omega \qquad (2.20)$$

and above, the semiflexible limit ($L \gg l_P \gg D$)

$$\sigma_{\mathrm{worm}}(f) = -\frac{L}{2l_P} \int f^{1/2}(\Omega) \Delta f^{1/2}(\Omega) d\Omega \qquad (2.21)$$

However, in experimental situations we often find the intermediate case, where $L \simeq l_P \gg D$. The problem now is to find an expression for the entropy in this case. Khokhlov and Semenov derived an expression for the entropy for arbitrary L/l_P. Unfortunately, this expression is too complicated for specific calculations [43]. Using the Onsager trial function with α as variational parameter for the orientational distribution function, they were able to calculate the correction terms to the rod and the semiflexible limit.

$$f(\cos\theta) = \frac{\alpha \cosh(\alpha \cos\theta)}{4\pi \sinh\alpha} \qquad (2.22)$$

Using these correction terms for the entropy, they calculated the change in phase behaviour. Interpolation of these results to intermediate cases (and later corrected by Odijk [51]) yields now a formula for the phase transition concentrations for arbitrary L/l_P [43, 41]. Another approach was made by Odijk. Instead of the Onsager trial function, he used a Gaussian distribution function for the orientational distribution function.

$$f(\theta) = \begin{cases} (\alpha/4\pi) \exp\left[\alpha\theta^2/2\right] & (0 \le \theta \le \pi/2) \\ (\alpha/4\pi) \exp\left[\alpha(\pi-\theta)^2/2\right] & (\pi/2 \le \theta \le \pi) \end{cases} \qquad (2.23)$$

It is now possible to derive an expression for the configurational entropy for arbitrary lengths of the polymer within this Gaussian approximation [51]. Phase diagrams calculated with the help of this exact expression deviate significantly from the ones based on the interpolation formula of Khokhlov and Semenov. In addition, Hentschke found an interpolation formula between the rod and the semiflexible limit that resembles numerically the expression of Odijk [55]. In chapter 5, we discuss in more detail the different theories of semiflexible polymers for arbitrary L/l_P and we compare them with simulation results.

Appendix

In 1981, Khokhlov and Semenov derived an expression for the orientational entropy appropiate for long persistent chains ($L \gg l_P \gg D$) [42, 43]. Their expression is often used as a basis for theories of semiflexible polymers. Unfortunately, the reader interested in a complete derivation of this important result is forced to gather material scattered over many papers. In this Appendix, we give a complete derivation of the Khokhlov and Semenov expression. The partition function for a worm-like chain with fixed tangent vectors $\hat{u}_0$ for the initial direction and $\hat{u}_L$ for the final direction in an external field $U(\hat{u}(s))$ can be obtained by integration over all possible conformations of the chain, which we denote by $\int D\hat{u}(s)$ [56]:

$$Z(\hat{u}_0, \hat{u}_L; 0, L) = \int D\hat{u}(s)\exp(-\beta S[\hat{u}(s)]) \tag{2.24}$$

where $S[\hat{u}(s)]$ is given by

$$S[\hat{u}(s)] = \int_0^L \frac{1}{2}C \left| \frac{\partial \hat{u}(s')}{\partial s'} \right|^2 + U(\hat{u}(s'))\, ds' \tag{2.25}$$

In Eq. 2.24, we have written $Z(\hat{u}_0, \hat{u}_L; 0, L)$ in the path integral representation, where the factor $\exp(-\beta S[\hat{u}(s)])$ assigns a weight to every path or trajectory described by the function $\hat{u}(s)$. If we now decompose the chain in M small segments of length a, such that $Ma = L$, we can rewrite $S[\hat{u}(s)]$ as follows

$$S[\hat{u}(s)] \simeq \sum_{i=0}^{M-1} \int_{s_i}^{s_{i+1}} \frac{1}{2}C \left[\frac{\hat{u}(s_{i+1}) - \hat{u}(s_i)}{s_{i+1} - s_i} \right]^2 + U(\hat{u}(s_{i+1}))\, ds' \tag{2.26}$$

This expression becomes exact in the worm-like chain limit: $a \to 0, M \to \infty$ such that $Ma = L$ remains fixed and finite, under the condition that the ratio $a/\langle 1 - \cos\theta \rangle \simeq 2a/\langle\theta^2\rangle \equiv l_P$. Here θ denotes the angle between two subsequent segments. As the integrand in Eq. 2.26 is independent of s' and $s_{i+1} - s_i = a$, $S[\hat{u}(s)]$ reads

$$S[\hat{u}(s)] = \sum_{i=0}^{M-1} \frac{C}{2a}(\hat{u}(s_{i+1}) - \hat{u}(s_i))^2 + aU(\hat{u}(s_{i+1})) \tag{2.27}$$

If we now use the so-called Wiener measure:

$$\int D\hat{u}(s) = \lim_{\substack{a \to 0 \\ M \to \infty \\ Ma = L}} \int \frac{1}{B} \prod_{i=0}^{M-1} \frac{d\hat{u}(s_{i+1})}{B} \tag{2.28}$$

with B a normalisation constant, which will be defined below, we can rewrite the partition function as follows

$$Z(\hat{u}_0, \hat{u}_L; 0, L) = \frac{1}{B} \int \prod_{i=0}^{M-1} d\hat{u}(s_{i+1}) G(\hat{u}(s_i), \hat{u}(s_{i+1})); s_i, s_{i+1}) \quad (2.29)$$

where we introduced the so-called propagator $G(\hat{u}(s_i), \hat{u}(s_{i+1})); s_i, s_{i+1})$

$$G(\hat{u}(s_i), \hat{u}(s_{i+1})); s_i, s_{i+1}) = $$
$$\frac{1}{B} \exp\left[-\beta\left(\frac{C}{2a}(\hat{u}(s_{i+1}) - \hat{u}(s_i))^2 + aU(\hat{u}(s_{i+1}))\right)\right] \quad (2.30)$$

The normalisation constant B is defined such that $G_0(\hat{u}(s_i), \hat{u}(s_{i+1})); a)$, the propagator for a free chain, for which $U(\hat{u}(s_{i+1})) = 0$, is normalised to unity:

$$\int d\hat{u}(s_{i+1}) G_0(\hat{u}(s_i), \hat{u}(s_{i+1}); a) = 1 \quad (2.31)$$

Note that the evolution of the chain is now written in terms of a series of propagators $G(\hat{u}(s_i), \hat{u}(s_{i+1}); s_i, s_{i+1})$, which can be interpreted as the conditional probability that segment i with orientation $\hat{u}(s_i)$ is followed by an orientation $\hat{u}(s_{i+1})$ for the $(i + 1)$th segment. However, if we want to know the probability that the $(i + 1)$th segment has an orientation $\hat{u}(s_{i+1})$ irrespective of the orientations of the previous segments, we have to introduce a new function $\psi(\hat{u}(s_{i+1}), s_{i+1})$. The total probability that the $(i + 1)$th segment has an orientation $\hat{u}(s_{i+1})$ is equal to the integral over all possible values of $\hat{u}(s_i)$ of the probability to have an orientation $\hat{u}(s_i)$ for the ith segment multiplied by the probability to go from an orientation $\hat{u}(s_i)$ at the ith segment to $\hat{u}(s_{i+1})$ for the $(i + 1)$th segment:

$$\psi(\hat{u}(s_{i+1}), s_{i+1}) = \int \psi(\hat{u}(s_i), s_i) G(\hat{u}(s_i), \hat{u}(s_{i+1}); s_i, s_{i+1}) d\hat{u}(s_i) \quad (2.32)$$

Since $G(\hat{u}(s_i), \hat{u}(s_{i+1}); s_i, s_{i+1})$ is known, knowledge of $\psi(\hat{u}(s_i), s_i)$ for a particular segment i, enables us to compute how this probability distribution function $\psi(\hat{u}(s), s)$ evolves, if we propagate the chain. Sometimes, it is more convenient to reduce the path integral into a differential equation. We therefore calculate what the probability is to find a certain orientation if we proceed the chain by a very short segment of length a. Inserting Eq. 2.30 into Eq. 2.32 yields

$$\psi(\hat{u}(s_i + a), s_i + a) = $$
$$\int \frac{1}{B} \exp\left[-\beta\left(\frac{C}{2a}[\hat{u}(s_i + a) - \hat{u}(s_i)]^2 + aU(\hat{u}(s_i + a))\right)\right]$$
$$\times \psi(\hat{u}(s_i), s_i)\ d\hat{u}(s_i) \quad (2.33)$$

Only if $\hat{u}(s_i + a)$ is close to $\hat{u}(s_i)$ we get important contributions to this integral. For this reason we make the substitution $\hat{u}(s_i) = \hat{u}(s_i + a) + \delta\hat{u}$. We obtain

$$
\begin{aligned}
\psi(\hat{u}(s_i + a), s_i + a) &= \int \frac{1}{B} \exp\left[-\beta\left(\frac{C}{2a}\delta\hat{u}^2 + aU(\hat{u}(s_i + a))\right)\right] \\
&\quad \times \psi(\hat{u}(s_i + a) + \delta\hat{u}, s_i)\ d\delta\hat{u}
\end{aligned}
\tag{2.34}
$$

We now expand $\psi(\hat{u}(s_i + a), s_i + a)$ in a power series about $(\hat{u}(s_i + a), s_i)$. We need only keep terms of order a. This implies keeping second-order terms in $\delta\hat{u}$, as we want to keep $\delta\hat{u}^2/a$ small.

Expanding the left-hand side of Eq. 2.34 to first order in a and the right-hand side to first order in a and second order in $\delta\hat{u}$, we obtain

$$
\begin{aligned}
\psi(\hat{u}(s_i + a), s_i) + a\frac{\partial\psi}{\partial s_i} &= \int \frac{1}{B} \exp[-\beta\frac{C}{2a}\delta\hat{u}^2]\,[1 - a\beta U(\hat{u}(s_i + a))] \\
&\quad \times \left[\psi(\hat{u}(s_i + a, s_i)) + \delta\hat{u}\frac{\partial\psi}{\partial\hat{u}(s_i + a)} + \frac{1}{2}\delta\hat{u}^2\frac{\partial^2\psi}{\partial\hat{u}(s_i + a)^2}\right]\ d\delta\hat{u}
\end{aligned}
\tag{2.35}
$$

As the propagator is normalised to unity (see Eq. 2.31), we find that

$$
\int \frac{1}{B} \exp[-\beta\frac{C}{2a}\delta\hat{u}^2]\ d\delta\hat{u} = 1
\tag{2.36}
$$

Because of the freely rotating character of the chain, we obtain

$$
\int \frac{1}{B} \exp[-\beta\frac{C}{2a}\delta\hat{u}^2]\delta\hat{u}\ d\delta\hat{u} = \langle\delta\hat{u}\rangle_0 = \langle\hat{u}(s_i) - \hat{u}(s_i + a)\rangle_0 = 0
\tag{2.37}
$$

Using the following properties of a worm-like chain

$$
\begin{aligned}
\langle\delta\hat{u}_x^2\rangle_0 = \langle\delta\hat{u}_y^2\rangle_0 &= \frac{1}{2}\langle\delta\hat{u}^2\rangle_0 \simeq \frac{1}{2}\langle\theta^2\rangle \simeq a/l_P \\
\langle\delta\hat{u}_x\delta\hat{u}_y\rangle_0 &= \langle\delta\hat{u}_x\rangle_0\langle\delta\hat{u}_y\rangle_0 = 0
\end{aligned}
\tag{2.38}
$$

yields

$$
\int \frac{1}{B} \exp[-\beta\frac{C}{2a}\delta\hat{u}^2]\delta\hat{u}^2 d\delta\hat{u} = \langle\delta\hat{u}^2\rangle_0 = \frac{a}{l_P}
\tag{2.39}
$$

Inserting Eq. 2.36-2.39 in Eq. 2.35, we find that $\psi(\hat{u}(s_{i+1}), s_i)$ satisfies the following diffusion equation:

$$
\frac{\partial\psi(\hat{u}(s_{i+1}), s_i)}{\partial s_i} = \left[\frac{\Delta_{\hat{u}(s_{i+1})}}{2l_P} - \beta U(\hat{u}(s_{i+1}))\right]\psi(\hat{u}(s_{i+1}), s_i)
\tag{2.40}
$$

Note the analogy of Eq. 2.40 with the Schrödinger equation for a particle in a potential field [57]. If we now use the propagator $G(\hat{u}(s_i), \hat{u}(s_i + a); s_i, s_i + a)$ instead of the normal probability distribution function $\psi(\hat{u}(s_i + a), s_i + a)$ in Eq. 2.33, we find easily that also this propagator or conditional probability distribution function satisfies this differential equation. Moreover, we can derive similarly that also the partition function Eq. 2.29 is a solution of this diffusion equation:

$$\frac{\partial Z(\hat{u}_0, \hat{u}_L; 0, L)}{\partial L} = \left[\frac{\Delta_{\hat{u}_L}}{2l_P} - \frac{U(\hat{u}_L)}{k_B T} \right] Z(\hat{u}_0, \hat{u}_L; 0, L) \tag{2.41}$$

with the natural boundary condition:

$$\lim_{L \to 0} Z(\hat{u}_0, \hat{u}_L; 0, L) = \delta(\hat{u}_0 - \hat{u}_L) \tag{2.42}$$

As the segment length is fixed and only the direction of the tangent vector changes, it is convenient to rewrite the propagator in standard spherical coordinates θ and ϕ, which denote the polar and azimuthal angle of the $(i + 1)$th segment with respect to $\hat{u}_i$. Eq. 2.41 describes now the diffusion on a unit sphere and the Laplacian $\Delta_{\hat{u}_L}$ is therefore restricted to this sphere.

$$\Delta_{\hat{u}_L} = \frac{1}{\sin \theta} \frac{\partial}{\partial \theta} \left(\sin \theta \frac{\partial}{\partial \theta} \right) + \left\{ \frac{1}{\sin^2 \theta} \frac{\partial^2}{\partial \phi^2} \right\} \tag{2.43}$$

In the case of a uniaxial nematic the azimuthal variation (within brackets) is irrelevant.

In order to solve Eq. 2.41, we use an expansion in orthonormal eigenfunctions $\phi_n(\hat{u}_L)$ of

$$\left[\frac{\Delta_{\hat{u}_L}}{2l_P} - \frac{U(\hat{u}_L)}{k_B T} \right] \phi_n(\hat{u}_L) = \lambda_n \phi_n(\hat{u}_L) \tag{2.44}$$

with eigenvalues λ_n. Then we find

$$Z(\hat{u}_0, \hat{u}_L; 0, L) = \sum_n a_n e^{\lambda_n L} \phi_n(\hat{u}_0) \phi_n(\hat{u}_L) \tag{2.45}$$

Here we have used the fact that the partition function is symmetric in $\hat{u}_0$ and $\hat{u}_L$, i.e., $Z(\hat{u}_0, \hat{u}_L; 0, L) = Z(\hat{u}_L, \hat{u}_0; 0, L)$. The boundary condition (Eq. 2.42) reads now

$$\lim_{L \to 0} \sum_n a_n e^{\lambda_n L} \phi_n(\hat{u}_0) \phi_n(\hat{u}_L) = \delta(\hat{u}_0 - \hat{u}_L) \tag{2.46}$$

From this boundary condition, we derive that

$$\phi_m(\hat{u}_L) = \int \phi_m(\hat{u}_0) \, \delta(\hat{u}_0 - \hat{u}_L) \, d\hat{u}_0 = a_m \phi_m(\hat{u}_L) \tag{2.47}$$

and hence, we find that $a_m = 1$ for all m.

Here we have used the fact that the eigenfunctions are orthonormal:

$$\int \phi_n(\hat{\mathbf{u}}_L)\phi_m(\hat{\mathbf{u}}_L)\, d\hat{\mathbf{u}}_L = \delta_{nm} \tag{2.48}$$

In the limit $L \to \infty$ or $L \gg l_P$ only the largest eigenvalue, say λ_0, is relevant.

$$Z(\hat{\mathbf{u}}_0, \hat{\mathbf{u}}_L; 0, L) \sim e^{\lambda_0 L}\phi_0(\hat{\mathbf{u}}_0)\phi_0(\hat{\mathbf{u}}_L) \tag{2.49}$$

The partition function $Z(\hat{\mathbf{u}}_0, \hat{\mathbf{u}}_L; 0, L)$ may be interpreted as the (unnormalised) conditional probability that a chain starting with direction $\hat{\mathbf{u}}_0$ will have direction $\hat{\mathbf{u}}_L$ after a contour length L. Because of the Markov character of the chain, the orientational distribution function at a point s of the chain with fixed end vectors $\hat{\mathbf{u}}_0$ and $\hat{\mathbf{u}}_L$ can be given by the probability that the two separate endparts of the chain have the same endvector $\hat{\mathbf{u}}_s$:

$$f(\hat{\mathbf{u}}_s, s) = \frac{1}{B'}\iint Z(\hat{\mathbf{u}}_0, \hat{\mathbf{u}}_s; 0, s)Z(\hat{\mathbf{u}}_s, \hat{\mathbf{u}}_L; 0, L-s)\, d\hat{\mathbf{u}}_0\, d\hat{\mathbf{u}}_L \tag{2.50}$$

with B' a normalisation constant

$$B' = \iint Z(\hat{\mathbf{u}}_0, \hat{\mathbf{u}}_L; 0, L)\, d\hat{\mathbf{u}}_0\, d\hat{\mathbf{u}}_L \tag{2.51}$$

When $L \gg l_P$ most of the points s are far from the chain ends and it is possible to define an average distribution function

$$f(\hat{\mathbf{u}}_s) = \frac{1}{L}\int_0^L f(\hat{\mathbf{u}}_s, s)\, ds \tag{2.52}$$

Inserting Eqs. 2.49 and 2.50 in Eq. 2.52 yields

$$f(\hat{\mathbf{u}}_s) = \phi_0^2(\hat{\mathbf{u}}_s) \tag{2.53}$$

where the distribution function $f(\hat{\mathbf{u}}_s)$ is normalised:

$$\int f(\hat{\mathbf{u}}_s)\, d\hat{\mathbf{u}}_s = 1 \tag{2.54}$$

Finally, the free energy of the chain is simply

$$\begin{aligned}
F &= -k_B T \log \iint Z(\hat{\mathbf{u}}_0, \hat{\mathbf{u}}_L; 0, L)\, d\hat{\mathbf{u}}_0\, d\hat{\mathbf{u}}_L \\
&\simeq -\lambda_0 k_B T L
\end{aligned} \tag{2.55}$$

which is an extensive quantity, i.e., proportional to the length of the polymer. The energy E of the chain is

$$E = L \int U(\hat{u}_s) f(\hat{u}_s) \, d\hat{u}_s \tag{2.56}$$

and the entropy can then be obtained as follows

$$
\begin{aligned}
S & = \frac{E - F}{T} \simeq k_B L \int \left(\lambda_0 + \frac{U(\hat{u}_s)}{k_B T} \right) \phi_0^2(\hat{u}_s) \, d\hat{u}_s \\
& \stackrel{2.44}{\simeq} k_B \frac{L}{2l_P} \int \phi_0(\hat{u}_s) \Delta_{\hat{u}_s} \phi_0(\hat{u}_s) \, d\hat{u}_s \\
& \simeq k_B \frac{L}{2l_P} \int f^{1/2}(\hat{u}_s) \Delta_{\hat{u}_s} f^{1/2}(\hat{u}_s) \, d\hat{u}_s
\end{aligned}
\tag{2.57}
$$

It is important to note that in this theory, first a fictitious external field is introduced, which is eliminated in the end in the expression for the entropy. Some arguments can be given that this external field indeed exists for a solution of polymers in the nematic phase. In the nematic phase each polymer feels a potential due to the presence of the aligned neighbours. Warner used in his calculations a Maier-Saupe mean-field potential and solved the equations self-consistently [58].

3   Confinement Free Energy of Semiflexible Polymers

In this chapter, we investigate the behaviour of a single polymer in a cylinder by means of computer simulations. We compute the confinement free energy of a worm-like chain in a tube and compare the results with the theoretical predictions of the scaling theory of Odijk, the fluctuation theory of Helfrich and the theory of Khokhlov and Semenov.

3.1   Introduction

In chapter 2, we reviewed the liquid crystal forming properties of fluids of hard stiff elongated particles [41] (and references therein). In nature, however, most rodlike particles are not completely stiff, but show a certain degree of flexibility. It is therefore interesting to investigate the influence of flexibility on the formation of liquid crystalline phases by such particles. In particular, we are interested in the phase behaviour of long flexible molecules, i.e., the constituent particles of main-chain liquid crystalline polymers. At high density, each chain is strongly hindered by neighbouring polymers in the system and we can assume that each polymer is effectively confined to a tube with diameter D as shown in Fig. 3.1. It is, hence, a good starting point to study first one single polymer in a tube.

A key quantity in the theoretical description of confined worm-like chains is the change in free energy associated with this confinement. This free energy plays an important role in the phase behaviour of semiflexible molecules. In Ref. [51], some of the theories that can be used to estimate the confinement free energy of a worm-like chain are reviewed [42, 43, 50, 52, 59, 60]. In section 3.2, we will discuss the several theoretical appoaches. First, we will discuss the scaling theory of Odijk [50, 51].
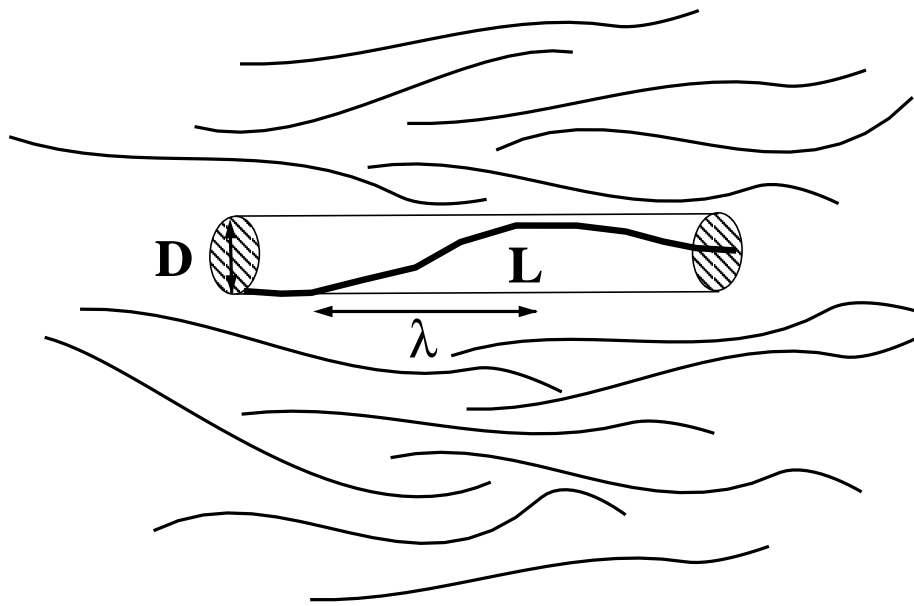
FIGURE 3.1   At high density, each polymer is more or less confined to a tube.

Then, we will explain Helfrich's theory, which is based on a rather ad-hoc assumption. Originally, his theory was derived for membranes. In his derivation, Helfrich assumed that the tube that confines the polymer exerts a restoring force on the polymer that works equally on all Fourier modes of the polymer conformations. In the end, we will extend the theory of Khokhlov and Semenov, described in section 2.3, for a semiflexible polymer in a tube. Although, at first sight, the basic concepts of the theories seem rather different, they all lead to similar predictions for the confinement free energy. Nevertheless, neither the basic concepts in the theories of worm-like chains have ever been directly tested, nor have their predictions been verified. It is therefore interesting to test some of these assumptions in the theoretical description of worm-like chains by computer simulations. However, numerical simulations of worm-like chains are difficult with the existing Monte Carlo schemes.

   In this chapter we describe a novel computational approach to this problem based on the configurational-bias Monte Carlo method [61]. The aim of the simulations is twofold. First, we test the scaling relations of the confinement free energy and we compute the prefactor. In the second place, we want to test Helfrich's assumption concerning the suppression of the Fourier modes of the polymer conformations and we want to investigate the scaling behaviour of these Fourier spectra. In section 3.3, our choice of simulation technique is explained and the results of our simulations are

discussed in section 3.4. The reader, who is interested in the technical details of this computational scheme, is referred to the Appendix of this chapter.

3.2 Theories of Semiflexible Polymers in a Tube

In what follows, we use the notation of Odijk [50, 51]. We consider an infinitely thin polymer with contour length L and persistence length l_P and $L \gg l_P$. In the nematic state, we can approximate the bending free energy (Eq. 2.15) of a polymer by considering only small displacements of the chain in the x- and y-direction with respect to the axis of the tube, which is oriented along the z-direction.

$$F_b = \frac{1}{2} C \int_0^L \left(\frac{d^2 r_x}{ds^2} \right)^2 + \left(\frac{d^2 r_y}{ds^2} \right)^2 \, ds \tag{3.1}$$

where r_x and r_y denote the displacements of the chain in the x- and y-direction, respectively. To compute the confinement free energy of a stiff chain in a long cylindrical pore of diameter D, Odijk [50, 51] has introduced a very useful concept, namely the deflection length λ. This length scale, corresponds to the average distance between successive deflection points of the chain in the pore (see Fig. 3.1). In Ref. [51] it is shown that the theories of Refs. [42, 43, 50, 52] all yield qualitatively the same expression for the confinement free energy ΔF_c:

$$\frac{\Delta F_c}{k_B T} \sim \frac{L}{\lambda} \tag{3.2}$$

Odijk made Eq. 3.2 plausible by a scaling argument [50, 51]. An extensive quantity like the free energy must scale like $k_B T$ times the chain length divided by the only other relevant length scale. As the chain loses its angular correlations through these deflections, this relevant length scale is no longer the persistence length l_P, but the deflection length λ and we arrive at Eq. 3.2. For the deflection length of a stiff chain in a long cylindrical pore of diameter D, the following expression can be derived [62, 50]

$$\lambda \sim l_P^{1/3} D^{2/3} \tag{3.3}$$

Inserting Eq. 3.3 in Eq. 3.2 yields:

$$\frac{\Delta F_c}{k_B T} = c \, \frac{L}{l_P^{1/3} D^{2/3}} \tag{3.4}$$

for $l_P \gg \lambda$ and where c is a dimensionless prefactor.

Helfrich's line of reasoning is quite different and is based on the so-called undulation force [52] due to the confinement of the polymer. If we introduce a Fourier expansion of the displacements of the polymer:

$$r_j(s) = \sum_{q=-\infty}^{\infty} a_{j,q} e^{iqs}, \qquad j = x, y \tag{3.5}$$

the mean-square amplitudes $\langle a_q^2 \rangle_{\text{free}}$ for one direction for a free polymer can be deduced from Eq. 3.1 and the equipartition theorem.

$$\frac{1}{2} C L q^4 \langle a_q^2 \rangle_{\text{free}} = \frac{1}{2} k_B T \tag{3.6}$$

If we now put the polymer in a tube the fluctuations of the polymer will be partly suppressed. Helfrich [52] assumes that all Fourier modes will be suppressed by the same amount:

$$\frac{1}{\langle a_q^2 \rangle_{\text{restr}}} = \frac{1}{\langle a_q^2 \rangle_{\text{free}}} + \tau \tag{3.7}$$

where the subscript restr refers to the restricted polymer. The mean-square displacement of the confined polymer for one direction can be calculated from:

$$\langle r^2 \rangle = \sum_{q=-\infty}^{\infty} \langle a_q^2 \rangle_{\text{restr}} \tag{3.8}$$

Replacing the sum by an integral:

$$\sum_{q=-\infty}^{\infty} \rightarrow \frac{L}{2\pi} \int_{-\infty}^{\infty} dq \tag{3.9}$$

and using Eq. 3.6-3.8 yields:

$$\begin{aligned} \langle r^2 \rangle &= \frac{1}{2\pi} \left(\frac{L}{\tau} \right)^{3/4} \left(\frac{1}{l_P} \right)^{1/4} \int_{-\infty}^{\infty} \frac{1}{1+q^4} \, dq \\ &= \left(\frac{L}{4\tau} \right)^{3/4} \left(\frac{1}{l_P} \right)^{1/4} \end{aligned} \tag{3.10}$$

On the other hand the mean square displacement must be of the order of the square of the diameter of the tube.

$$\langle r^2 \rangle = \mu D^2 \tag{3.11}$$

where μ is a still undefined number near unity. Eliminating $\langle r^2 \rangle$ between Eqs. 3.10 and 3.11 leads to:

$$\frac{\tau}{L} = \frac{1}{4\mu^{4/3} D^{8/3} l_P^{1/3}} \tag{3.12}$$

The confinement free energy can now be calculated with the help of a plausible expression for the associated change in free energy of a single mode ΔF_q [59] and by integration over all q modes and the two independent directions

$$\frac{\Delta F_c}{k_B T} = -\frac{L}{2\pi} \int_{-\infty}^{\infty} \log \frac{\langle a_q^2 \rangle_{\mathrm{restr}}}{\langle a_q^2 \rangle_{\mathrm{free}}} \, dq \tag{3.13}$$

Using Eq. 3.6 and 3.7 results in

$$\frac{\Delta F_c}{k_B T} = \frac{L}{2\pi} \left(\frac{\tau}{l_P L} \right)^{1/4} \int_{-\infty}^{\infty} \log \left(1 + \frac{1}{q^4} \right) \, dq = \frac{L}{\mu^{1/3} l_P^{1/3} D^{2/3}} \tag{3.14}$$

This leads again to Eq. 3.4. It is interesting to note that, unlike the scaling approach, Helfrich's theory leads to a prediction for the prefactor c, namely $c = \mu^{-1/3}$. Eq. 3.13 shows that the ratio of the mean square amplitudes for the confined chain and the free polymer is directly correlated to the confinement free energy and it is therefore interesting to investigate this quantity in more detail. Using Eq. 3.6 and 3.7, we can rewrite this quantity as follows

$$R(q) = \frac{\langle a_q^2 \rangle_{\mathrm{restr}}}{\langle a_q^2 \rangle_{\mathrm{free}}} = \frac{q^4}{q^4 + \tilde{q}^4} \tag{3.15}$$

with

$$\tilde{q} = \left(\frac{\tau}{l_P L} \right)^{1/4} = \frac{1}{2^{1/2} \mu^{1/3} D^{2/3} l_P^{1/3}} \simeq \frac{1}{2^{1/2} \mu^{1/3} \lambda} \tag{3.16}$$

and we see that $\tilde{q}$ scales with the reciprocal of the deflection length λ with a prefactor:

$$c_1 = 2^{-1/2} \mu^{-1/3} \tag{3.17}$$

In chapter 2, we derived, following the theory of Khokhlov and Semenov, an expression for the contribution to the free energy due to the orientational entropy (Eq. 2.21). The confinement free energy is equal to this free energy term. If we now confine a semiflexible polymer in a cylinder, we can imagine that this tube forces the polymer in such a way

that it remains within a certain angular range. Particularly, we can assume that the orientational distribution function of the segments of the polymer is of the Gaussian type (see Eq. 2.23). From this assumption for the orientational distribution function follows

$$\langle \theta^2 \rangle = 2\alpha^{-1} \tag{3.18}$$

On the other hand, if we use Eq. 2.13, we obtain

$$
\begin{aligned}
\langle \hat{u}(s) \cdot \hat{u}(s + \Delta s) \rangle &= \langle \cos \theta(\Delta s) \rangle = 1 - \frac{1}{2} \langle \theta^2 (\Delta s) \rangle + \cdots \\
&= 1 - \frac{|\Delta s|}{l_P} + \cdots
\end{aligned}
\tag{3.19}
$$

Hence, we can derive that for small Δs:

$$\langle \theta^2 (\Delta s) \rangle \simeq \frac{2|\Delta s|}{l_P} \tag{3.20}$$

If $|\Delta s|$ becomes so large that $\langle \theta^2 (\Delta s) \rangle$ exceeds $\langle \theta^2 \rangle$ the chain will be deflected by the tube, such that it remains within the angular range. This fixes the deflection length. Comparing Eq. 3.18 and 3.20 yields for this deflection length:

$$\lambda \sim \frac{l_P}{\alpha} \tag{3.21}$$

Eq. 3.3 can now easily be derived, if we realise that $\langle \theta^2 \rangle$ is of the order of $(D/\lambda)^2$ (see Fig. 3.1):

$$\langle \theta^2 \rangle \sim \frac{D^2}{\lambda^2} \sim \frac{2\lambda}{l_P} \tag{3.22}$$

If we now integrate Eq. 2.21 by parts, we find

$$\frac{\Delta F_c}{k_B T} = \frac{L}{8l_P} \int d\Omega \left(\frac{\partial f(\theta)}{\partial \theta} \right)^2 f(\theta)^{-1} \tag{3.23}$$

where $d\Omega$ is equal to $\sin \theta \, d\theta \, d\phi$. Using the Gaussian approximation (Eq. 2.23) gives us again

$$\frac{\Delta F_c}{k_B T} = \frac{L}{8l_P} \alpha^2 \langle \theta^2 \rangle = \frac{L}{4 l_P^{1/3} D^{2/3}} \tag{3.24}$$

3.3 Monte Carlo Simulations

Our aim is to compute the increase of free energy of a semiflexible chain, due to the confinement imposed by the tube. The confinement free energy can be expressed in terms of the partition function of the confined chain and of the ideal chain, Z and Z^{id}, respectively:

$$\Delta F_c = -k_B T \log \left(\frac{Z}{Z^{\text{id}}} \right) \tag{3.25}$$

The ideal chain, i.e., a chain that is not confined in a cylinder, is our reference state. The ideal chain will have an internal potential energy that is equal to the sum of the bending energies of the individual joints. The bending energy for a joint between segments $i-1$ and i of a polymer with conformation $\Gamma_{\mathbf{w}}$ is

$$u^{\text{id}}_{\hat{\mathbf{w}}_{i-1}\hat{\mathbf{w}}_i} = C' \, \theta^2_{\hat{\mathbf{w}}_{i-1}\hat{\mathbf{w}}_i} \tag{3.26}$$

where $\theta_{\hat{\mathbf{w}}_{i-1}\hat{\mathbf{w}}_i}$ is the angle between the unit vectors $\hat{\mathbf{w}}_{i-1}$ and $\hat{\mathbf{w}}_i$ that specify, respectively, the orientations of the segments $i-1$ and i. If we compare Eq. 3.26 with the expression for the bending energy per unit length of a continuous, semiflexible polymer (Eq. 3.1), we get

$$C' = \frac{C}{2\ell} \tag{3.27}$$

where ℓ is the segment length. In what follows, we shall choose ℓ to be our unit of length.

Monte Carlo simulations can be used to measure ensemble averages like $\langle A \rangle$, but cannot be used to compute the partition function directly. Thus, it is impossible to compute the confinement free energy by computing the partition function of the confined chain and of the ideal chain seperately. Special techniques are required to compute free energies. Fortunately, the ratio of the two partition functions in Eq. 3.25 can be rewritten as an ensemble average, similar to the so-called 'particle-insertion method' of Widom [63]. The expression for the confinement free energy then becomes

$$
\begin{aligned}
\Delta F_c &= -k_B T \log \left(\frac{\int \prod_{i=1}^{L} d\hat{\mathbf{w}}_i \exp[-\beta \sum_{i=1}^{L} (u^{\text{id}}_{\hat{\mathbf{w}}_{i-1}\hat{\mathbf{w}}_i} + u^{\text{wall}}_{\hat{\mathbf{w}}_i})]}{\int \prod_{i=1}^{L} d\hat{\mathbf{w}}_i \exp[-\beta \sum_{i=1}^{L} u^{\text{id}}_{\hat{\mathbf{w}}_{i-1}\hat{\mathbf{w}}_i}]} \right) \\
&= -k_B T \log \left\langle \exp[-\beta \sum_{i=1}^{L} u^{\text{wall}}_{\hat{\mathbf{w}}_i}] \right\rangle
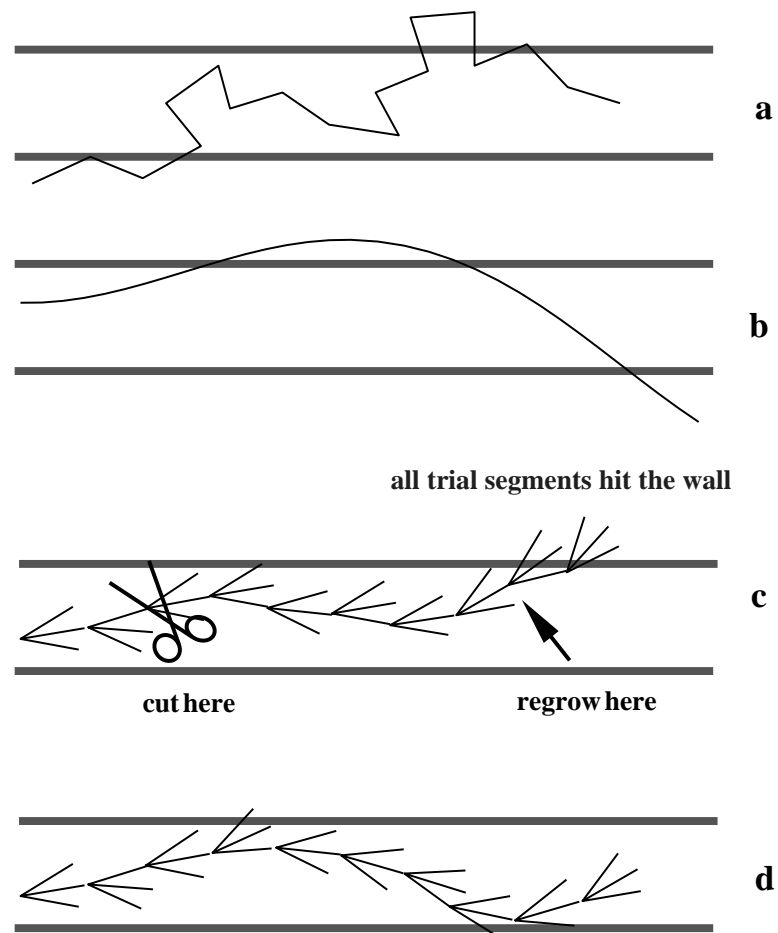\end{aligned}
\tag{3.28}
$$

FIGURE 3.2   Possible schemes to generate conformations of a worm-like chain. (a) Generate conformations of a freely jointed chain. (b) Generate subsequent segments according to the internal Boltzmann factors. (c) Configurational bias. (d) Configurational bias with an extra bias.

A naive way to simulate a worm-like chain would be to generate a very large number of completely random conformations of the freely jointed chain and compute the Boltzmann weight of the resulting conformation (Fig. 3.2-a). The problem with this approach is that the overwhelming majority of randomly generated conformations correspond to worm-like chains with a very high internal energy and probably with a very high external energy (and therefore a very small Boltzmann weight). Hence the statistical accuracy of this sampling scheme will be poor.

To alleviate the problem of high internal energies, we could sample the internal angles in the chain in such a way that the probability of finding a given angle is given

by the internal Boltzmann weight (Fig. 3.2-b). For every conformation thus generated, we compute the Boltzmann factor that corresponds to the interaction of the polymer with the hard wall of the cylinder. Thus, overlap of the polymer with the wall will give a Boltzmann factor equal to zero and no overlap will give one for the Boltzmann factor. With the average of these Boltzmann factors we can compute the confinement free energy.

This second approach is obviously superior to the first scheme. However, in many practical situations it will still yield poor statistics, because most ideal chain conformations will still not correspond to energetically favourable situations for the confined chain, as most chains will have overlap with the tube. Hence the Boltzmann weights will, again, be zero for the majority of conformations and the statistical accuracy will not be very good.

The problem with both schemes described above, is that neither allows us to focus on those conformations that should contribute most to Z, namely the ones for which both the internal and external potential energy are not much larger than a few $k_B T$ per degree of freedom. As the external energy is either zero for non overlap or infinity for overlap of the polymer with the hard wall, only non-overlapping conformations will contribute to Z. It would clearly be desirable to *bias* the sampling towards such favourable conformations.

One solution to this problem is to use the 'configurational-bias Monte Carlo' sampling scheme for continuously deformable molecules [61, 64]. In this scheme, the construction of chain conformations proceeds segment by segment. To add a segment, we generate a fixed number of trial segments, calculate for each trial segment the Boltzmann factor associated with the interaction with the wall and select the new segment with a probability proportional to that Boltzmann factor. Thus we will never choose a segment that has overlap with the tube, as this probability is equal to zero (Fig. 3.2-c). If we have grown a whole polymer, we cut the chain at a random position, regrow part of the chain at one or the other end and accept the new conformation with a certain probability, that is given in the Appendix of this chapter and is based on the condition of detailed balance. The advantage of this scheme is that we can rapidly generate large conformational changes and a conformation that hits the wall will immediately be rejected.

Nevertheless, the problem remains that when the polymer is grown or regrown, there is still a large probability that the polymer will encounter the wall at a large angle, as the width of the orientational distribution of the polymer after ℓ steps is equal to $\ell \langle \theta^2 \rangle$ with $\langle \theta^2 \rangle$ the width of the orientational distribution after one step.

Fig.	L	D	l_P
3.3	10-700	0.80	60.00
3.4	500	0.30-1.00	60.00
3.5	500	0.60	15.00-60.00
3.6	512	0.60	60.00
3.7	512	0.60	60.00
3.8	512	0.40-1.00	20.00-60.00
3.9	512	0.40-1.00	20.00-60.00

TABLE 3.1   Parameters characterising the simulations of a polymer in a tube. The table shows the values for the length of the polymer L, for the persistence length l_P, and for the diameter of the cylinder used in our simulations. The first column refers to the number of the figure. If one single value is shown in the table, we kept that parameter fixed at that value, otherwise the range will be shown, wherein the value of that parameter is varied.

Because the trial segments are generated according to the internal Boltzmann factors, all trial segments will probably hit the wall and no trial segment will make such a large turn, that the polymer can go from the wall, or if it does, it will do so in a conformation with a high internal energy and therefore a small statistical weight. As a consequence, the statistical accuracy of this sampling scheme will be poor. We therefore introduced an extra bias into our computational scheme and the polymer will now be guided smoothly to and from the wall of the cylinder (Fig. 3.2-d). The trial segments will now not be generated according to the Boltzmann factors of the internal energy, but distributed around a new unit vector $\hat{v}$, that denotes the "bias" direction for the new segment. This vector $\hat{v}$ depends on the radial distance of the segment to the axis of the cylinder and on the orientation of the $(i-1)$th segment. Of course, in our Monte Carlo sampling we should correct for this bias. In the Appendix of this chapter this computational scheme is described in detail.

3.4   Results and Discussion

As it is our aim to test the dependence of the confinement free energy of worm-like chains on the parameters characterising the chain and the confining tube, simulations were carried out on chains with lengths between 10 and 700 segments and with persistence lengths of 15 to 60 segments in tubes of diameters of 0.3 to 1.0. The parameters
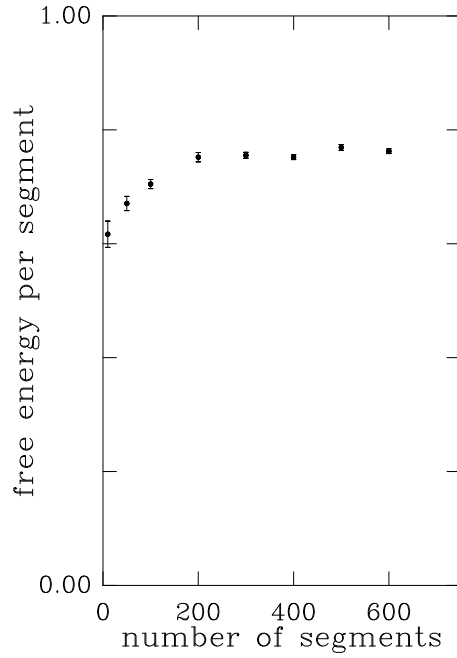
FIGURE 3.3   A plot of the confinement free energy per segment of a polymer
with persistence length l_P =60 in a tube with diameter D =0.80 versus the number
of segments of the polymer.

characterising the various simulations that we have performed have been collected in
table 3.1. Fig. 3.3 shows a plot of the confinement free energy per segment versus
the number of segments of the polymer. In order to estimate the statistical error of
the confinement free energy, 40 independent simulations were performed. In each
simulation we regrew the polymer 100 times. The confinement free energy per segment
is found to approach a constant value for $L \gg l_P$, as expected, because the total free
energy of the chain is an extensive quantity. In what follows, we shall always discuss
simulations of worm-like chains with $L \gg l_P$.

The dependence of the free energy on the diameter of the cylinder and on the
persistence length is shown, respectively, in Fig. 3.4 and 3.5. The free energy is found
to scale with the diameter of the cylinder as $\Delta F_c \sim D^a$, where a = -0.66 $\pm$ 0.07
and with the persistence length l_P as $\Delta F_c / k_B T \sim l_P^b$, where b = -0.31 $\pm$ 0.05. This
should be compared with the value a = 2/3 and b = -1/3 predicted by the theory of
Ref. [42, 43, 50–52]. Thus our data are consistent with the scaling relations theoretically
predicted.

Let us next consider if we can gain a better physical understanding of the scaling
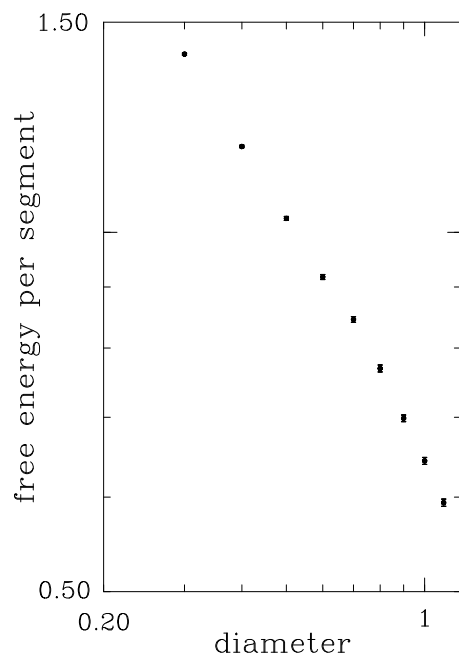behaviour of the confinement free energy. Clearly, the physical origin of the confinement

FIGURE 3.4   A plot of the confinement free energy per segment of a polymer of length L=500 and persistence length l_P=60 in a tube versus the diameter D of this tube.
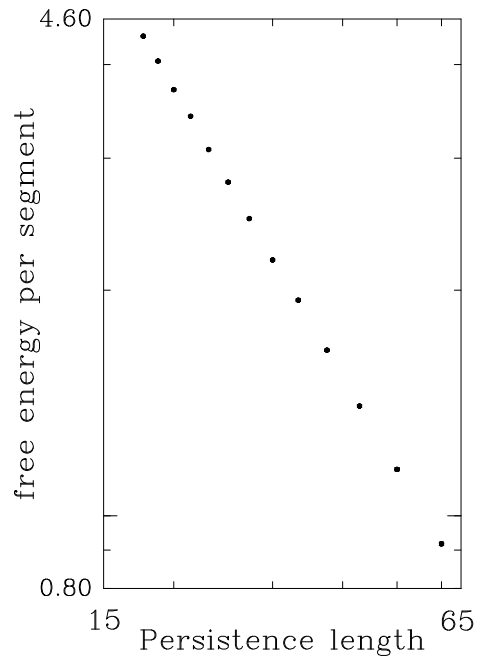

FIGURE 3.5   A plot of the confinement free energy per segment of a polymer of length L =500 in a tube with diameter D =0.60 versus the persistence length l_P of the polymer.

free energy is the suppression of chain fluctuations. Specifically, Helfrich's theory is based on the argument that the scaling behaviour is a result of the *constant* suppression of all Fourier modes of the chain fluctuations. Our simulations allow us to test this prediction in detail. In Fig. 3.6 the difference of $1/\langle a_q^2 \rangle$ between the confined worm-like chain and the free polymer is shown as a function of q. For small q the difference appears to be constant in agreement with Eq. 3.7. However, we also observe, somewhat surprisingly, that the high-q Fourier modes of the confined chain are *enhanced* with respect to the free chain. It seems likely that the enhancement of the amplitude of the high-q modes in a confined chain is caused by the influence of the hard wall potential on the conformations of the chain. Loosely speaking, one can imagine that the highly non-linear chain-wall interactions will enhance the "overtones" in the chain, at the expense of the low-q modes. However, our present simulation, where we have used rather small values for the tube diameter D, do not allow us to investigate this phenomenon systematically. In any event, as we shall argue below, the confinement free energy is completely dominated by the low-q chain fluctuations that are suppressed rather than enhanced. If we magnify the plot of $1/\langle a_q^2 \rangle$ versus q in the low-q region, also shown in Fig. 3.6, we see that the suppression of the Fourier modes varies by some 20% for $0 \le q \le 0.13$. This variation is not accounted for by the Helfrich theory. We expect that the fact that the suppression of the low-q Fourier modes is not completely constant will affect the quantitative prediction of the Helfrich theory, but not the scaling behaviour.

Let us now test Helfrich's prediction for the amplitude of the low-q Fourier modes, i.e., τ in Eq. 3.12. In order to compute τ, we must know the mean-square displacement of a polymer in a tube (μ in Eq. 3.11). Helfrich gives the estimate $\mu = 1/24$. However, we can "measure" μ in our simulations by computing $\langle r^2 \rangle / D^2$. We find $\mu = 0.073 \pm 0.001$. If we insert this value of μ in Eq. 3.12, we find that $\tau = 4.18 \pm 0.08 \times 10^3$. As can be seen from the magnified part of Fig. 3.6, this value of τ is indeed within the range found in our simulations. We note that if, in contrast, we used Helfrich's estimate $\mu = 1/24$, we would have seriously overestimated the value of τ (viz. $\tau = 8.84 \times 10^3$).

Helfrich's theory also gives a prediction for the prefactor in Eq. 3.4, namely $c = \mu^{-1/3}$. In Fig. 3.4 and 3.5 the prefactor is $c = 2.46 \pm 0.07$. With $\mu = 0.073 \pm 0.001$, we find $c = 2.39 \pm 0.01$. The actual value for c agrees within the statistical error with this value and turns out to be slightly lower than the value, obtained by using the value $\mu = 1/24$.

In order to investigate the scaling behaviour of the suppression of these Fourier spectra, we compute the ratio $R(q)$ of the mean square amplitudes of the restricted chain and the free polymer for several values for the diameter of the tube and the persistence length. An example of the q-dependence of $R(q)$ is shown in Fig. 3.7. As before
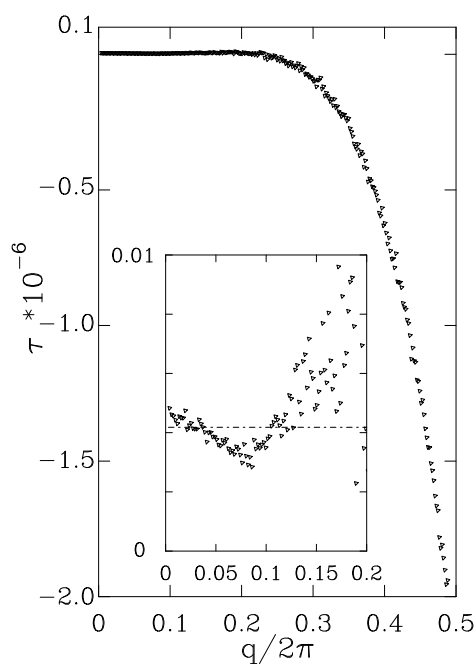
FIGURE 3.6   A plot of $\tau = 1/\langle a_q^2 \rangle_{\text{restr}} - 1/\langle a_q^2 \rangle_{\text{free}}$ of a polymer with length L=512 and persistence length l_P=60 in a tube with diameter D=0.60 as a function of q. The inset shows a magnification of the low-q region, where the dash-dot line denotes the value of τ based on Helfrich's theory (for details see text).
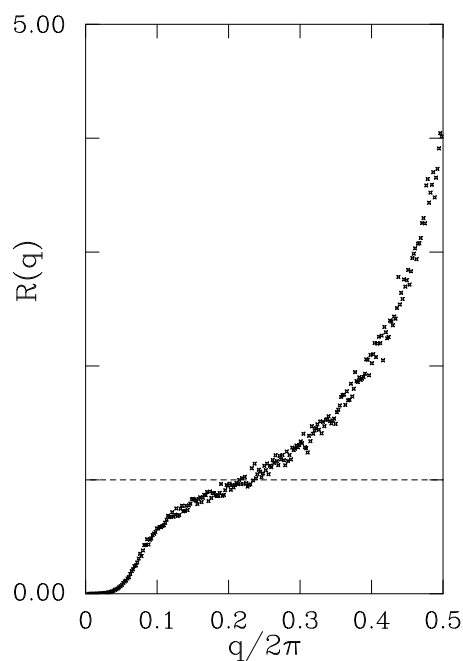

FIGURE 3.7   A plot of the ratio of the mean-square amplitudes of the confined and the free chain as a function of q with D= 0.60 and l_P=60.
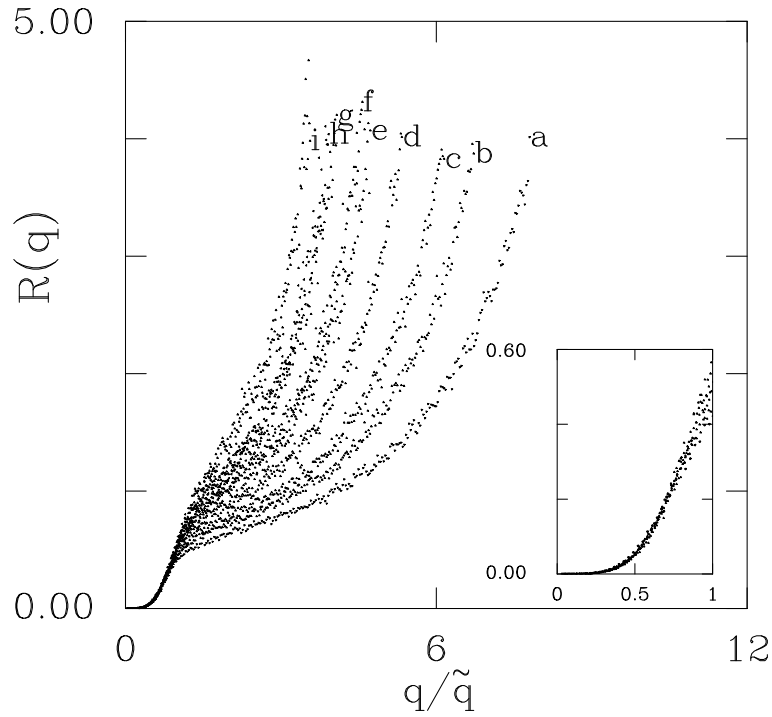
FIGURE 3.8 A plot of the ratio of the mean-square amplitudes of the confined and the free chain as a function of $q/\tilde{q}$ with the following values for, respectively, D and l_P: (a) 1.00, 60; (b) 0.80, 60; (c) 0.70, 60; (d) 0.60, 60; (e) 0.50, 60; (f) 0.60, 40; (g) 0.60, 30; (h) 0.40, 60; (i) 0.60, 20. The inset shows a magnification of the low-$q/\tilde{q}$ region.

we see the strong suppression of low-q Fourier modes of the chain fluctuations and an enhancement of the high-q modes. The Helfrich theory predicts that $R(q)$ becomes a universal function of $q/\tilde{q}$, namely $R(q) = q^4/(q^4 + \tilde{q}^4)$ (Eq. 3.15). Below, we shall test this functional form of $R(q)$. First, we simply assume that R is an, as yet unspecified, universal function of $q/\tilde{q}$. We can then measure the dependence of $\tilde{q}$ on D and l_P in the following way. We determine the value of q for which $R(q)$ has a given value. As R is a universal function of $q/\tilde{q}$, a fixed value of R correspond to a fixed value of $q/\tilde{q}$, say x. If we now measure how this specific value of q depends on D and l_P, we immediately determine the dependence of $\tilde{q} = q/x$ on D and l_P. Following this procedure, we found that $\tilde{q}$ scales with the diameter of the cylinder as $\tilde{q} \sim D^{a_1}$, where $a_1 = \text{-}0.69 \pm 0.06$ and with the persistence length l_P as $\tilde{q} \sim l_P^{b_1}$, where $b_1 = \text{-}0.37 \pm 0.04$. This should be compared with the value $a_1 = \text{-}2/3$ and $b_1 = \text{-}1/3$ predicted by Helfrich's theory [52, 59, 60].
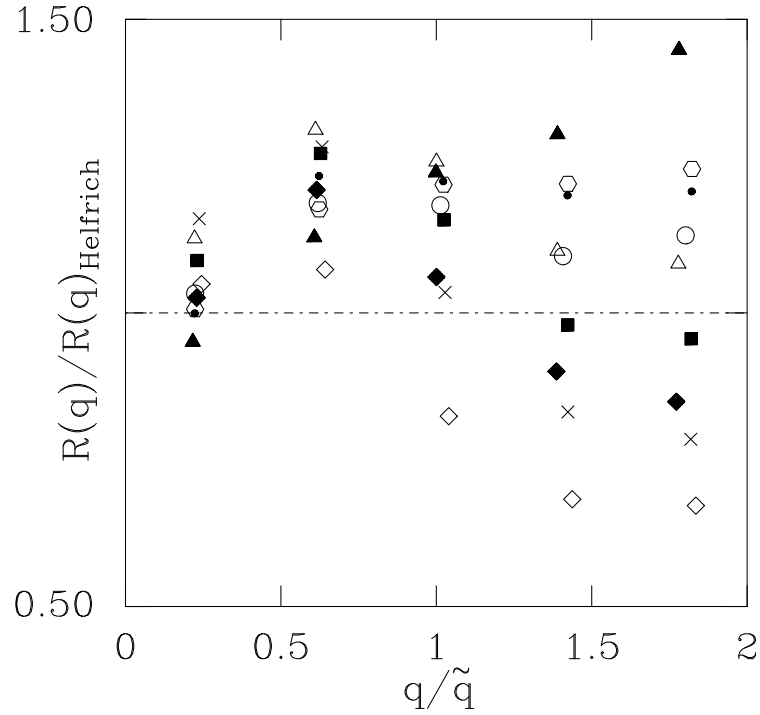
FIGURE 3.9   A plot of the ratio of the mean-square amplitudes of the confined and the free chain divided by the ratio predicted by Helfrich as a function of $q/\tilde{q}$ with the following values for, respectively, D and l_P, open diamond: 1.00, 60; cross: 0.80, 60; solid diamond: 0.70, 60; solid square: 0.60, 60; open triangular: 0.50, 60; open circle: 0.60, 40; open hexagon: 0.60, 30; dot: 0.40, 60; solid triangular: 0.60, 20.

In order to determine the prefactor c_1 in Eq. 3.17, we have fitted our Fourier spectra with the function $R(q) = q^4/(q^4 + \tilde{q}^4)$, where $\tilde{q} = c_1/D^{2/3}l_P^{1/3}$. Fig. 3.8 and 3.9 show that for $q \leq \tilde{q}$ (i.e., $R(q) \leq 1/2$) the Fourier spectra agree very well with Helfrich's assumption. We find the best fits, using $c_1 = 1.63 \pm 0.06$, which should be compared with the value $c_1 = 1.69 \pm 0.01$ using the value for $\mu = 0.073 \pm 0.001$ that follows from the simulations. The value for the prefactor, obtained by using $\mu = 1/24$ yields an overestimate for c_1.

In summary, our simulations of the excess free energy of a worm-like chain confined in a tube appear to be in quantitative agreement with the scaling behaviour predicted by the theories of Helfrich, Khokhlov and Semenov and Odijk [51, 50, 52, 42, 43]. In addition, we find that the theory of Helfrich yields a prediction for the absolute confinement free energy, that is in good, but not perfect, agreement with our simulations.

We find that the amplitude of the short-wavelength modes of the chain fluctuations are seriously underestimated in the Helfrich theory. However, for the estimate of the confinement free energy, those modes are relatively unimportant. Nevertheless, these high-q modes may turn out to be quite important for other physical properties of confined chains (e.g. the scattering behaviour [65]). For this reason, a better theoretical understanding of the behaviour of short-wavelength modes of confined worm-like chains appears highly desirable.

Appendix

In order to compute the confinement free energy of a worm-like chain in a tube, we apply the following 'recipe' to construct a conformation of a chain of L segments. The construction of chain conformations proceeds segment by segment. Let us first consider the addition of one such segment. To be specific, let us assume that we have already grown $i-1$ segments of the chain, and that we are trying to add segment i. This is done as follows:

1. Generate a fixed number (say k) trial segments. The orientations of the trial segments are distributed according to the internal Boltzmann weight $P^{\mathrm{id}}_{\hat{\mathbf{w}}_{i-1}\hat{\mathbf{w}}_j} = \exp(-\beta u^{\mathrm{id}}_{\hat{\mathbf{w}}_{i-1}\hat{\mathbf{w}}_j})$ associated with the internal bending energy times a weight function:

$$g_j = \frac{P_{\hat{\mathbf{v}}\hat{\mathbf{w}}_j}}{P^{\mathrm{id}}_{\hat{\mathbf{w}}_{i-1}\hat{\mathbf{w}}_j}} \qquad (3.29)$$

with

$$P_{\hat{\mathbf{v}}\hat{\mathbf{w}}_j} = \frac{1}{B}\exp\left[-\beta\,C(r_{xy})\theta^2_{\hat{\mathbf{v}}\hat{\mathbf{w}}_j}\right] \qquad (3.30)$$

where r_{xy} is the radial distance of the previous segment to the axis of the tube and where $\theta_{\hat{\mathbf{v}}\hat{\mathbf{w}}_j}$ is the angle between the unit vectors $\hat{\mathbf{w}}_j$ and $\hat{\mathbf{v}}$ that denote, respectively, the orientation of the j th trial segment and the bias orientation, as yet unspecified, for the i th segment. The unit vector $\hat{\mathbf{v}}$ depends on the unit vector that specifies the orientation of the previous segment $\hat{\mathbf{w}}_{i-1}$ and on the radial distance of the previous segment to the axis of the cylinder. The normalisation constant B is equal to $\int d\hat{\mathbf{w}}P_{\hat{\mathbf{v}}\hat{\mathbf{w}}_j}$. The bending constant $C(r_{xy})$ is also dependent on the radial distance of the previous segment to the axis of the cylinder:

$$C(r_{xy}) = \frac{C}{1 - (2r_{xy}/D)^2}$$

For the bias direction, we took the following boundary conditions

$$
\hat{v}(\hat{w}_{i-1}, r_{xy}) = \begin{cases} \hat{e}_z & \text{if } r_{xy} = D/2 \\ \hat{e}_z & \text{if } \hat{w}_{i-1} \cdot \hat{e}_z = 0 \\ \hat{w}_{i-1} & \text{if } r_{xy} = 0 \end{cases} \tag{3.31}
$$

with $\hat{e}_z$ along the axis of the cylinder. An equation for the bias direction of segment i that satisfies these conditions is

$$
\hat{v}(\hat{w}_{i-1}, r_{xy}) = \frac{\vec{v}(\hat{w}_{i-1}, r_{xy})}{|\vec{v}(\hat{w}_{i-1}, r_{xy})|} \tag{3.32}
$$

where $\vec{v}(\hat{w}_{i-1}, r_{xy})$ is equal to

$$
\vec{v}(\hat{w}_{i-1}, r_{xy}) = (\frac{D}{2} - r_{xy})(\hat{w}_{i-1} \cdot \hat{e}_z)\,\hat{w}_{i-1} +
$$
$$
r_{xy}(1 - \hat{w}_{i-1} \cdot \hat{e}_z)\,\hat{e}_z \tag{3.33}
$$

We denote the different trial segments by indices $1, 2, \cdots k$. Now the probability to generate a given subset $\{\hat{w}\}_i$ of k trial segments with orientations $\hat{w}_1$ through $\hat{w}_k$ is equal to

$$
\begin{aligned}
P_{\{\hat{w}\}_i} &= \frac{1}{B^k} \prod_{j=1}^{k} d\hat{w}_j\, P^{\text{id}}_{\hat{w}_{i-1}\hat{w}_j}\, g_j \\
&= \frac{1}{B^k} \prod_{j=1}^{k} d\hat{w}_j\, P_{\hat{v}\hat{w}_j}
\end{aligned} \tag{3.34}
$$

2. For all k trial segments, the 'external' Boltzmann factor $\exp(-\beta u^{\text{wall}}_{\hat{w}_j})$ is computed, where $u^{\text{wall}}_{\hat{w}_j}$ is the potential energy of the j th trial segment of the polymer with conformation Γ_w due to interaction with the wall of the cylinder.

3. Select one of the trial segments, say $\hat{w}_i$, with a probability

$$
P^{\text{wall}}_{\hat{w}_i} = \frac{\exp(-\beta u^{\text{wall}}_{\hat{w}_i})}{Z_{\{\hat{w}\}_i}} \tag{3.35}
$$

where we have defined

$$
Z_{\{\hat{w}\}_i} \equiv \sum_{j=1}^{k} \exp(-\beta u^{\text{wall}}_{\hat{w}_j})
$$

The subscript $\{\hat{w}\}_i$ means that $\hat{w}_i$ is one of the segments of the subset, so $\hat{w}_i \in \{\hat{w}\}$.

4. Add this segment as segment i to the chain and store the corresponding partial "Rosenbluth weight" [61]:

$$\omega_i = Z_{\{\hat{\mathbf{w}}\}_i}/k \qquad (3.36)$$

and the weight-factor g_i (Eq. 3.29).

The desired ratio Z/Z^{id} is than equal to the average value (over many trial chains) of the product of the partial Rosenbluth weights times the reciprocal partial weight-factors divided by the average value of the product of the reciprocal partial weight-factors:

$$Z/Z^{\text{id}} = \frac{\left\langle \prod_{i=1}^{L} \omega_i \cdot g_i^{-1} \right\rangle_g}{\left\langle \prod_{i=1}^{L} g_i^{-1} \right\rangle_g} = \langle \prod_{i=1}^{L} \omega_i \rangle \qquad (3.37)$$

where the angular brackets with the subscript g denotes an average over sampling distribution $P_{\hat{\mathbf{v}}\hat{\mathbf{w}}_j}$ and not the distribution $P^{\text{id}}_{\hat{\mathbf{w}}_{i-1}\hat{\mathbf{w}}_i}$. This is similar to the Umbrella Sampling [66], where the desired average will be obtained by a biased sampling. The advantage of this scheme is that step 3 biases the sampling towards energetically favourable conformations.

However, it still remains to be shown that equation 3.37 is, in fact, correct. To this end, we first consider the probability with which we generate a given chain conformation. This probability is the product of a number of factors. We can first derive these factors for one segment, and then later extend the result to the complete chain.

We wish to compute the average of ω_i, over all possible sets of trial segments and all possible choices of the segment. We must sum over all $\hat{\mathbf{w}}_i$ in a set and integrate over all orientations $\prod_{j=1}^{k} d\hat{\mathbf{w}}_j$ to get all possible sets of trial segments.

$$\langle \omega_i \rangle = \frac{\langle \omega_i \cdot g_i^{-1} \rangle_g}{\langle g_i^{-1} \rangle_g} = \frac{\int P_{\{\hat{\mathbf{w}}\}_i} \sum_{i=1}^{k} P^{\text{wall}}_{\hat{\mathbf{w}}_i} \omega_i \cdot g_i^{-1}}{\int P_{\{\hat{\mathbf{w}}\}_i} g_i^{-1}} \qquad (3.38)$$

In the numerator the summation over the external Boltzmann factors $Z_{\{\hat{\mathbf{w}}\}_i}$ in the probability to select a trial segment ($P^{\text{wall}}_{\hat{\mathbf{w}}_i}$) will cancel the summation in the Rosenbluth factor ω_i.

$$\begin{aligned}
\langle \omega_i \rangle &= \int \prod_{j=1}^{k} d\hat{\mathbf{w}}_j \, P_{\hat{\mathbf{v}}\hat{\mathbf{w}}_j} \sum_{i=1}^{k} \frac{\exp(-\beta u^{\text{wall}}_{\hat{\mathbf{w}}_i})}{k} g_i^{-1} \\
&\quad \times \left(\int \prod_{j=1}^{k} d\hat{\mathbf{w}}_j \, P_{\hat{\mathbf{v}}\hat{\mathbf{w}}_j} g_i^{-1} \right)^{-1}
\end{aligned} \qquad (3.39)$$

As the labeling of the trial segments in Eq. 3.39 is arbitrary all k terms yield the same contribution. We now arrive at

$$\langle \omega_i \rangle = k \int d\hat{\mathbf{w}}_i \, P_{\hat{\mathbf{v}}\hat{\mathbf{w}}_i} \frac{P^{\mathrm{id}}_{\hat{\mathbf{w}}_{i-1}\hat{\mathbf{w}}_i}}{P_{\hat{\mathbf{v}}\hat{\mathbf{w}}_i}} \frac{\exp(-\beta u^{\mathrm{wall}}_{\hat{\mathbf{w}}_i})}{k} \int \prod_{j=1, j \neq i}^{k-1} d\hat{\mathbf{w}}_j \, P_{\hat{\mathbf{v}}\hat{\mathbf{w}}_j}$$

$$\times \left(\int \prod_{j=1, j \neq i}^{k-1} d\hat{\mathbf{w}}_j \, P_{\hat{\mathbf{v}}\hat{\mathbf{w}}_j} \int d\hat{\mathbf{w}}_i \, P^{\mathrm{id}}_{\hat{\mathbf{w}}_{i-1}\hat{\mathbf{w}}_i} \right)^{-1}$$

The integrals over the $k-1$ orientations in the numerator will cancel the $k-1$ integrals in the denominator. Thus the final equation is

$$\langle \omega_i \rangle = \frac{\int d\hat{\mathbf{w}}_i \exp[-\beta(u^{\mathrm{id}}_{\hat{\mathbf{w}}_{i-1}\hat{\mathbf{w}}_i} + u^{\mathrm{wall}}_{\hat{\mathbf{w}}_i})]}{\int d\hat{\mathbf{w}}_i \exp[-\beta u^{\mathrm{id}}_{\hat{\mathbf{w}}_{i-1}\hat{\mathbf{w}}_i}]} = \frac{Z_i}{Z_i^{\mathrm{id}}} \tag{3.40}$$

The subscript in Eq. 3.40 denotes that this expression holds for the ith segment. The extension to a polymer of L segments is similar. Note that with this scheme Z_i/Z_i^{id} is equal to one, when the cylinder is taken away, so when $u^{\mathrm{wall}}_{\hat{\mathbf{w}}_i} = 0$. It is not necessary to sample over a large distribution; the correct answer is immediately obtained.

For the configurational-bias method, we used the detailed balance condition [61] in the Metropolis form:

$$\mathrm{acc}\,(a \mid b) = \min \left(1, \frac{P_a / \exp(-\beta U_a)}{P_b / \exp(-\beta U_b)} \right) \tag{3.41}$$

where P_a and P_b are, respectively, the probabilities that the chain is in conformation a and b. If we now impose the 'super-detailed' balance condition, we have to consider the probability of generating a new chain via one particular choice of trial directions $\{\hat{\mathbf{w}}\}_i$ and of choosing a set of trial directions $\{\hat{\mathbf{w}}'\}_i$ from all possible sets that contains the old configuration. The probability of generating a new chain of L segments via the set $\{\hat{\mathbf{w}}\}_i$ and of choosing the set $\{\hat{\mathbf{w}}'\}_i$ will now be equal to the probability to generate the old set of trial directions $\{\hat{\mathbf{w}}'\}_i$ excluding the old orientation (denoted by $P_{\{\mathrm{rest}'\}_i}$, where $\{\mathrm{rest}'\}$ denotes the set of $k-1$ orientations of $\{\hat{\mathbf{w}}'\}_i$ excluding the old orientation) times the probability to generate a new set of trial directions $\{\hat{\mathbf{w}}\}_i$ that contains the new orientation (i.e., $P_{\{\hat{\mathbf{w}}\}_i}$) times the probability to select this new orientation (i.e., $\exp(-\beta u^{\mathrm{wall}}_{b_i})/Z_{\{\hat{\mathbf{w}}\}_{b_i}}$).

$$P_b = \prod_{i=1}^{L} P_{\{\hat{\mathbf{w}}\}_i} \, P_{\{\mathrm{rest}'\}_i} \frac{\exp(-\beta u^{\mathrm{wall}}_{b_i})}{Z_{\{\hat{\mathbf{w}}\}_{b_i}}} \tag{3.42}$$

where $P_{\{\hat{\mathbf{w}}\}_i}$ will be given by Eq. 3.34. If $U_b = \sum_{i=1}^{L} u_{b_i}^{\text{id}} + u_{b_i}^{\text{wall}}$, we arrive at

$$P_b / \exp\left(-\beta U_b\right) = \prod_{i=1}^{L} \frac{P_{\{\text{rest}\}_i} \, P_{\{\text{rest}'\}_i} \, g_{b_i}}{BZ_{\{\hat{\mathbf{w}}\}_{b_i}}} \tag{3.43}$$

Substitution of Eq. 3.43 in Eq. 3.41 gives

$$\text{acc}\,(a \mid b) = \min(1, W_b G_b^{-1} / W_a G_a^{-1}) \tag{3.44}$$

with

$$G_b = \prod_{i=1}^{L} g_{b_i} \quad \text{and} \quad W_b = \prod_{i=1}^{L} \frac{Z_{\{\hat{\mathbf{w}}\}_{b_i}}}{k} = \prod_{i=1}^{L} \omega_{b_i} \tag{3.45}$$

In words, the configurational-bias Monte Carlo (CBMC) scheme works as follows:

1. Generate a trial conformation by using the Rosenbluth scheme (i.e., Eq. 3.42) to regrow the entire molecule, or part thereof.

2. Compute the Rosenbluth weights times the weight-functions.

$$W_{\text{old}} G_{\text{old}}^{-1} \text{ and } W_{\text{trial}} G_{\text{trial}}^{-1}$$

of the trial conformation and of the old conformation.

3. Accept the trial move with a probability

$$\min(1, W_{\text{trial}} G_{\text{trial}}^{-1} / W_{\text{old}} G_{\text{old}}^{-1})$$

4 A Two-Dimensional System of Semiflexible Polymers

In this chapter, we present computer simulations of a two-dimensional system of semiflexible polymers consisting of infinitesimally thin hard segments connected by joints of variable flexibility. As the density is increased, we observe a transition from the isotropic to a "nematic" phase with quasi-long-range orientational order. In addition, we study the scaling behaviour of the elastic constants for splay and bend in the nematic phase and find good agreement with the relevant theoretical predictions.

4.1 Introduction

In this chapter, we will study a two-dimensional system of semiflexible polymers. The study of semiflexible polymers was initiated by Flory in 1956 [67]. Still, the statistical behaviour of bulk systems of semiflexible polymers is incompletely understood. Flory modeled the polymers by self-avoiding random walks on a three-dimensional lattice and defined the equilibrium flexibility as the fraction of bonds that are bent. In his mean-field calculation, he obtained a first-order phase transition from an isotropic to an orientationally ordered phase, when the flexibility exceeds a critical value. Other mean-field theories [68–70] also predict this phase transition for three-dimensional lattice polymers. However, these results have been disputed on the basis of several exactly solvable models for three-dimensional polymers which show a continuous phase transition [71, 72]. It would seem that computer simulations could be used to investigate the phase behaviour of semiflexible polymers. However, somewhat surprisingly, long-range orientational order has thus far not been observed in computer simulations of two- and three-dimensional athermal lattice polymers [73–76]. In particular, in the simulations of

Baumgärtner [73] (athermal polymers on a square and cubic lattice), Kolinsky *et al.* [74] (tetrahedral lattice) and Rodriguez *et al.* [75] (bond fluctuation model in two dimensions) only a transition to ordered domains is observed. The linear dimension of these domains is of the order of the contour length of the polymer. Only upon inclusion in the model of an attractive interaction between two parallel oriented nearest neighbour segments, which may or may not belong to different chains, is an isotropic-nematic phase transition observed [73, 74]. The reason why the athermal semiflexible polymers do not seem to form an orientationally ordered phase may, at least in part, be due to the fact that the simulations referred to above were all performed on lattice models. It is therefore interesting to consider an off-lattice system of continuously deformable polymers. Theories for the phase behaviour of off-lattice semiflexible polymers all do predict an isotropic to nematic phase transition in three dimensions [42, 43]. Recently, a continuous isotropic-nematic phase transition was predicted theoretically for a two-dimensional system of semiflexible polymers [77].

In this chapter, we present first a simulation study of a two-dimensional off-lattice model of semiflexible polymers. Simulations of a three-dimensional system of continuously deformable polymers will be described in the next chapter. In particular, we investigate in this chapter whether this two-dimensional system exhibits an isotropic to nematic phase transition. We therefore performed a series of grand canonical Monte Carlo (GCMC) simulations [78] of semiflexible polymers with varying flexibility. For infinitely stiff polymers, i.e., needles, simulations have been performed earlier by Frenkel and Eppenga [79]. In these simulations, an isotropic to "nematic" phase transition of the Kosterlitz-Thouless type was observed.

We found that the conventional Monte Carlo schemes (Metropolis sampling and reptation) were not sufficiently efficient to ensure rapid equilibration. For a faster equilibration of the polymers we used the configurational-bias Monte Carlo (CBMC) method [80, 81]. This method will be discussed in Sec. 4.2. For more technical details on the implementation of the CBMC method in the GCMC simulation, we refer to the Appendix of this chapter. In Sec. 4.3, we present the results and discussion.

4.2   Model and Computational Technique

We performed GCMC simulations of a two-dimensional system of semiflexible polymers. The chains consist of ten infinitesimally thin hard segments connected to each other. The bending energy for a joint between two segments i and $i-1$ is given by Eq. 3.26 and the relation between the persistence length and the bending elastic constant C by Eq. 2.14. Again, the segment length was chosen as our unit of length.

In a GCMC simulation the chemical potential, the temperature, and the "volume" of the system are fixed quantities. The diameter of the periodic box used in our simulations was 30 segment lengths. In our Monte Carlo simulations we had to ensure that no trial move would result in a hard-core overlap of the polymer segments. To test whether a trial move generated such an overlap, we used the criterion described in Ref. [79]. The following trial moves were performed:

- Reptation: Remove a segment from one end of the polymer. Generate one trial segment at either end of the polymer in such a way that the probability of finding a given angle with the previous segment is given by the Boltzmann weight associated with the bond bending. Accept this segment if it has no overlap with another segment. If the move is not accepted, reset the segment to its original position.

- Regrow a whole polymer at a random position and with a random orientation using the CBMC method [80]. Below, the procedure is only briefly sketched. For more technical details on the construction of a chain, the reader is referred to the Appendix of this chapter. The construction of a chain proceeds segment by segment. To add a segment, we generate a fixed number of trial segments according to the internal (bond-bending) Boltzmann factors. The Boltzmann factors, associated with the nonbonded interaction, are either zero (if the segment overlaps with another) or one (if there is no overlap). We refer to the Boltzmann factors associated with nonbonded interaction as "external" to distinguish them from the "internal" Boltzmann factors associated with bond bending. We select the new segment with a probability that is proportional to the external Boltzmann factor. The new polymer conformation will now be accepted with a certain probability that can be derived from the condition of detailed balance (see Ref. [80]).

- Remove or insert a polymer in the system. For the insertion of the polymer we used the same procedure as above. This trial move, insertion or removal, will be accepted with a probability that satisfies the condition of detailed balance and is described in more detail in the Appendix of this chapter.

In our simulations, we calculated the average number density ρ of the chains, the pressure P, and the elastic constants for the splay and the bend, respectively, K_1 and K_3, as a function of the imposed chemical potential μ and of the chosen persistence length l_P. The pressure is calculated by virtual volume changes. In this method, we use the fact that the pressure can be obtained by differentiation of the thermodynamic potential with respect to the volume. To this end we must compute the acceptance ratio [82] of

virtual trial moves that decrease and increase the volume of the system. For hard convex bodies, the acceptance of virtual expansions is always one and the method reduces to that described in Ref. [83]. However, in the present case for polymers there is a small but finite probability to reject virtual expansions. For the sake of comparison, we also computed the pressure by integrating the Gibbs-Duhem equation. This equation shows the relationship between a change in the temperature and pressure to a change in the chemical potential:

$$d\mu = -\frac{S}{N}dT + \frac{V}{N}dP \qquad (4.1)$$

We can now compute the pressure by integrating the Gibbs-Duhem equation at constant temperature:

$$dP = \rho\, d\mu \qquad (4.2)$$

In the nematic phase the orientational distribution function is symmetric around a preferred direction, i.e. the nematic director, which is denoted by the unit vector $\hat{n}_0$. A local deformation $\delta n(r)$ of the uniform alignment of the director results in an elastic restoring force. If the deformations are small, the restoring forces are proportional to the deformations. The constants of proportionality are called the Frank elastic constants, denoted by K_1 and K_3. The deformation free energy F_D for a two-dimensional nematic has the following form:

$$F_D = \int \frac{1}{2}K_1[\vec{\nabla}\cdot\hat{n}(r)]^2 + \frac{1}{2}K_3[\vec{\nabla}\times\hat{n}(r)]^2\, dr \qquad (4.3)$$

where $\hat{n}(r) = \hat{n}_0 + \delta n_0(r)$. Note that the local nematic director $\hat{n}(r)$ is normalised to unity, so that $\delta n_0(r)$ is perpendicular to $\hat{n}(r)$ and $\hat{n}_0$, i.e., $\delta(\hat{n}(r)\cdot\hat{n}(r)) = 2\hat{n}(r)\cdot\delta\hat{n}(r) \simeq 2\hat{n}_0\cdot\delta\hat{n}(r) = 0$. Defining the Fourier transforms:

$$\delta\hat{n}_0(r) = \frac{1}{(2\pi)^2}\int d\mathbf{q}\exp(i\mathbf{q}\cdot\mathbf{r})\mathbf{n}(\mathbf{q}) = \frac{1}{V}\sum_{\mathbf{q}}\exp(i\mathbf{q}\cdot\mathbf{r})\mathbf{n}(\mathbf{q})$$

$$\mathbf{n}(\mathbf{q}) = \int d\mathbf{r}\exp(-i\mathbf{q}\cdot\mathbf{r})\delta n_0(r)$$

where V is the volume of the system, yields

$$F_D = \frac{1}{2V}\sum_{\mathbf{q}} K_1[\mathbf{q}\cdot\mathbf{n}(\mathbf{q})]^2 + K_3[\mathbf{q}\times\mathbf{n}(\mathbf{q})]^2 \qquad (4.4)$$

If we decompose $\mathbf{q}$ in $(q_\parallel, q_\perp)$, where $q_\parallel$ and $q_\perp$ are the components parallel and perpendicular, respectively, to the nematic director $\hat{n}_0$, we arrive at

$$F_D = \frac{1}{2V}\sum_{\mathbf{q}} |\mathbf{n}(\mathbf{q})|^2(K_1 q_\perp^2 + K_3 q_\parallel^2) \qquad (4.5)$$

The equipartition theorem now yields

$$\langle |n(q)|^2 \rangle = \frac{V k_B T}{K_1 q_\perp^2 + K_3 q_\parallel^2} \tag{4.6}$$

The local nematic order parameter of a two-dimensional system of N polymers consisting of L segments is defined by

$$Q_{\alpha\beta}(\mathbf{r}) = \frac{1}{L} \sum_{k=1}^{N} \sum_{j=1}^{L} (2\hat{w}_\alpha^{k,j} \hat{w}_\beta^{k,j} - \delta_{\alpha\beta}) \delta(\mathbf{r} - \mathbf{r}_{k,j}) \tag{4.7}$$

where $\hat{w}_\alpha^{k,j}$ is the αth Cartesian coordinate of the unit vectors specifying the orientation of segment j of polymer k and $\mathbf{r}_{k,j}$ the position of this segment. The spatial average $\langle Q \rangle$ of $Q_{\alpha\beta}(\mathbf{r})$ is easily checked to be traceless and symmetric and can therefore be written as

$$\begin{aligned}
\langle Q \rangle &\equiv \frac{1}{V} \int d\mathbf{r} Q(\mathbf{r}) \\
&= \rho S (2\hat{n}_0 \hat{n}_0 - \mathbf{I})
\end{aligned} \tag{4.8}$$

where ρS is the positive eigenvalue of $\langle Q \rangle$ and $\hat{n}_0$ the corresponding normalised eigenvector, which is the global nematic director. Here ρ is the chain density and S the nematic scalar order parameter. Note that S vanishes in the isotropic phase and equals unity in the fully aligned nematic phase. We can now define a local deviation from the global order by means of:

$$\begin{aligned}
\delta Q(\mathbf{r}) &\equiv Q(\mathbf{r}) - \langle Q \rangle \\
&= 2\rho S (\hat{n}(\mathbf{r})\hat{n}(\mathbf{r}) - \hat{n}_0 \hat{n}_0) \\
&= 2\rho S (\hat{n}_0 \delta\hat{n}_0(\mathbf{r}) + \delta\hat{n}_0(\mathbf{r})\hat{n}_0 + \delta\hat{n}_0(\mathbf{r})\delta\hat{n}_0(\mathbf{r}))
\end{aligned} \tag{4.9}$$

If the deviations from the uniform alignment are small, then $\delta\hat{n}_0(\mathbf{r}) \perp \hat{n}_0$. Consequently, we obtain

$$\begin{aligned}
\langle |Q_{\parallel\perp}(q)|^2 \rangle &= \left\langle \left| \int \exp(-i\mathbf{q} \cdot \mathbf{r}) \delta Q_{\parallel\perp}(\mathbf{r}) d\mathbf{r} \right|^2 \right\rangle \\
&= 4S^2 \rho^2 \langle |n(q)|^2 \rangle \\
&= \frac{4S^2 \rho^2 V k_B T}{K_1 q_\perp^2 + K_3 q_\parallel^2}
\end{aligned} \tag{4.10}$$

where $\parallel$ and $\perp$ denote components parallel and perpendicular to $\hat{n}_0$.

Thus if we calculate $\langle |Q_{\parallel\perp}(q)|^2 \rangle$ for $\mathbf{q}$ parallel and perpendicular to the nematic director, we can compute the elastic constants K_1 and K_3. The analogous expression for 3D nematics was used in Ref. [84, 85].
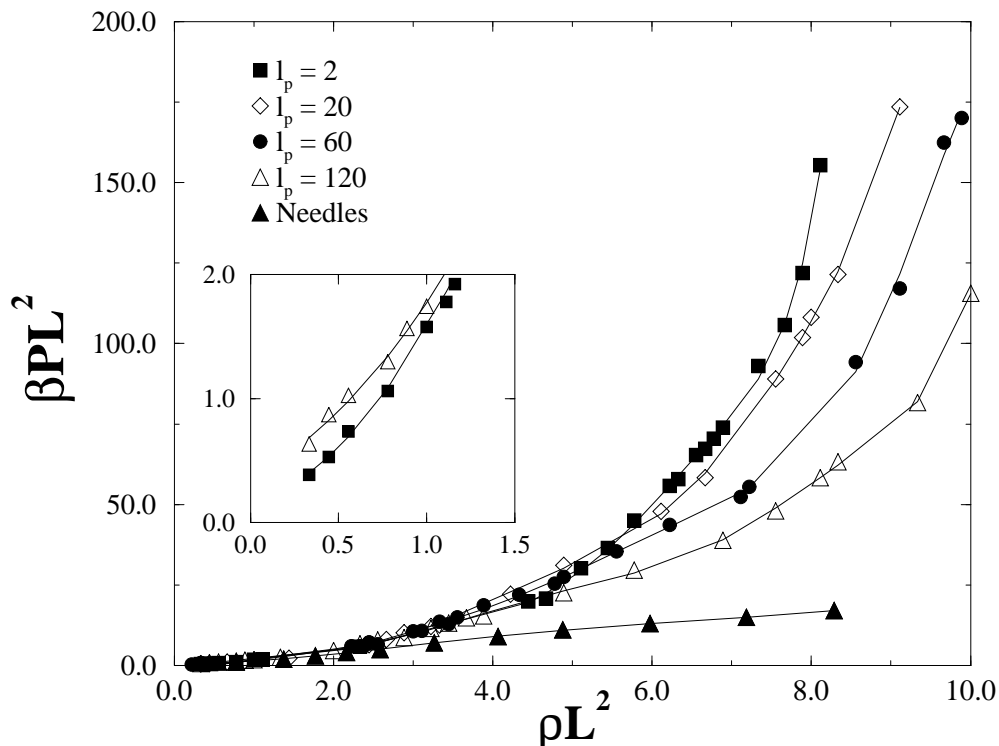
FIGURE 4.1   Pressure versus the density for different values for the flexibility of the two-dimensional semiflexible polymers with *L* the length of the polymer. The inset shows the pressure versus the density for semiflexible polymers with persistence length $l_P = 2$ and 120 in the low density limit.

4.3   Results and Discussion

We performed GCMC simulations of semiflexible polymers with different persistence length (l_P = 2, 20, 60, and 120) in order to investigate the influence of flexibility on the equation of state. In a GCMC simulation the chemical potential, the volume, and the temperature are fixed quantities; the pressure P and the chain density $\rho = N/V$ are fluctuating quantities. The chemical potential was chosen such that the dimensionless or reduced density ρL^2 varied from 0.2 to 10. The initial configuration from which the first runs were started was one in which all the polymers were directed in the same direction but randomly positioned in the periodic box. Subsequent runs were started from previously equilibrated configurations at a higher or lower chemical potential. Most runs consisted of $1 \times 10^5 - 1 \times 10^7$ trial moves per chain. Most trial moves were simple reptation moves. On average once every three reptation moves a polymer is completely
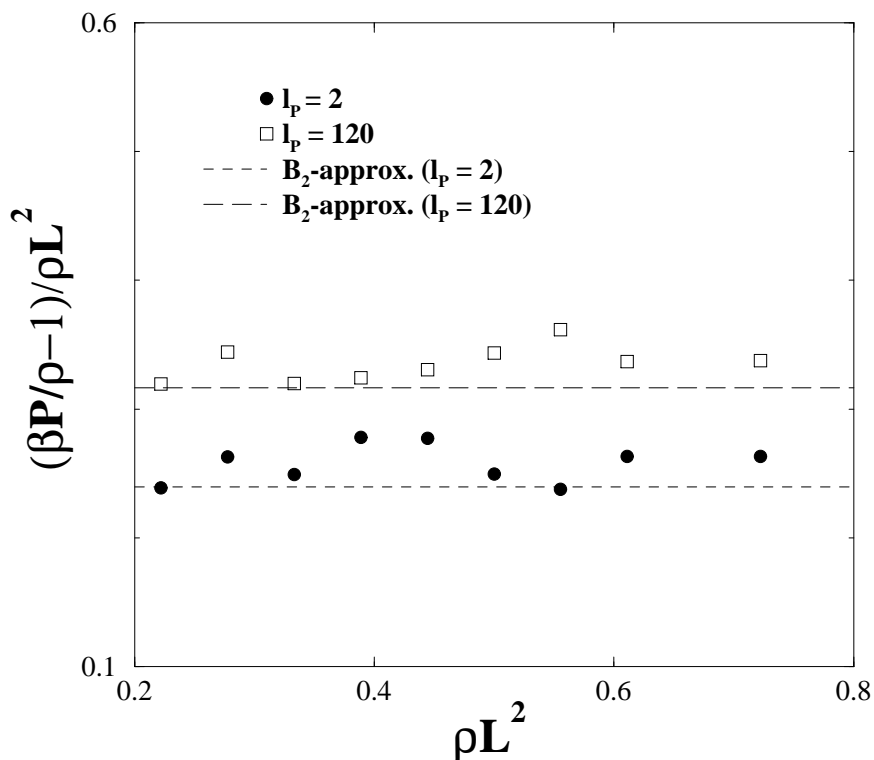
FIGURE 4.2 Pressure versus the density for semiflexible polymers of persistence length 2 (black circles) and 120 (open squares) in the low-density regime. The solid line and the dashed line correspond with the B_2 approximation for semiflexible polymers of, respectively, persistence length 2 and 120. L denotes the length of the polymer.

regrown at a random position in the periodic box using the CBMC method. Once every ten reptation moves, a trial move to insert or to remove a particle was attempted. In order to investigate the pressure dependence at low densities and the elastic constants in the nematic phase, canonical ensemble simulations (with fixed number of particles, volume and temperature) were performed for systems with ρL^2 ranging from 0.2 to 1 and from 10 to 70, respectively. Fig. 4.1 shows a plot of the pressure versus the density for different values of the persistence length of the polymers. For the sake of comparison the results for hard needles (Ref. [79]) have also been plotted in Fig. 4.1. Earlier simulations by Dickman [76] indicated that the pressure increases dramatically with increasing stiffness for a dilute system, but it is nearly independent of stiffness in dense systems [76]. However, for high densities we observe an increase in the pressure when the polymers become more flexible. This effect is to be expected because for dense systems the confinement free energy plays an important role. An increase in the
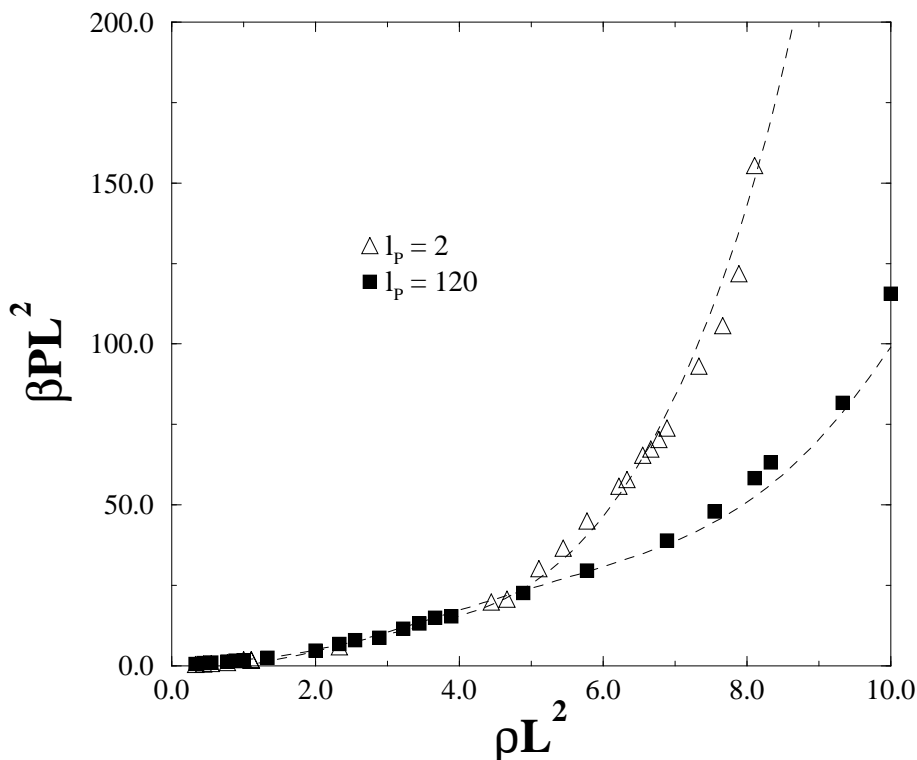
FIGURE 4.3 The pressure calculated by integration of the Gibbs-Duhem equation for persistence length $l_P = 2$ and 120 (dashed curves) and the pressure calculated by virtual volume changes (open triangles and black squares). L denotes the length of the polymer.

flexibility of the polymers results in a larger confinement free energy and the pressure will increase rapidly with larger flexibility [81]. At low densities, the pressure can be approximated by the virial expansion.

$$\beta P = \rho + B_2 \rho^2 + \cdots \tag{4.11}$$

For hard-core systems, the second virial coefficient B_2 is a measure of the pair excluded volume of the polymers. For flexible chains the excluded volume is smaller than for stiff chains and therefore we expect that the pressure is smaller for more flexible chains. At low densities ($\rho L^2 < 1$) we do indeed observe an increase in pressure with stiffness (see Fig. 4.1) and our results agree qualitatively well with those of Ref. [76] at low densities.

For the sake of comparison, we computed the virial coefficient B_2 numerically and plotted the virial expansion (Eq. 4.11) truncated at the second virial coefficient in Fig. 4.2. For semiflexible polymers with persistence length 2 and 120, we found, respectively, $B_2/L^2 = 0.2393 \pm 0.0003$ and 0.3166 ± 0.0002. The latter value approaches the value
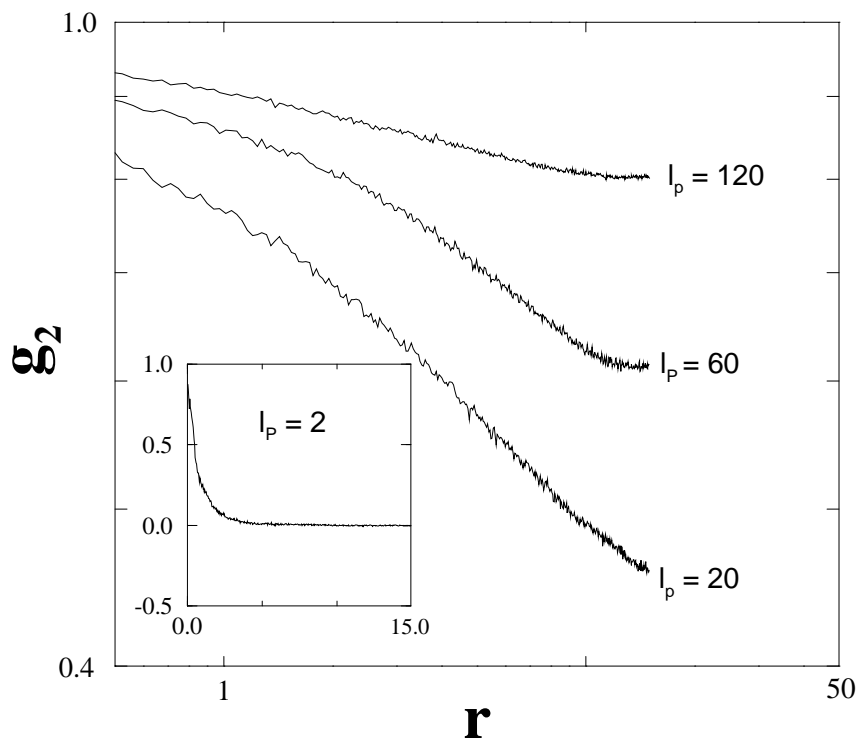
FIGURE 4.4 The orientational pair distributution function $g_2(r) = \langle \cos\{2[\theta(0) - \theta(r)]\} \rangle$ versus r (in units of the segment length) for different values for the flexibility of the two-dimensional semiflexible polymers.

for the second virial coefficient for hard needles, i.e., $1/\pi$. As can be seen in Fig. 4.2, the pressure computed in our MC simulations reduces to the value predicted on the basis of the second-virial coefficient, in the low-density limit.

In order to test our calculations of the pressure by virtual volume changes, we also computed the pressure by integrating the Gibbs-Duhem equation. Fig. 4.3 shows that the pressure calculations by virtual volume changes agree well with the pressure obtained by integration of the Gibbs-Duhem equation.

The orientational pair distribution function $g_2(r) = \langle \cos\{2[\theta(0) - \theta(r)]\} \rangle$ is plotted in Fig. 4.4 as a function of r (in units of the segment length) for a system with a density ρL^2 of about 8. For large flexibility ($l_P=2$), the orientational order dies out over a distance smaller than the length of the polymer. For stiffer chains, we find that the orientational order appears to decay algebraically. This algebraic decay of orientational order was also observed in a two-dimensional fluid of hard needles, which shows an isotropic-nematic phase transition of the Kosterlitz-Thouless type. For 2D nematics this Kosterlitz-Thouless transition occurs at a universal value of the renormalised elastic

constant $K = (K_3 K_1)^{1/2}$, where K_1 and K_3 are the elastic constants for the splay and bend, respectively. This universal value is denoted by $K_{\mathbf{K-T}}$ and is given by [86]:

$$\beta K_{\mathbf{K-T}} = \frac{8}{\pi} \tag{4.12}$$

Using Eq. 4.10, we computed the elastic constants for the bend and the splay as function of the density. The results are plotted in Figs. 4.5 and 4.6. We observe that the elastic constants increase with stiffness and density. This effect is to be expected, as a system with only a few flexible chains is easier to deform, than a system consisting of many rigid chains. We also find that the elastic constants for the splay are smaller than for the bend. Using Eq. 4.12, we can now estimate the density at which a Kosterlitz-Thouless transition should occur. To this end, we fitted our data for the elastic constants as a function of the density for different persistence lengths. Using this fit, we determined the density $\rho_{\mathbf{K-T}}$, where $K = K_{\mathbf{K-T}}$ for a given persistence length. We find $\rho_{\mathbf{K-T}} L^2$ = 21.7 $\pm$ 0.8, 16.1 $\pm$ 0.5, 11.7 $\pm$ 0.5 for persistence length l_P = 20, 60, and 120, respectively (see Fig. 4.7).

In Fig. 4.8, we have shown typical configurations of the two-dimensional semiflexible polymer fluid with persistence length l_P = 120 at densities ρL^2 = 4.89, 9.11, and 22.22 and with persistence length l_P =20 at densities ρL^2 = 4.44, 8.88, and 22.22. The snapshots for the highest density are well inside the nematic regime. The configurations at lower densities are isotropic, in spite of the fact that, due to finite size effects, the configurations look nematic. In Fig. 4.9, we have shown typical snapshots of the semiflexible polymer fluid with persistence length l_P = 2 at densities ρL^2 = 5.11 and 8.44. Both configurations are in the isotropic regime.

In the nematic phase, each polymer is strongly hindered by neighbouring polymers and we can assume that each polymer is effectively confined to a tube with diameter D. The tube diameter D scales with the density as ρ^{-1}. The ratio of the elastic constants for the bend and for the splay is then expected to scale as follows [87]

$$\frac{K_3}{K_1} \sim \left(\frac{\lambda}{D}\right)^2 \tag{4.13}$$

A new length scale is introduced here, namely the deflection length λ. The deflection length is the characteristic length scale for a semiflexible chain confined in a tube with diameter D. This length scale corresponds to the average distance between two successive deflection points of the chain in the tube and is found to scale as $\lambda \sim l_P^{1/3} D^{2/3}$ (see Eq. 3.3). It is not surprising that the ratio of the elastic constants follows Eq. 4.13, as the deflection length and the diameter are the characteristic length scales parallel and
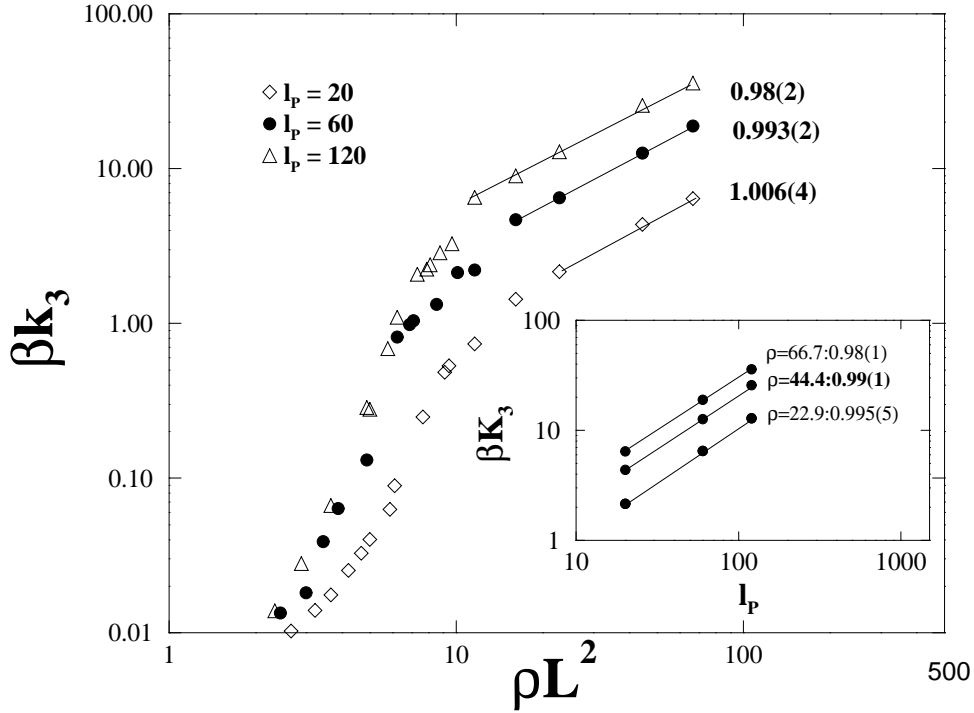
FIGURE 4.5   The elastic constant for the bend as a function of the density and the persistence length (the inset). In order to investigate the scaling behaviour, we have fitted the data for high density. The values for the slopes are plotted with the error in the last digit between brackets.

perpendicular to the nematic director. The bending elastic constant is directly related to the internal bending constant and the density and scales as [87]

$$K_3 \sim C\rho = \rho k_B T l_P \tag{4.14}$$

Using Eqs. 4.13 and 4.14 we can derive the scaling behaviour of the elastic constant for the splay with the density and the persistence length

$$K_1 \sim \rho^{1/3} l_P^{1/3} \tag{4.15}$$

It is, therefore, interesting to investigate the scaling behaviour of the elastic constants at high densities by simulation. We find that both the bending elastic constant and the splay elastic constant scale as a power of the density ($K_1 \sim \rho^{\mu_1}$ and $K_3 \sim \rho^{\mu_3}$). We computed μ_1 and μ_3 for the different persistence lengths as shown in Figs. 4.5 and 4.6. We find μ_3
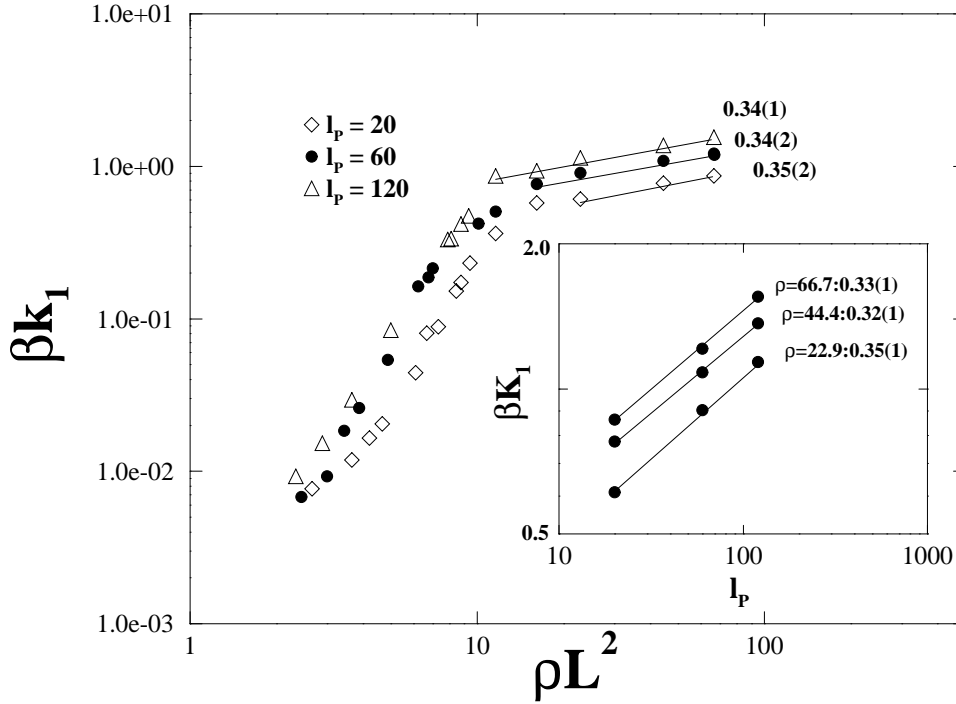
FIGURE 4.6   The elastic constant for the splay as a function of the density and the persistence length (the inset). In order to investigate the scaling behaviour, we have fitted the data for high density. The values for the slopes are plotted with the error in the last digit between brackets.

$= 1.006 \pm 0.004$, 0.993 ± 0.002, and 0.98 ± 0.02 for, respectively, persistence lengths $l_P = 20,\ 60$, and 120. Thus we do indeed find that the bending elastic constant scales linearly with the density for densities well inside the nematic regime. In Fig. 4.6, μ_1 is 0.35 ± 0.02, 0.34 ± 0.02, and 0.34 ± 0.01 for, respectively, persistence lengths $l_P = 20,\ 60$, and 120. This value should be compared with $1/3$ as expected on the basis of the scaling argument. Secondly, the bending elastic constant is found to scale as $\sim l_P^{\nu_3}$ and the splay elastic constant scales as $\sim l_P^{\nu_1}$. We computed ν_1 and ν_3 for the different densities as shown in the insets of Figs. 4.5 and 4.6. We find, respectively, $\nu_3 = 0.995 \pm 0.005$, 0.99 ± 0.01, and 0.98 ± 0.01 for densities $\rho L^2 = 22.9,\ 44.4$, and 66.7. For ν_1, we find $\nu_1 = 0.35 \pm 0.01$, 0.32 ± 0.01 and 0.33 ± 0.01 for densities $\rho L^2 = 22.9,\ 44.4$ and 66.7, respectively. This should be compared with the values $\nu_3 = 1$ and $\nu_1 = 1/3$ predicted by theory. Thus our data are consistent with the scaling relations predicted theoretically.

In summary, we have performed simulations of a two-dimensional system of semi-
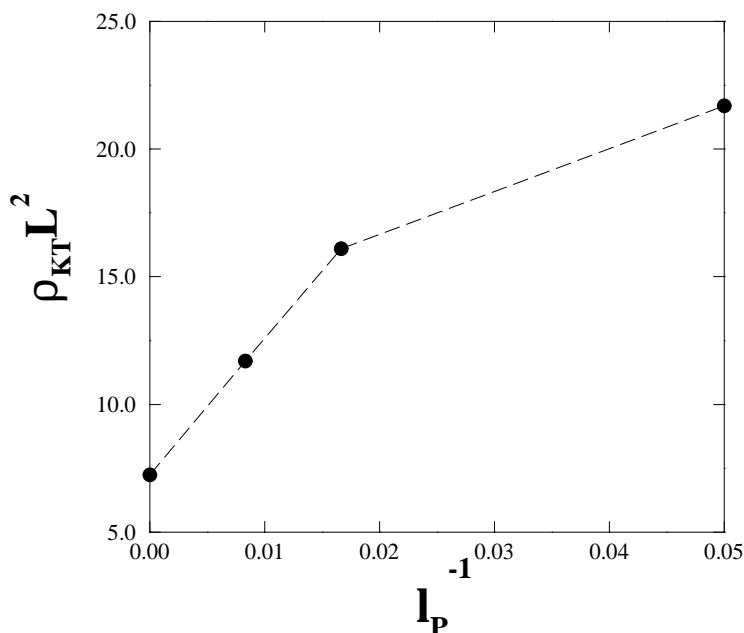
FIGURE 4.7 The density at which the Kosterlitz-Thouless transition occurs versus the inverse persistence length flexibility for a two-dimensional system of semiflexible polymers with L the length of the polymers. The value for $l_P^{-1}{=}0$ is taken from Ref. [79]

flexible polymers. For a dilute system the pressure decreases when the polymers become more flexible, but increases in dense systems. If we increase the density, we observe an isotropic-nematic phase transition with algebraic decay of orientational order. This transition appears to be of the Kosterlitz-Thouless type. The scaling behaviour of the elastic constants is found to be in good agreement with the theoretical predictions.

Appendix

One of the trial moves in a GCMC simulation is the exchange of particles with an infinitely large reservoir, which contains an ideal gas of the same particles. In the present case, the ideal gas particles have internal bending energy. Direct insertion of all but the shortest flexible particles in a dense fluid has a prohibitively low probability, as it almost always results in an overlap with one of the other chains. We therefore employed an extension of the configurational-bias Monte Carlo method [80] to GCMC simulations. In this algorithm, we bias the insertion of the chains in such a way that the 'holes' of the system are found. Below, we describe the algorithm.

Consider a trial move to insert a molecule in the system. We first choose a random
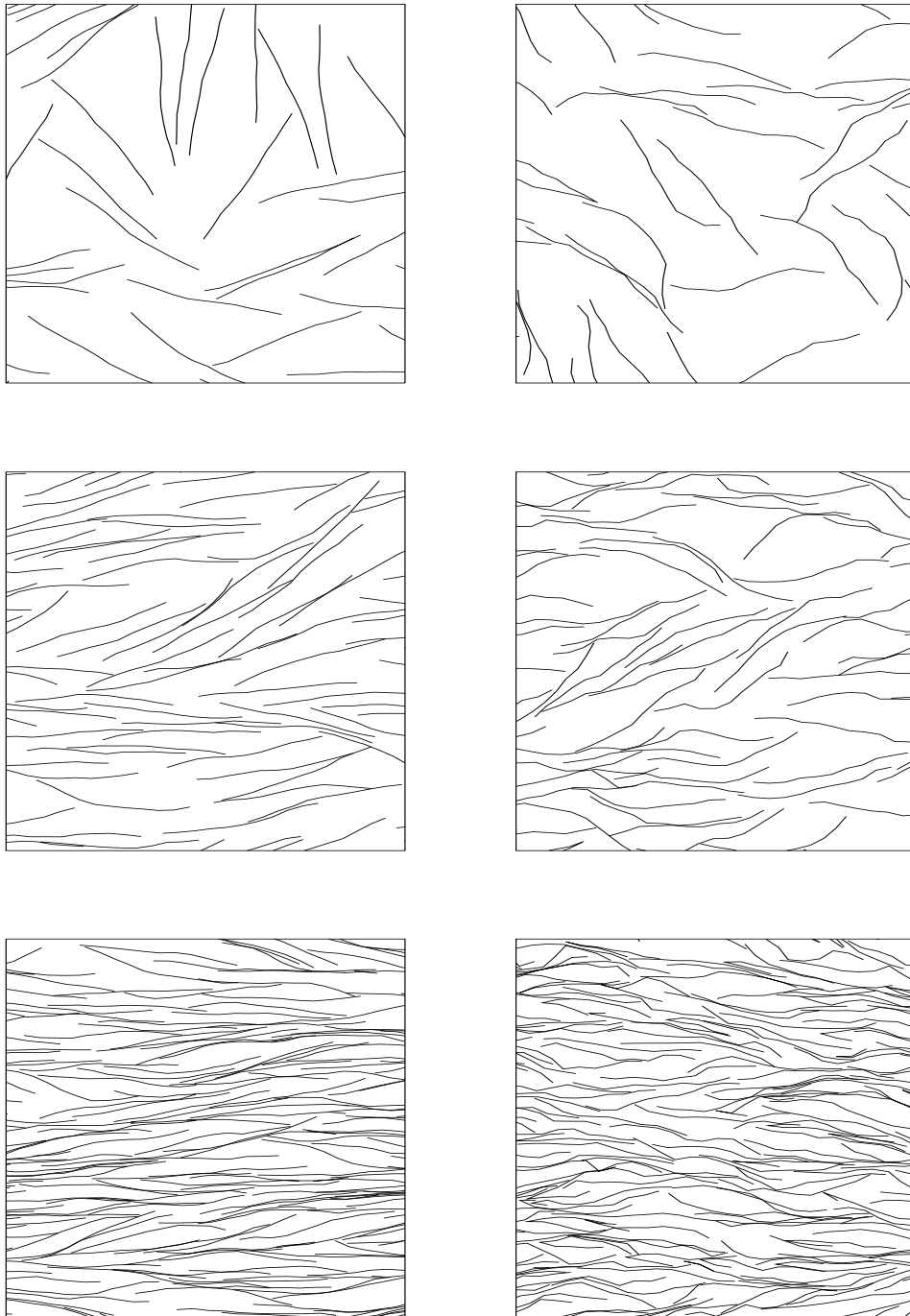
FIGURE 4.8   Snapshots of the two-dimensional semiflexible polymers with persistence length $l_P = 120$ (left, ρL^2 equal to 4.89, 9.11, and 22.22 from top to bottom) and $l_P = 20$ (right, ρL^2 equal to 4.44, 8.88, and 22.22 from top to bottom). The size of the snapshots is 25×25 in units of the segment length.
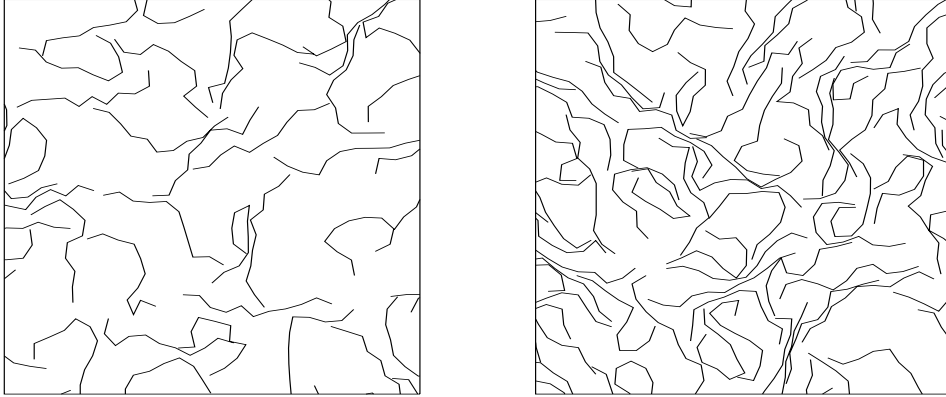
FIGURE 4.9   Snapshots of the two-dimensional semiflexible polymers with persistence length $l_P = 2$ ($\rho L^2 = 5.11$ and 8.44 from left to right). The size of the snapshots is 25 x 25 in units of the segment length.

position and a random orientation. The construction of the chain proceeds then segment by segment. Let us consider the addition of one such segment. To be specific, let us assume that we have already grown $i-1$ segments, and that we are trying to add segment i. This is done as follows

1. Generate a fixed number, say k, trial segments. The probability distribution of the orientations of the trial segments is proportional to the internal Boltzmann weight $P^{\mathrm{id}}_{\hat{\mathbf{w}}_{i-1}\hat{\mathbf{w}}_j} = \exp(-\beta u^{\mathrm{id}}_{\hat{\mathbf{w}}_{i-1}\hat{\mathbf{w}}_j})$ associated with the internal bending. We denote the different trial segments by indices $1,2,\ldots,k$. Now the probability to generate a given subset $\{\hat{\mathbf{w}}\}_i$ of k trial segments with orientations $\hat{\mathbf{w}}_1$ through $\hat{\mathbf{w}}_k$ is equal to

$$P_{\{\hat{\mathbf{w}}\}_i} = \frac{1}{B^k} \prod_{j=1}^{k} d\hat{\mathbf{w}}_j \, P^{\mathrm{id}}_{\hat{\mathbf{w}}_{i-1}\hat{\mathbf{w}}_j} \tag{4.16}$$

where the normalisation constant B is equal to $\int d\hat{\mathbf{w}}_j \, \exp(-\beta u^{\mathrm{id}}_{\hat{\mathbf{w}}_{i-1}\hat{\mathbf{w}}_j})$

2. For all k trial segments, the 'external' Boltzmann factor $\exp(-\beta u^{\mathrm{ext}}_{\hat{\mathbf{w}}_j})$ is computed, where $u^{\mathrm{ext}}_{\hat{\mathbf{w}}_j}$ is the potential energy of the j th trial segment of the polymer with conformation $\Gamma_{\mathbf{w}}$ due to interaction with all the other segments in the system.

3. Select one of the trial segments, say $\hat{w}_i$, with a probability

$$P_{\hat{w}_i}^{\mathrm{ext}} = \frac{\exp\left(-\beta u_{\hat{w}_i}^{\mathrm{ext}}\right)}{Z_{\{\hat{w}\}_i}} \tag{4.17}$$

where we have defined

$$Z_{\{\hat{w}\}_i} \equiv \sum_{j=1}^{k} \exp(-\beta u_{\hat{w}_j}^{\mathrm{ext}}) $$

The subscript $\{\hat{w}\}_i$ means that $\hat{w}_i$ is one of the segments of the subset, so $\hat{w}_i \in \{\hat{w}\}_i$.

4. Add this segment as segment i to the chain and store the corresponding partial "Rosenbluth weight" [80]:

$$\omega_i = Z_{\{\hat{w}\}_i}/k \tag{4.18}$$

In order to use this method to transfer a molecule from the reservoir to the system with N molecules in a GCMC simulation, we impose detailed balance on the Monte Carlo scheme. This implies that in equilibrium, the rate at which particles are removed from the system equals the reverse rate.

Let us first consider the grand canonical partition function in scaled coordinates of a combined system of N interacting particles in volume V and $M - N$ ideal polymers in a reservoir of volume V_{res}:

$$\begin{aligned}
Q(M, V, V_{\mathrm{res}}, T) = \sum_{N=0}^{M} &\frac{V^N V_{\mathrm{res}}^{M-N}}{\Lambda^{3M} N!(M-N)!} \\
\times &\int ds^{M-N} \int d\Gamma^{M-N} \exp[-\beta V^{\mathrm{id}}(\Gamma^{M-N})] \\
\times &\int ds^N \int d\Gamma^N \exp[-\beta(U^{\mathrm{id}}(\Gamma^N) + U^{\mathrm{ext}}(s^N))]
\end{aligned} \tag{4.19}$$

where $\Lambda = \sqrt{h^2/2\pi m k_B T}$, $U^{\mathrm{ext}}(s^N)$ is the external potential of the N particles interacting with each other by a hard-core potential. $U^{\mathrm{id}}(\Gamma^N)$ and $V^{\mathrm{id}}(\Gamma^{M-N})$ are the internal potentials corresponding to the internal bending energy of the, respectively, N flexible chains in the system and $M - N$ flexible chains in the reservoir. The probability density $P(s^M; N)$ to find a system with $M - N$ particles at reduced coordinates s^{M-N}

in a reservoir of volume V_{res} and N particles at reduced coordinates s^N in a system of volume V is

$$
\begin{aligned}
P(s^M; N) &= \frac{V^N V_{\mathrm{res}}^{M-N}}{N!(M-N)!\Lambda^{3M}} \frac{\exp[-\beta V^{\mathrm{id}}(\Gamma^{M-N})]}{Q(M, V, V_{\mathrm{res}}, T)} \\
&\quad \times \exp\{-\beta[U^{\mathrm{id}}(\Gamma^N) + U^{\mathrm{ext}}(s^N)]\}
\end{aligned} \tag{4.20}
$$

The ratio of the statistical weights $P(s^M; N+1)$ and $P(s^M; N)$ is given by

$$
\frac{P(s^M; N+1)}{P(s^M; N)} = \frac{V(M-N)\exp[-\beta(\sum_{i=1}^{L} u^{\mathrm{id}}_{\hat{\mathbf{w}}_{i-1}\hat{\mathbf{w}}_i} + u^{\mathrm{ext}}_{\hat{\mathbf{w}}_i})]}{V_{\mathrm{res}}(N+1)\exp[-\beta \sum_{i=1}^{L} v^{\mathrm{id}}_{\hat{\mathbf{w}}_{i-1}\hat{\mathbf{w}}_i}]} \tag{4.21}
$$

where we have rewritten the difference in internal and external potential as follows

$$
U^{\mathrm{id}}(\Gamma^{N+1}) - U^{\mathrm{id}}(\Gamma^N) + U^{\mathrm{ext}}(s^{N+1}) - U^{\mathrm{ext}}(s^N) = \sum_{i=1}^{L} u^{\mathrm{id}}_{\hat{\mathbf{w}}_{i-1}\hat{\mathbf{w}}_i} + u^{\mathrm{ext}}_{\hat{\mathbf{w}}_i}
$$

$$
V^{\mathrm{id}}(\Gamma^{M-N}) - V^{\mathrm{id}}(\Gamma^{M-N-1}) = \sum_{i=1}^{L} v^{\mathrm{id}}_{\hat{\mathbf{w}}_{i-1}\hat{\mathbf{w}}_i}
$$

The condition for detailed balance can now be expressed as follows

$$
\begin{aligned}
P(s^M; N)\, G(N \mid N+1)\, \mathrm{acc}\,(N \mid N+1) = \\
P(s^M; N+1)\, G(N+1 \mid N)\, \mathrm{acc}\,(N+1 \mid N) \quad (4.22)
\end{aligned}
$$

where $P(s^M; N)$ and $P(s^M; N+1)$ are, respectively, the statistical weights that the system has N particles and $N+1$ particles. $G(N \mid N+1)$ is the probability that, starting from the current configuration of N particles in the system, a configuration is generated with $N+1$ molecules in the system. $\mathrm{acc}\,(N \mid N+1)$ denotes the probability that this trial move is accepted. If we now impose the "superdetailed" balance condition, we have to consider the probability of generating a new chain in the system via one particular choice of trial directions $\{\hat{\mathbf{w}}_{\mathrm{syst}}\}_i$ and of choosing a set of trial directions in the reservoir $\{\hat{\mathbf{w}}_{\mathrm{res}}\}_i$ from all possible sets that contain the old configuration. The probability of transferring a chain of L segments from the reservoir to the system via the set $\{\hat{\mathbf{w}}_{\mathrm{syst}}\}_i$ and of choosing the set $\{\hat{\mathbf{w}}_{\mathrm{res}}\}_i$ will now be equal to the probability to generate the old set of trial directions $\{\hat{\mathbf{w}}_{\mathrm{res}}\}_i$ excluding the old orientation denoted by $P_{\{\hat{\mathbf{w}}_{\mathrm{res}}\}_i} / \exp(-\beta v^{\mathrm{id}}_{\hat{\mathbf{w}}_{i-1}\hat{\mathbf{w}}_i})$ times the probability to generate a new set of trial directions in the system $\{\hat{\mathbf{w}}_{\mathrm{syst}}\}_i$ that contains the new orientation, i.e., $P_{\{\hat{\mathbf{w}}_{\mathrm{syst}}\}_i}$, times the probability to select this new orientation, i.e., $\exp(-\beta u^{\mathrm{ext}}_i)/Z_{\{\hat{\mathbf{w}}\}_i}$

$$
G(N \mid N+1) = \prod_{i=1}^{L} \frac{P_{\{\hat{\mathbf{w}}_{\mathrm{syst}}\}_i} P_{\{\hat{\mathbf{w}}_{\mathrm{res}}\}_i}}{\exp(-\beta v^{\mathrm{id}}_{\hat{\mathbf{w}}_{i-1}\hat{\mathbf{w}}_i})} \frac{\exp(-\beta u^{\mathrm{ext}}_i)}{Z_{\{\hat{\mathbf{w}}\}_i}} \tag{4.23}
$$

The probability $G(N + 1 \mid N)$ is the probability of moving one chain from the system to the reservoir. The probability to exchange one particle with the reservoir is equal to the probability to generate the old set of trial directions in the system $\{\hat{w}_{syst}\}_i$ excluding the old orientation, i.e., $P_{\{\hat{w}_{syst}\}_i} / \exp(-\beta u^{id}_{\hat{w}_{i-1}\hat{w}_i})$, times the probability to generate a new set of trial directions $\{\hat{w}_{res}\}_i$ that contains the new orientation, i.e., $P_{\{\hat{w}_{res}\}_i}$, times the probability to select this new orientation, i.e., $1/k$:

$$G(N + 1 \mid N) = \prod_{i=1}^{L} \frac{P_{\{\hat{w}_{res}\}_i} P_{\{\hat{w}_{syst}\}_i}}{\exp(-\beta u^{id}_{\hat{w}_{i-1}\hat{w}_i})} \frac{1}{k} \tag{4.24}$$

The ratio of the probabilities $G(N + 1 \mid N)$ and $G(N \mid N + 1)$ is now given by

$$\frac{G(N + 1 \mid N)}{G(N \mid N + 1)} = \prod_{i=1}^{L} \frac{\exp(-\beta v^{id}_{\hat{w}_{i-1}\hat{w}_i})}{\exp[-\beta(u^{id}_{\hat{w}_{i-1}\hat{w}_i} + u^{ext}_{\hat{w}_i})]} \frac{Z_{\{\hat{w}\}_i}}{k} \tag{4.25}$$

Substitution of Eqs. 4.21 and 4.25 in Eq. 4.22 yields

$$\begin{aligned}
\text{acc}\,(N \mid N + 1) &= \min\left(1, \frac{P(s^M; N + 1)G(N + 1 \mid N)}{P(s^M; N)G(N \mid N + 1)}\right) \\
&= \min\left(1, \frac{V(M - N)W}{V_{res}(N + 1)}\right) \tag{4.26}
\end{aligned}$$

where $W = \prod_{i=1}^{L} \omega_i$. Let us now consider the limit that the reservoir is very much larger than the interacting system: $M \to \infty$, $V_{res} \to \infty$ and $M/V_{res} \to \rho$. For an ideal gas the fugacity z is equal to the particle density. Therefore, in the limit $M/N \to \infty$, Eq. 4.26 becomes

$$\text{acc}\,(N \mid N + 1) = \min\left(1, \frac{VzW}{N + 1}\right) \tag{4.27}$$

Similarly, we can derive the probability of accepting a trial move that removes a particle from the system to the reservoir:

$$\text{acc}\,(N + 1 \mid N) = \min\left(1, \frac{N + 1}{VzW}\right) \tag{4.28}$$

5

A THREE-DIMENSIONAL SYSTEM OF SEMIFLEXIBLE POLYMERS

In this chapter, we investigate the isotropic-nematic phase transition in a three-dimensional system of semiflexible polymers. The results of our computer simulations are compared with the theoretical predictions.

5.1 Introduction

All existing theories for the phase behaviour of off-lattice semiflexible polymers predict a first order isotropic to nematic phase transition in three dimensions. These theoretical predictions for the phase behaviour of off-lattice semiflexible polymers will be reviewed in Sec. 5.2. The phase diagrams based on these different theoretical approaches differ significantly. It is therefore interesting to explore whether computer simulations can shed some light on this matter. In the previous chapter, we mentioned that long-range orientational order has thus far not been observed in computer simulations of two- and three-dimensional athermal *lattice* polymers. The reason why these polymers do not exhibit long-range orientational order may be related to the fact that the simulations were performed on a lattice. Recently, simulations of an off-lattice system of semiflexible chain molecules consisting of linked hard spheres showed the presence of three fluid phases, which were identified as isotropic, nematic and smectic-A [88].

In this chapter, we describe Monte Carlo simulations of a three-dimensional system of semiflexible polymers consisting of hard spherocylinders connected by joints of variable flexibility. In particular, we investigate the influence of flexibility on the isotropic-nematic phase transition. The simulation method is explained in Sec. 5.3 and

the results of the simulations are reported in Sec. 5.4.

5.2 Theories of the Isotropic-Nematic Transition of Semi-flexible Chains

As a starting point, we first consider the theoretical prediction of the coexistence densities of the isotropic and nematic phases in two extreme cases, namely for rods ($l_P \gg L \gg D$) and for semiflexible polymers ($L \gg l_P \gg D$). Next, we describe how to interpolate this result to arrive at a prediction of the coexistence densities for polymers with arbitrary flexibility.

In Sec. 2.2, we derived an expression for the Helmholtz free energy of a fluid of hard rods in the Onsager approximation, which holds for $L \gg D$:

$$
\begin{aligned}
\frac{\Delta F}{N k_B T} &= \log(\Lambda^3 \rho) - 1 + \int f(\Omega) \log(4\pi f(\Omega)) d\Omega \\
&\quad + \rho L^2 D \int f(\Omega) f(\Omega') |\sin\gamma| d\Omega d\Omega'
\end{aligned}
\tag{5.1}
$$

For a given density ρ this expression must be minimised with respect to the orientational distribution function $f(\Omega)$. At low densities, the only possible solution to the minimum condition is $f(\Omega) = f_{\mathrm{iso}}(\Omega) = 1/4\pi$, representing the isotropic phase. In that case, the contribution to the free energy due to the orientational entropy $\int f_{\mathrm{iso}}(\Omega) \log(4\pi f_{\mathrm{iso}}(\Omega)) d\Omega$ vanishes. The contribution due to the translational entropy becomes $\rho L^2 D \int f_{\mathrm{iso}}(\Omega) f_{\mathrm{iso}}(\Omega') |\sin\gamma| d\Omega d\Omega' = \rho \pi D L^2/4$. At sufficiently high densities, a second solution of the minimum condition is possible, representing the nematic phase, with $f(\Omega) = f_{\mathrm{nem}}(\Omega)$. The exact functional form of $f_{\mathrm{nem}}(\Omega)$ is unknown, but several approximations, that will be discussed below, have been reported in the literature. Because of the first order character of the isotropic-nematic transition, there is a density regime, where an isotropic phase of density ρ_{iso} coexists with a nematic phase of density ρ_{nem} and orientational distribution function $f_{\mathrm{nem}}(\Omega)$. The coexisting phases must be in thermal, mechanical and chemical equilibrium, so that the temperature T, the osmotic pressure Π and the chemical potential μ are the same in both phases:

$$
\begin{aligned}
T_{\mathrm{iso}} &= T_{\mathrm{nem}} \\
\Pi_{\mathrm{iso}}(\rho_{\mathrm{iso}}) &= \Pi_{\mathrm{nem}}(\rho_{\mathrm{nem}}) \\
\mu_{\mathrm{iso}}(\rho_{\mathrm{iso}}) &= \mu_{\mathrm{nem}}(\rho_{\mathrm{nem}})
\end{aligned}
\tag{5.2}
$$

The osmotic pressure and chemical potential are easily obtained by the thermodynamic relations

$$\Pi(\rho) = -\left(\frac{\partial \Delta F}{\partial V}\right)_{N,T} \tag{5.3}$$

$$\mu(\rho) = \left(\frac{\partial \Delta F}{\partial N}\right)_{V,T} \tag{5.4}$$

Note that $\mu_{\mathrm{nem}}(\rho_{\mathrm{nem}})$ and $\Pi_{\mathrm{nem}}(\rho_{\mathrm{nem}})$ depend functionally on $f_{\mathrm{nem}}(\Omega)$. The conditions in Eq. 5.2 and the extremum condition of the Helmholtz free energy are sufficient to determine (numerically) the values for ρ_{iso}, ρ_{nem} and $f_{\mathrm{nem}}(\Omega)$. One way of doing this is to approximate $f_{\mathrm{nem}}(\Omega)$ with a trial function of one or more variational parameters. A well-known trial function is the Gaussian distribution (Eq. 2.23), where α is the variational parameter. Introducing the reduced density $c \equiv \rho v_0 L/D = \phi L/D$, where ϕ is the volume fraction of the rods and v_0 the volume of one rod, the Gaussian approximation leads to [51]

$$c_{\mathrm{iso}} = 3.45 \qquad c_{\mathrm{nem}} = 5.12 \qquad \alpha = 33.4 \tag{5.5}$$

However, if we use instead of the Gaussian trial function Onsager's trial function Eq. 2.22, we obtain the following results [21]

$$c_{\mathrm{iso}} = 3.340 \qquad c_{\mathrm{nem}} = 4.486 \qquad \alpha = 18.58 \tag{5.6}$$

Hence, the results of the coexisting concentrations depend on the form chosen for the trial function.

Although Eq. 5.2 cannot be solved analytically, it is possible to find the exact solution numerically. This approach was pioneered by Lasher [89] and subsequently refined by Kayser and Raveché [90] and by Lekkerkerker *et al.* [91]. Using this method, Lekkerkerker *et al.* obtained the following result [91]

$$c_{\mathrm{iso}} = 3.290 \qquad c_{\mathrm{nem}} = 4.191 \tag{5.7}$$

The difference between this 'exact' result and the approximate answers given by Eq. 5.5 and 5.6 is due to the choice of the approximate trial functions. The Onsager trial function and the Gaussian trial function are too sharply peaked functions and consequently, the contribution to the free energy due to the orientational entropy is overestimated and that due to the translational entropy is underestimated. The result is that the tendency to form the nematic phase is postponed to higher concentrations in the case of these trial functions.

In chapter 2, we also derived an expression for the Helmholtz free energy for semiflexible polymers, i.e., chains that are locally very stiff, but are so long that they form coils:

$$\frac{\Delta F}{N k_B T} = \log(\Lambda^3 \rho) - 1 + \sigma(f) + B_2 \rho \tag{5.8}$$

where

$$\sigma(f) = -\frac{L}{2l_P} \int f^{1/2}(\Omega) \Delta f^{1/2}(\Omega) d\Omega$$

$$B_2 = L^2 D \int f(\Omega) f(\Omega') |\sin\gamma| d\Omega d\Omega' \qquad (5.9)$$

with $f(\Omega)$ the segment orientation distribution function. Again, in the isotropic phase the orientational entropy $\sigma(f)$ is zero and the contribution to the free energy due to the translational entropy is given by $B_2 \rho$ equals $\rho \pi D L^2/4$. If we now use again a Gaussian trial function for the orientational distribution function for the segments, we can calculate similarly as described above the coexisting concentrations in reduced units ($c^* \equiv \phi\, l_P/D$) [41].

$$c_{\text{iso}}^* = 7.77 \qquad\qquad c_{\text{nem}}^* = 9.71 \qquad\qquad \alpha = 12.34 \qquad (5.10)$$

The Onsager trial function gives the following results [51]

$$c_{\text{iso}}^* = 5.409 \qquad\qquad c_{\text{nem}}^* = 6.197 \qquad\qquad \alpha = 6.502 \qquad (5.11)$$

Using the equivalent of the iterative procedure, we find [92]

$$c_{\text{iso}}^* = 5.124 \qquad\qquad c_{\text{nem}}^* = 5.509 \qquad (5.12)$$

Thus far we only discussed the coexisting concentrations for two extreme cases, namely the rigid rod limit and the very long coil limit. However, we are interested in the range between these two limits. In chapter 2, we already mentioned that several approaches have been made to predict the phase behaviour of semiflexible polymers of intermediate chain lengths ($L \simeq l_P \gg D$). Khokhlov and Semenov calculated therefore the correction terms to these limits for the orientational free energy $\sigma(f)$ [43].
For $L \ll l_P$:

$$\sigma(f) = \sigma_{\text{rigid}}^{(0)}(f) + \sigma_{\text{rigid}}^{(1)}(f)$$

$$= \int f(\Omega) \log(4\pi f(\Omega)) d\Omega + \frac{L}{12 l_P} \int d\Omega [\nabla f(\Omega)]^2/f(\Omega) \quad (5.13)$$

and for $L \gg l_P$:

$$\sigma(f) = \frac{L}{l_P}\sigma_{\text{worm}}^{(0)}(f) + \sigma_{\text{worm}}^{(1)}(f)$$

$$= \frac{L}{8 l_P} \int d\Omega [\nabla f(\Omega)]^2/f(\Omega) - 2\log \int f(\Omega)^{1/2} d\Omega \qquad (5.14)$$

These expressions can be worked out further for the specific choice of the Onsager trial function [51]

$$\sigma(\alpha) = \frac{L(\alpha - 1)}{4l_P} + \log(\frac{1}{4\alpha}) \quad (L \gg l_P) \tag{5.15}$$

$$\sigma(\alpha) = \log \alpha - 1 + \frac{L(\alpha - 1)}{6l_P} \quad (L \ll l_P) \tag{5.16}$$

The coexisting concentrations become now [51]

$$c^*_{\text{iso}} = 5.409 + 1.910 N_{l_P}^{-1} \quad c^*_{\text{nem}} = 6.197 + 1.781 N_{l_P}^{-1} \quad (N_{l_P} \gg 1) \tag{5.17}$$

$$c^*_{\text{iso}} = 3.340 N_{l_P}^{-1} + 4.99 \quad c^*_{\text{nem}} = 4.486 N_{l_P}^{-1} - 1.458 \quad (N_{l_P} \ll 1) \tag{5.18}$$

where $N_{l_P} \equiv L/l_P$. In order to obtain a formula valid for arbitrary L/l_P these results can be interpolated in the form of a Padé approximant [43, 51]

$$\begin{aligned} c^*_{\text{iso}} &= \frac{3.34 + 5.97 N_{l_P} + 1.585 N_{l_P}^2}{N_{l_P}(1 + 0.293 N_{l_P})} \\ c^*_{\text{nem}} &= \frac{4.486 + 11.24 N_{l_P} + 17.54 N_{l_P}^2}{N_{l_P}(1 + 2.83 N_{l_P})} \end{aligned} \tag{5.19}$$

Another approach was taken by Odijk. Within the Gaussian approximation, he derived a closed expression for the orientational free energy for arbitrary chain length [51]

$$\sigma(\alpha) \simeq \log \alpha + \frac{\alpha - 1}{6} N_{l_P} + \frac{5}{12} \log \left[\cosh(\frac{\alpha - 1}{5} N_{l_P}) \right] - \frac{19}{12} \log 2 \tag{5.20}$$

In fact, this expression is a highly accurate approximation of the exact expression, which is easier to use in further calculations. The coexisting concentrations calculated from Eq. 5.20 deviate significantly from the concentrations given by Eq. 5.19.

Hentschke proposed a semi-empirical expression for the free energy of semiflexible polymers of arbitrary chain length by extrapolating the orientational free energy in the rod limit and the semiflexible limit [55]:

$$\sigma_h(f) \simeq \frac{\sigma_{\text{rigid}}^{(0)}(f) + \sigma_1(f) N_{l_P} + s(f) \sigma_{\text{worm}}^{(0)}(f) N_{l_P}^2}{1 + s(f) N_{l_P}} \tag{5.21}$$

where

$$\begin{aligned} \sigma_1(f) &= s(f) \sigma_{\text{rigid}}^{(0)}(f) + \sigma_{\text{rigid}}^{(1)}(f) \\ s(f) &= \frac{\sigma_{\text{worm}}^{(0)}(f) - \sigma_{\text{rigid}}^{(1)}(f)}{\sigma_{\text{rigid}}^{(0)}(f) - \sigma_{\text{worm}}^{(1)}(f)} \end{aligned} \tag{5.22}$$

If we now use the Onsager's trial function and retain only the leading order terms, we find

$$\sigma_h(f) \simeq \frac{12(\log 4 - 1)(\log \alpha - 1) + (\log 16\alpha - 3)z + (1/4)z^2}{12(\log 4 - 1) + z} \tag{5.23}$$

where z equals $(\alpha - 1)N_{l_P}$. In addition, Hentschke used a generalisation of the Carnahan-Starling equation for hard spheres to the case of spherocylinders instead of the Onsager or second virial approximation [93]. The Helmholtz free energy expression for semiflexible polymers reads now

$$\begin{aligned}
\frac{\Delta F}{N k_B T} &= \log(\Lambda^3 \rho) - 1 + \sigma_h(f) + A(\phi, x) \\
&\quad + B(\phi, x)\frac{4}{\pi}\int f(\Omega)f(\Omega')|\sin \gamma|d\Omega d\Omega'
\end{aligned} \tag{5.24}$$

where we define $x = L/D$ and

$$\begin{aligned}
A(\phi, x) &= 4\phi\frac{1 - 3\phi/4}{(1 - \phi)^2} \\
B(\phi, x) &= \phi\frac{1 - 3\phi/4}{(1 - \phi)^2}\frac{3x^2/2}{1 + 3x/2}
\end{aligned} \tag{5.25}$$

Using this expression for the Helmholtz free energy and Onsager's trial function, Hentschke computed the phase diagram for persistent flexible hard rods [55, 94]. In Fig. 5.1, we show that the phase diagrams computed numerically on the basis of the several theories differ significantly from each other. A detailed analysis of this isotropic-nematic phase transition is therefore needed.

5.3   Model and Computational Technique

We performed computer simulations of a three-dimensional system of semiflexible polymers consisting of 10 hard spherocylinders connected to each other. The bending energy for a joint between two segments i and $i-1$ is given by (Eq. 3.26)

$$u^{\text{id}}_{\hat{\mathbf{w}}_{i-1}\hat{\mathbf{w}}_i} = \frac{C}{2\ell}\theta^2_{\hat{\mathbf{w}}_{i-1}\hat{\mathbf{w}}_i} \tag{5.26}$$

where $\theta_{\hat{\mathbf{w}}_{i-1}\hat{\mathbf{w}}_i}$ is the angle between the unit vectors $\hat{\mathbf{w}}_{i-1}$ and $\hat{\mathbf{w}}_i$ that specify respectively the orientations of the segments $i-1$ and i. The relation between the persistence length and the bending elastic constant C is given by (Eq. 2.14)

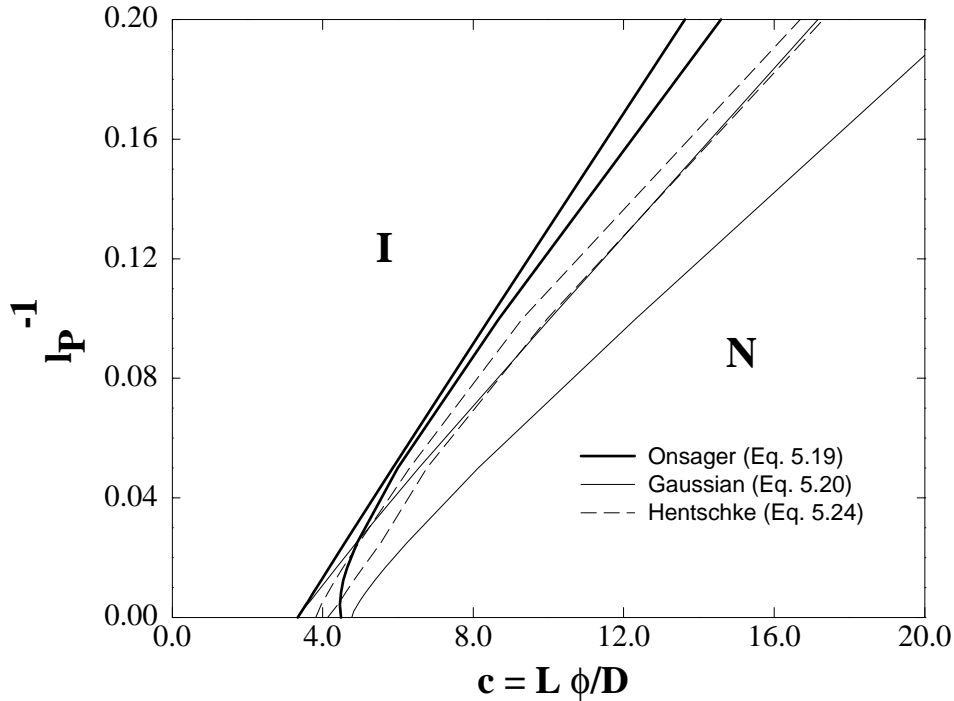$$l_P = \frac{C}{k_B T} \tag{5.27}$$

FIGURE 5.1   The phase diagrams of a three-dimensional system of semiflexible polymers based on some of the theories mentioned in the text.

The ℓ/D ratio of these spherocylinders is 4, where ℓ is the segment length and D the diameter of the spherocylinder. The segment length was chosen as our unit of length. In order to compute the phase diagram, we generalised a scheme introduced by Kofke [95, 96] that enables direct simulation of the phase coexistence line. This method is based on the Gibbs-Duhem equation. For our model of semiflexible polymers the Gibbs-Duhem equation reads

$$N d\mu = V dP + \left(\frac{\partial G}{\partial l_P^{-1}} \right) dl_P^{-1} \tag{5.28}$$

where G is the Gibbs free energy. Using the thermodynamic conditions for coexistence of two phases (Eq. 5.2), we obtain the following relation between the pressure and the persistence length l_P along the $P\text{-}l_P^{-1}$ coexistence line:

$$\left(\frac{\partial P}{\partial l_P^{-1}} \right)_{\text{coex}} = -\frac{\Delta(\partial G/\partial l_P^{-1})}{\Delta V} \tag{5.29}$$

where $\Delta(\partial G/\partial l_P^{-1})$ and ΔV denote the difference of $(\partial G/\partial l_P^{-1})$ and volume V in the coexisting phases, which can be measured easily in the simulations. Using the Kofke

method, we can compute the phase coexistence curve, provided that one set of points on this curve is already known. In the present case, the known point is the limit of infinite persistence length l_P. In this limit, the semiflexible polymers reduce to hard rods. For this fully rigid limit, we performed a Gibbs ensemble Monte Carlo simulation of hard spherocylinders of length $L/D = 40$. The reduced pressure and concentrations ($c \equiv L\phi/D$) of the coexisting isotropic and nematic phase obtained from the simulations are given by

$$
\begin{aligned}
c_{\mathrm{iso}} &= 3.075 \pm 0.015 \\
c_{\mathrm{nem}} &= 4.065 \pm 0.015 \\
\beta v_0 \Pi L/D &= 16.36 \pm 0.88
\end{aligned}
\tag{5.30}
$$

These values should be compared with the values obtained by Lekkerkerker for limit $L/D \to \infty$ (see Eq. 5.7) [91]:

$$
c_{\mathrm{iso}} = 3.290 \qquad c_{\mathrm{nem}} = 4.191 \qquad \beta v_0 \Pi = 14.116 \tag{5.31}
$$

where the pressure of the coexisting phases is obtained by using the relation

$$
\beta v_0 \Pi_{\mathrm{iso}} L/D = c_{\mathrm{iso}} + c_{\mathrm{iso}}^2 \tag{5.32}
$$

Eq. 5.29 was solved using a four-points Adams-Bashforth-Moulton predictor-corrector algorithm (see e.g. Ref. [97]). As such algorithms are not self-starting, we initialise the integration using a first order predictor-corrector algorithm. Starting from $l_P^{-1} = 0$, we increase the flexibility of the polymers and compute for this new flexibility the predicted pressure. Then, we performed constant pressure Monte Carlo simulations [78] at this predicted pressure for each phase and compute $\Delta(\partial G/\partial l_P^{-1})$ and ΔV, i.e., the right-hand side of Eq. 5.29. Using the information of the derivative at this new point obtained from the simulations, we correct the predicted pressure. Repeating these predictor-corrector steps, we performed simulations along the $P - l_P^{-1}$ coexistence lines. After two integration steps, a second order predictor-corrector algorithm was applied. After that, we continued with an integration routine of the fourth order.

In a constant pressure simulation, the number of particles, the pressure and the temperature are fixed quantities. In our simulations, the number of polymers for the isotropic and the nematic phase are, respectively, 268 and 431. In the simulations we had to ensure that no trial move would result in a hard-core overlap of the polymer segments. To test whether a trial move generated such an overlap, we used the overlap criterion for spherocylinders described in Ref. [98]. In the isothermal-isobaric Monte Carlo simulations, the following trial moves were performed:
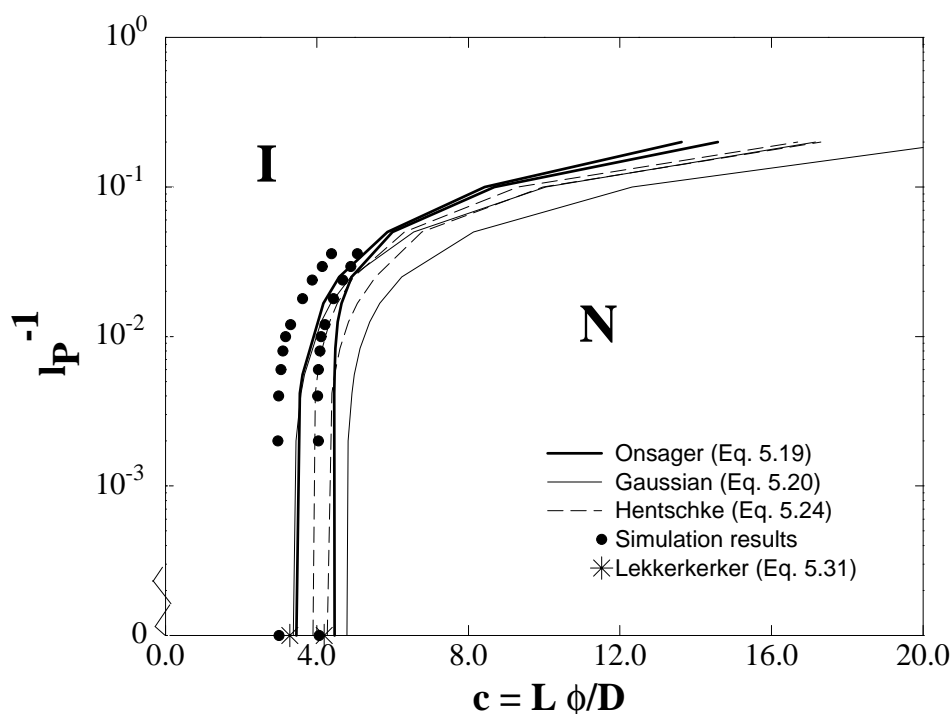
FIGURE 5.2 Phase diagram of a three-dimensional system of semiflexiblle poly-
mers consisting of ten hard spherocylinders connected to each other.

- Reptation

- Regrow a whole polymer at a random position and with a random orientation
  using the configurational-bias Monte Carlo method (CBMC) [80].

- Volume changes

Most runs consisted of at least 10^6 cycles per polymer. Each cycle consists of one
reptation move and an attempt to change the volume of the box. On average once
every five reptation moves a polymer is completely regrown at a random position in the
periodic box using the CBMC method. For more technical details on the regrow of a
polymer, the reader is referred to the Appendix in chapter 3.

5.4 Results and Discussion

Using the Kofke integration scheme, we obtained the isotropic-nematic coexistence
curve of a three-dimensional system of semiflexible polymers consisting of 10 hard
spherocylinders connected to each other. Our results are shown in Fig. 5.2. For the sake
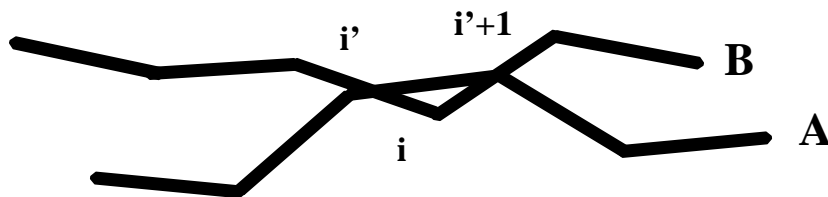of comparison, we also plot the relevant theoretical predictions. We clearly observe that

FIGURE 5.3   Schematic representation of a three segment interaction.

compared with the theories our simulation results for the coexisting densities are shifted systematically to lower densities. In the rest of this section, we discuss possible sources of this discrepancy between theory and computer 'experiment'.

The first possible reason why we find systematically lower values for the coexisting densities in our computer simulations may be related to the choice of the trial function in the theoretical descriptions. In Sec. 5.2, we already mentioned that the trial functions are too sharply peaked and that consequently this method overestimates the coexisting densities. In the case of infinitely stiff polymers (hard spherocylinders), we find that our simulation results agree reasonably well with the predicted coexisting densities calculated self-consistently by Lekkerkerker [91]. In this method, the functional form of the orientational distribution function is not approximated by a trial function.

A second reason why the current theories overestimate the coexisting densities may be related to the approximations made in the calculation of the second virial coefficient of the polymer system. In most theories, the second virial coefficient of a fluid of N polymers consisting of M segments is approximated by the second virial coefficient of a fluid of MN disconnected segments. This treatment consists, in fact, of two simultaneous approximations, since both the effect of connectivity and the three-and-more segment interactions are neglected. One can easily imagine that the combination of these two approximations is serious, since there is an enhanced probability that the ith segment of polymer A overlaps with segment $i'+1$ of polymer B, when segment i of polymer A already overlaps with segment i' of polymer B (see Fig. 5.3). This is caused simply by the fact that segment $i'+1$ is in the direct neighbourhood of i' due to connectivity. The sequel of this section is devoted to a more detailed and quantitative analysis of the approximations made in the calculation of the second virial coefficient of semiflexible polymers.

The second virial term for a mixture of particles is given in Eq. 2.7. We can now identify the mole fractions x_i with the fraction of the molecules that have an orientation within a solid angle $d\Omega$ around Ω at a position $d\mathbf{r}$ around $\mathbf{r}$, i.e., $x_i \leftrightarrow \rho(\mathbf{r}, \Omega)d\mathbf{r}d\Omega$.

The second virial term reads now

$$B_2 = -\frac{1}{2V} \int d\mathbf{r} d\mathbf{r}' d\Omega d\Omega' \rho(\mathbf{r}, \Omega) \rho(\mathbf{r}', \Omega') \Phi_{12}(\mathbf{r}, \Omega; \mathbf{r}', \Omega') \tag{5.33}$$

If we now consider polymers consisting of k segments, the second virial term becomes

$$\begin{aligned}
B_2 &= -\frac{1}{2V^{2k-1}} \int d\{\mathbf{r}\} d\{\mathbf{r}'\} d\{\Omega\} d\{\Omega'\} \rho(\{\mathbf{r}\}, \{\Omega\}) \rho(\{\mathbf{r}'\}, \{\Omega'\}) \\
&\quad \times \Phi_{12}(\{\mathbf{r}\}, \{\Omega\}; \{\mathbf{r}'\}, \{\Omega'\})
\end{aligned} \tag{5.34}$$

Note that the connectivity can be implemented by the segment distribution function $\rho(\{\mathbf{r}\}, \{\Omega\})$, which we will show below. The configurations of the chains are now given by the centres of mass $\{\mathbf{r}\} = (\mathbf{r}_1, \mathbf{r}_2, \ldots, \mathbf{r}_k)$ and the orientations $\{\Omega\} = (\hat{\mathbf{w}}_1, \hat{\mathbf{w}}_2, \ldots, \hat{\mathbf{w}}_k)$ of the individual segments of the polymer. The Mayer function $\Phi_{12}(\{\mathbf{r}\}, \{\Omega\}; \{\mathbf{r}'\}, \{\Omega'\})$ is directly related to the polymer-polymer interaction energy U_{12}, which we assume to be the sum of pairwise additive segment-segment interaction energies u_{12}:

$$\begin{aligned}
\Phi_{12}(\{\mathbf{r}\}, \{\Omega\}; \{\mathbf{r}'\}, \{\Omega'\}) &= \exp[-\beta U_{12}(\{\mathbf{r}\}, \{\Omega\}; \{\mathbf{r}'\}, \{\Omega'\})] - 1 \\
&= \exp[-\beta \sum_{i,i'} u_{12}(\mathbf{r}_i, \hat{\mathbf{w}}_i; \mathbf{r}'_{i'}, \hat{\mathbf{w}}'_{i'})] - 1
\end{aligned} \tag{5.35}$$

Introducing the segment-segment Mayer function:

$$\begin{aligned}
\phi_{12}^{i,i'} &\equiv \phi_{12}(\mathbf{r}_i, \hat{\mathbf{w}}_i; \mathbf{r}'_{i'}, \hat{\mathbf{w}}'_{i'}) \\
&= \exp[-\beta u_{12}(\mathbf{r}_i, \hat{\mathbf{w}}_i; \mathbf{r}'_{i'}, \hat{\mathbf{w}}'_{i'})] - 1
\end{aligned} \tag{5.36}$$

i.e., the interaction of segment i of polymer 1 with segment i' of polymer 2, we can rewrite the Mayer function for polymers as follows

$$\begin{aligned}
\Phi_{12}(\{\mathbf{r}\}, \{\mathbf{r}'\}; \{\Omega\}, \{\Omega'\}) &= \sum_{i,i'} \phi_{12}^{i,i'} + \sum_i \sum_{i' \neq j'} \phi_{12}^{i,i'} \phi_{12}^{i,j'} + \\
&\quad \sum_{i \neq j} \sum_{i'} \phi_{12}^{i,i'} \phi_{12}^{j,i'} + \sum_{i \neq j} \sum_{i' \neq j'} \phi_{12}^{i,i'} \phi_{12}^{j,j'} + \\
&\quad \sum_{i \neq j} \sum_{i' \neq j'} \phi_{12}^{i,i'} \phi_{12}^{i,j'} \phi_{12}^{j,j'} + \\
&\quad \sum_{i \neq j} \sum_{i' \neq j'} \phi_{12}^{i,i'} \phi_{12}^{i,j'} \phi_{12}^{j,i'} \phi_{12}^{j,j'} \\
&\quad + \ldots
\end{aligned} \tag{5.37}$$

It is now convenient to rewrite this expansion in terms of diagrams. Fig. 5.4 shows the diagrammatic expansion of the Mayer function for polymers into Mayer functions
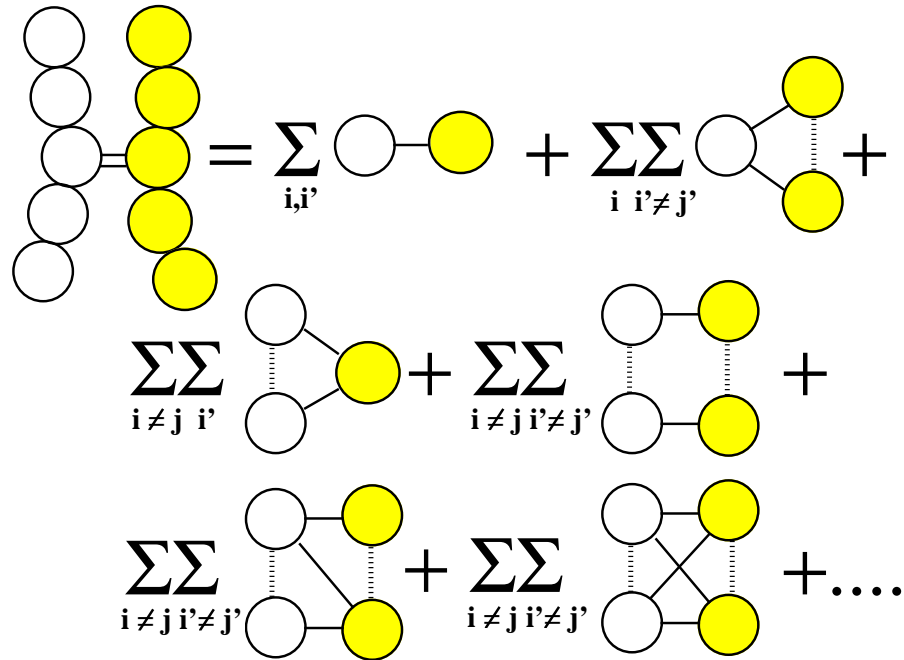
FIGURE 5.4   Diagrammatic expansion of the Mayer function for polymers in Mayer functions for segments. The open circles denote the segments of polymer 1, the shaded circles the segments of polymer 2. The dashed lines denote that the segments interact with each other through the backbone of the polymer. The solid bonds between the circles are associated with the Mayer function for segments and the double bond to the Mayer function for polymers.

for segments. The white and the shaded circles denote the segments of polymer 1 and 2, respectively. The dashed lines between the segment of the same species denote that the segments interact with each other through the backbone of the polymer. The solid bonds corresponds to the Mayer functions for segments and the double bond to the Mayer function for polymers.

As mentioned before, in most theories, the second virial term for a fluid of polymers was estimated to be equal to the second virial term for a fluid, in which the polymers were cut into separated segments. The two simultaneous approximations to calculate Eq. 5.34 can now be identified more precisely. First, the one-polymer distribution function is assumed to be a product of one-segment orientational distribution functions $f(\hat{\mathbf{w}})$, i.e., all segments are independent:

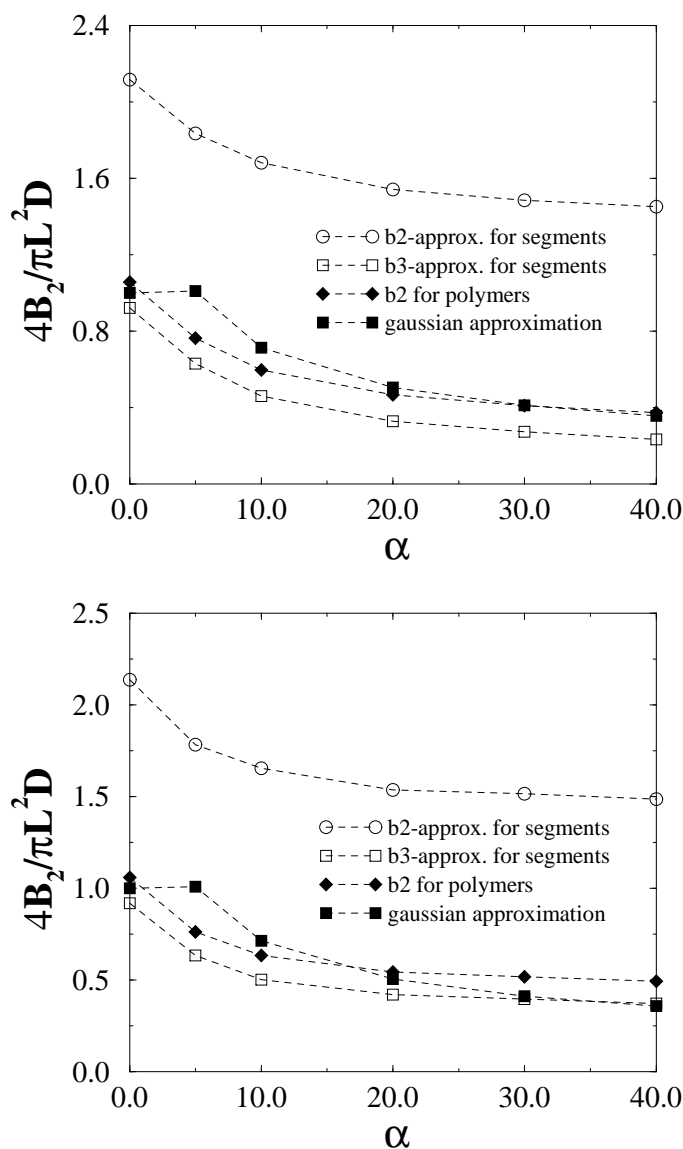$$\rho(\{\mathbf{r}\}, \{\Omega\}) = \prod_{j=1}^{k} f(\hat{\mathbf{w}}_j) \tag{5.38}$$

FIGURE 5.5 The reduced second virial coefficient for semiflexible polymers with $l_P = 1000$ (top) and $l_P = 100$ (bottom) in units of the segment length versus the width α of the Gaussian distribution function. The second virial coefficient for an isotropic distribution function is plotted at $\alpha = 0$. The length of the polymers $L = 10$ and the diameter $D = 0.25$. The open circles and squares denote the second virial coefficient, if we truncate the diagrammatic expansion at the two-segment interaction and the three-segment interactions, respectively. The black diamonds denote the second virial coefficient for polymers computed numerically. The gaussian approximation is shown by the black squares. The dashed lines are mount as a guide to the eye.

Note that this functional form neglects the connectivity of the segments. Second, only the first term in the righthand-side of Eq. 5.37 is taken into account, which means that the simultaneous overlap of more than two segments is neglected.

In order to investigate the influence of both the connectivity of the segments and the more-than-two-segment overlaps, we computed numerically the second virial coefficient for polymers consisting of 10 hard spherocylinders with a $\ell/D = 4$, where ℓ is the length of a segment and D the diameter. We generated for a specific persistence length two polymer configurations. For the generation of polymer configurations, we should know the exact form of the distribution function $\rho(\{\mathbf{r}\}, \{\Omega\})$, which depends on the alignment to the nematic director and the internal bending energy. For very stiff chains, we can assume that the first segments of both chains are distributed according to an orientational distribution function $f(\hat{\mathbf{w}}_1)$, which is either an isotropic distribution function or a gaussian distribution function with a specific width α. The following k-1 segments are distributed according to the internal bending energy. These assumptions correspond to a distribution function:

$$
\begin{aligned}
\rho(\{\mathbf{r}\}, \{\Omega\}) &= f(\hat{\mathbf{w}}_1) \prod_{j=2}^{k} \exp(-\beta\theta^2_{\hat{\mathbf{w}}_j \hat{\mathbf{w}}_{j-1}}) \\
&\times V \, \delta(\mathbf{r}_j - \mathbf{r}_{j-1} - (\hat{\mathbf{w}}_j + \hat{\mathbf{w}}_{j-1})/2)
\end{aligned}
\tag{5.39}
$$

where the delta-functions ensure the connectivity. The centre of mass of the second polymer was randomly chosen within a sphere of radius L around the centre of mass of the first polymer. When the polymer configurations result in an overlap, we can compute the several contributions to the different diagrams in Fig. 5.4. As it is too time-consuming to identify all the segment-segment overlaps in the two overlapping chains, we only computed the contributions to the two- and three-segment interactions (first and first three terms in the diagrammatic expansion). In Fig. 5.5, we plotted the reduced second virial coefficient $4B_2/(\pi L^2 D)$ for polymers with persistence length l_P = 100 and 1000 versus the width α of $f(\hat{\mathbf{w}}_1)$, if we only take into account the two-segment interactions (first diagram in Fig. 5.4), the two- and three-segment interactions (first three terms) and if we take into account all diagrams. The results for an isotropic distribution function is shown at $\alpha = 0$. For the sake of comparison, we also plotted the second virial term for a fluid of disconnected segments, on which most theories are based. Using a gaussian distribution function, we can compute that this second virial term in Eq. 2.19 is equal to $4/\sqrt{\pi\alpha}$.

We observe clearly that for polymers with persistence length l_P = 100 and 1000, the connectivity influences the first term in the diagrammatic expansion dramatically. We significantly underestimate the two-segment interaction term in a polymer-polymer
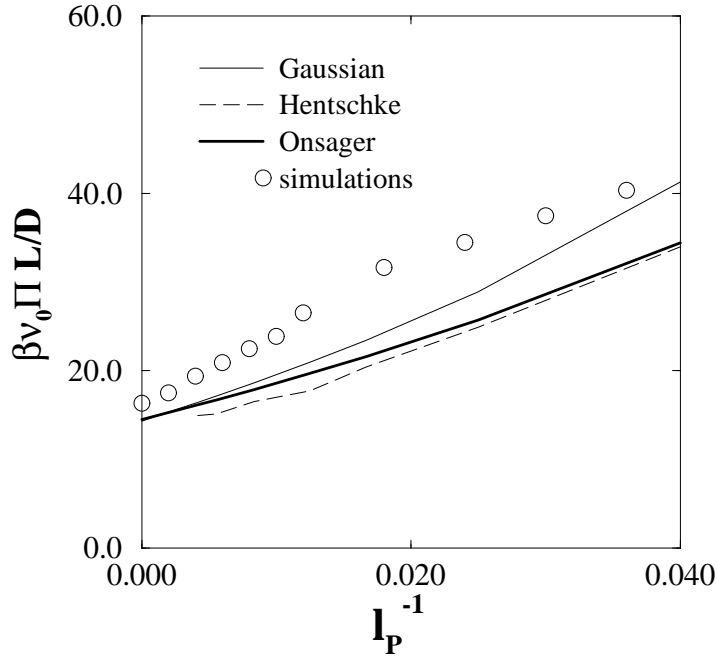
FIGURE 5.6   The pressure versus the inverse persistence length for a three-dimensional system of semiflexible polymers with $L/D = 40$.

interaction by neglecting the connectivity. If one segment of polymer A overlaps with a segment of B, the probability that another segment of A overlaps with B is extremely large as shown in Fig. 5.3. For the isotropic distribution function, we found, for instance, a polymer-polymer interaction that is more than twice as large as the polymer-polymer interaction, if we take into account all diagrams. Thus, when two polymer configurations result in an overlap, we observe on average two overlapping segment pairs in these chains. This effect is strongly pronounced as the ℓ/D of the segments is small (in the present case: $\ell/D = 4$!). However, if we also take into account the three-segment interaction term, the polymer-polymer interaction decreases and if we take into account all interaction terms it increases slightly again. We also observe that the polymer-polymer interaction truncated at the first and the third diagram is only roughly shifted by a constant from the full polymer-polymer interaction. As the coexisting densities are calculated by equating free energy derivatives (see Eq. 5.2), the value of this constant is not important for the prediction of the phase diagram. Note that the numerically calculated reduced second virial coefficient for an isotropic distribution function is slightly larger than one as a result of end effects. If we now compare in more detail the second virial term for a fluid of disconnected segments with the full polymer-polymer interaction calculated numerically, we observe that this second virial term is larger for small α and smaller for large α. We can now use these numerically
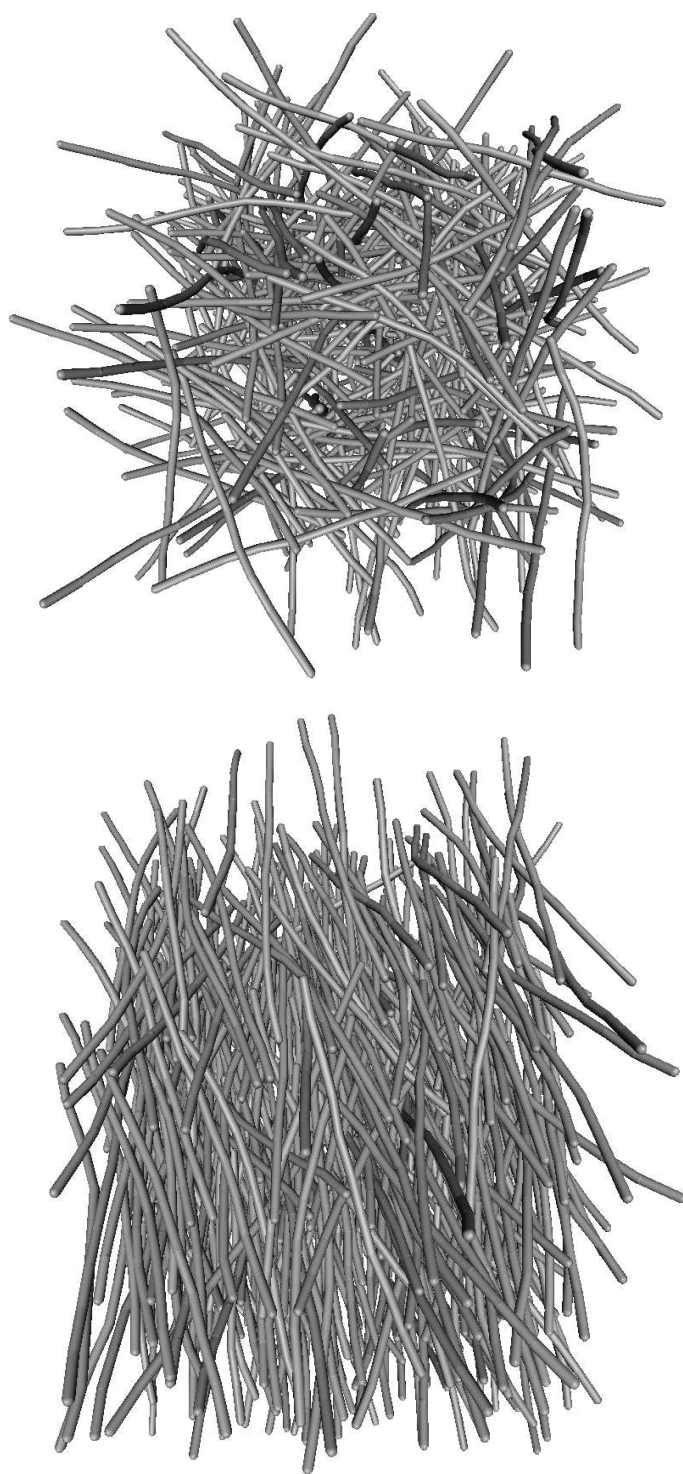
FIGURE 5.7   Typical configurations for a system of semiflexible polymers with persistence length $l_P = 160$ in units of the segment length in the coexisting isotropic (top) and nematic phase (bottom).

computed second virial coefficients in Odijk's approach (Eq. 5.20) and we find the following coexisting densities for $l_P = 100$ and 1000:

$$l_P = 1000 : \quad c_{\text{iso}}^* = 3.06 \pm 0.15 \qquad c_{\text{nem}}^* = 3.76 \pm 0.09$$
$$l_P = 100 : \quad c_{\text{iso}}^* = 3.26 \pm 0.10 \qquad c_{\text{nem}}^* = 4.06 \pm 0.12$$

These values are much closer to the simulation results than all previous theoretical results. Apparently, the functional form of the second virial coefficient on the width α of the orientational distribution function is of great importance. Unfortunately, if we do the same for $l_P = 10$, we could not find a stable solution. Since all theories do predict a first order isotropic-nematic phase transition for semiflexible polymers with $l_P = 10$, we conclude that our numerical calculation of the second virial coefficient as a function of α may have been too naive, in the sense that the generation of the two polymers according to Eq. 5.39 is not entirely correct. In the real many-body system, the segment distribution functions depends besides the internal bending energy, also on a tendency to align along the nematic director. This coupling with the molecular nematic field was not taken into account in Eq. 5.39, where the first segment is generated according to the molecular orientation $f(\hat{w}_1)$ and the following segments according to the internal Boltzmann factor. The effect of this coupling with the nematic field would be a stronger alignment of the segments, yielding a smaller effective second virial coefficient. This alignment effect is expected to be stronger for more flexible chains and this might be the reason why we did find a solution for $l_P = 100$ and 1000 and not for $l_P = 10$. This indicates again that the exact functional form of the second virial coefficient on the width α of the orientational distribution function is of great importance. Further analysis of the second virial coefficient is therefore needed.

A third reason why the theories overestimate the coexisting densities may be that the second virial approximation for polymers is not valid. In Ref. [34], it is shown that for hard spherocylinders with $L/D = 5$, 10 and 100, the reduced third virial coefficient B_3/B_2^2 is equal to respectively 0.4194, 0.3133 and 0.0698 in the isotropic phase. In the nematic phase, the contributions of higher virial coefficients is expected to be even higher. In the limiting case of perfectly parallel spherocylinders, the probability of three overlapping particles is completely not negligible. Only for very high L/D, higher virial coefficients may be neglected.

Finally, we look in more detail to the different theories. Hentschke used instead of the second virial approximation a generalisation of the Carnahan-Starling equation for hard spheres to the case of spherocylinders, which yields good agreement with Monte Carlo simulations for short spherocylinders [93]. In Fig. 5.2, we observe clearly that the width of the coexistence region in the simulations is much larger than predicted

by Hentschke. Using the Onsager approximation with a Gaussian or Onsager's trial function, the predicted width of the coexistence region is larger. However, for high flexibility the width becomes very small, when we use the Onsager trial function, whereas the width remains more or less the same, when a Gaussian trial function is used. Using the Gaussian trial function, Odijk derived a closed expression for the orientational free energy for arbitrary chain length. However, when the Onsager trial function was used, we had to interpolate the rod and the semiflexible limit in the form of a Padé approximant in order to obtain a formula valid for arbitrary flexibility. In our simulations, we observe that the width decreases slightly with inverse persistence length for $0 \ll l_P^{-1} \ll 0.04$. In Fig. 5.6, we show the pressure versus the inverse persistence length. The pressure in the simulations are higher than predicted by all theories. Fig. 5.7 shows typical configurations of the coexisting isotropic and nematic phases for semiflexible polymers with persistence length $l_P = 160$.

In summary, we have performed Monte Carlo simulations of a three-dimensional system of semiflexible polymers consisting of 10 hard spherocylinders connected to each other. Using the Kofke method, we were able to perform simulations along the isotropic-nematic coexistence curve. We clearly observe that our simulation results for the coexisting densities are shifted systematically to lower densities compared with the current theories.

6

PHASE SEPARATION IN BINARY HARD-CORE MIXTURES

In this chapter, we investigate the stability of binary mixtures of hard cubes of sidelength σ_1 and σ_2, respectively. We find that a purely entropic demixing transition takes place, if σ_2/σ_1 is sufficiently large. A simple theoretical criterion can be used to predict the presence of phase separation. This criterion is based on the value of the pair distribution function at contact. In addition, we present simulations of a single athermal polymer in a hard-core solvent, which collapses as the chemical potential of the solvent is increased. Again, this collapse transition is purely entropy-driven.

6.1   Introduction

One of the most striking phenomena in mixtures is phase separation into two or more coexisting phases of different composition. The theoretical study of the causes of phase separation in binary mixtures is one of the oldest in statistical thermodynamics. In fact, for simple liquid mixtures [99] the first microscopic theories date back to van der Waals [14], while for polymer solutions the Flory-Huggins theory plays a similar role [24, 100]. In view of the almost overwhelming amount of experimental and theoretical work that has since been spent on the study of liquid mixtures, one might think that the factors that are responsible for demixing are, by now, well understood. Surprisingly, this is not the case. In particular, it is still an unresolved question, if demixing can be driven by entropic effects alone.

In Chapter 1, we have already mentioned that a phase transition will only occur in a system at constant volume and temperature T, if this results in lowering the Helmholtz free energy $F = E - TS$. In "athermal" mixtures, i.e., mixtures of particles that have

only excluded volume interactions, phase separation can only occur, if demixing results in an *increase* of the entropy. To a first approximation, the entropy of mixing of a binary mixture is equal to the entropy of mixing of an ideal mixture (see also Eq. 2.5):

$$S_{\mathrm{id}}(x) = -N k_B [x \log x + (1-x) \log(1-x)] \tag{6.1}$$

where x denotes the number fraction of one component and N the number of particles. From Fig. 6.1, which shows the entropy of mixing of an ideal mixture versus the number fraction, we can conclude that phase separation results always in a decrease in entropy. This implies that we should never observe a demixing transition in a hard-core mixture. Also our intuitive interpretation of entropy suggests that a system should have a higher entropy in the mixed phase than in the demixed phase with the same density and energy. However, it is dangerous to use our intuitive notion of disorder to estimate entropy. One trivial way in which phase separation can happen in an athermal mixture is, if the hard-core interactions in the mixture are "non-additive", i.e., $\sigma_{AB} > (\sigma_{AA} + \sigma_{BB})/2$, where σ_{ij} denotes the distance of closest approach of particles of type i and j [101–103]. For such systems the pure phases can fill space more effectively than the mixture. More interesting is the case of *additive* hard-core mixtures, for which $\sigma_{AB} = (\sigma_{AA} + \sigma_{BB})/2$, and here the situation is more confused. For additive hard sphere mixtures, we have two conflicting predictions. In 1964 Lebowitz and Rowlinson [104] showed that the (approximate) Percus-Yevick integral equation for hard sphere mixtures predicts no fluid-fluid phase separation for any size ratio or density. Indeed, simulations of hard sphere mixtures have thus far not provided any evidence for fluid-fluid demixing [105–109]. However, more recently Biben and Hansen [110], using the so-called Rogers-Young integral equation for hard sphere mixtures, found evidence for a spinodal instability in a fluid mixture of spheres of sufficiently dissimilar sizes. Similar predictions have subsequently been made with other approximations [111]. In principle, computer simulation is a suitable tool to investigate whether phase separation can take place in purely athermal mixtures. Unfortunately, direct simulation of phase separation in mixtures of very dissimilar spheres is difficult because of slow equilibration [112]. The numerical difficulties are less severe for lattice models of hard-core mixtures. We have therefore performed simulations of lattice models of additive hard-core particles.

The results of grand canonical Monte Carlo simulations of a mixture of large and small cubes with side ratios of 2 or 3 on a cubic lattice are reported in this chapter. In section 6.2, the simulation method is discussed and the results are presented. The more technical aspects of the simulation method are explained in the Appendices of this chapter. A question related to phase separation induced by purely entropic effects is whether an athermal polymer in a hard-core solvent undergoes a collapse transition. The
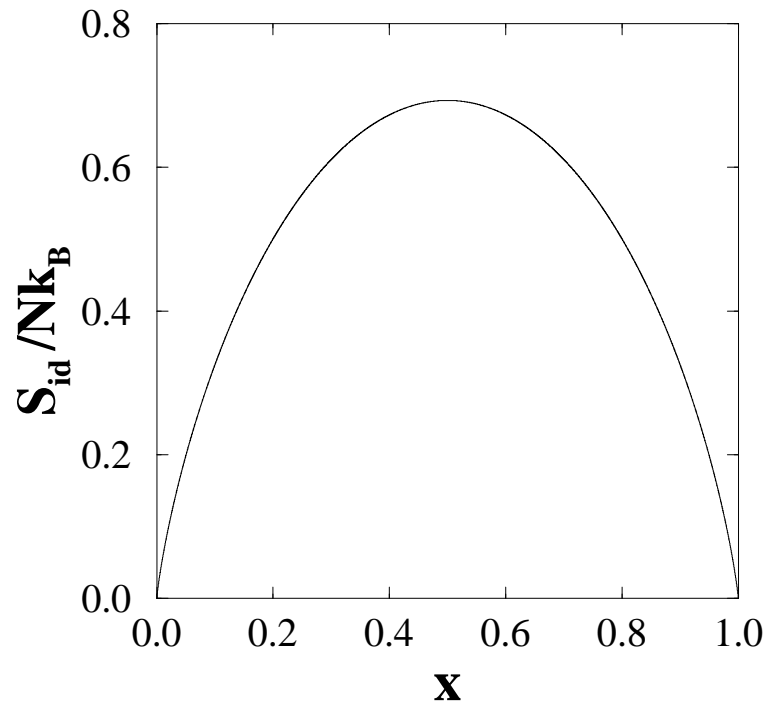
FIGURE 6.1 The entropy of mixing of an ideal binary mixture versus the number fraction x.

results of a simulation of such a system are reported in section 6.3. In section 6.4, we show that in an off-lattice system of large and small parallel cubes the pair distribution function of large cubes diverges at contact in the limit $\sigma_1/\sigma_2 \rightarrow 0$, where σ_1 and σ_2 are the side lengths of the cubes. This tendency of the large cubes to stick together is strongly suggestive of phase separation. For the lattice system, we computed the pair distribution functions of the binary hard cube mixture and compared them with the pair distribution functions for a pure system at the same packing fraction.

6.2 Computer Simulations of a Binary Mixture of Hard Parallel Cubes

6.2.1 Simulation Method

The model that we consider is a mixture of large and small parallel hard cubes on a lattice. The sidelength of each cube corresponds to an even number of lattice spacings.
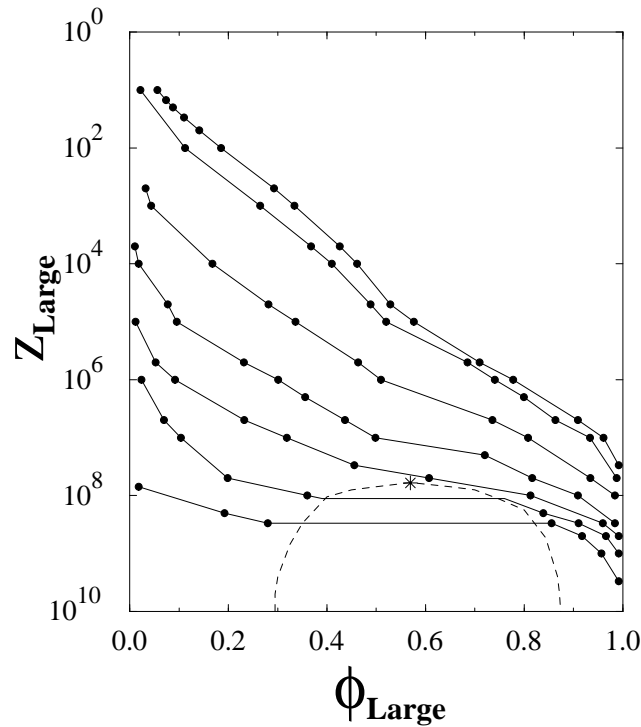
FIGURE 6.2   The fugacity of the large cubes (size 6×6×6) versus the volume fraction of the large cubes at different fugacities (z_s=0, 100, 500, 1 10^3, 1.5 10^3, 2 10^3, and 5 10^3, from top to bottom) of the small particles (size 2×2×2). The star denotes the critical point ($z_l = 6.02\ 10^7$, $z_s = 1.63\ 10^3$, ϕ_{Large}=0.57) and is derived by a global fit of all isofugacity curves. The rest of the binodal (dashed) curve could not be estimated as accurately as the critical point. This curve should therefore be considered as a guide to the eye.

This model is clearly additive: at close packing we can fill space just as well in the mixed phase as in the pure phases. Hence there is no trivial volume-driven demixing. In our simulations we considered mixtures of cubes with side ratios of 2 or 3 on a lattice with respectively 28×28×28 and 30×30×30 lattice points. In both cases, the sidelength of the small cubes is equal to 2. We performed grand canonical Monte Carlo (GCMC) simulations, where the independent variables are the fugacities of the large and the small cubes, z_l and z_s. Three types of trial moves can be performed:

- Random displacement of a particle in the box.

- Changing the identity of a particle (large to small or vice versa).
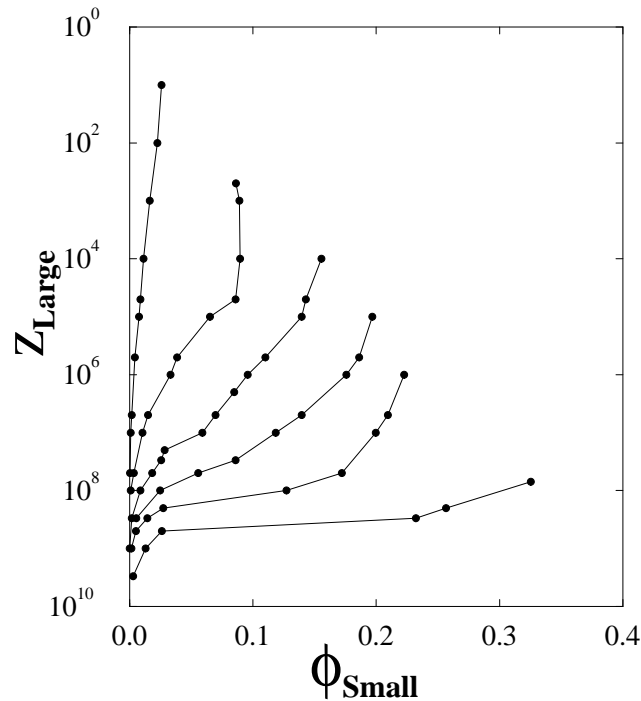
- Removal or insertion of a particle.

FIGURE 6.3 The fugacity of the large cubes (size $6 \times 6 \times 6$) versus the volume fraction of the small cubes at different fugacities (z_s=0, 100, 500, 1 10^3, 1.5 10^3, 2 10^3 and 5 10^3, from top to bottom) of the small particles (size $2 \times 2 \times 2$).

However, the acceptance ratio for a random displacement of a large particle is small in a dense system of small particles, as the displacement of a large particle is strongly hindered by the small particles. In order to speed up equilibration, we used collective particle moves that employed a generalisation of the configurational-bias Monte Carlo scheme of Ref. [61]. In this approach, the large particle was moved to a random trial position. Typically several small particles would occupy this region in space. These particles were then moved to the volume vacated by the large particle and inserted using Rosenbluth sampling [112]. The trial move was then accepted with a probability determined by the ratio of the Rosenbluth weights of the new and old configurations. Of course, a trial move would be rejected immediately if it resulted in overlap of two or more large particles. In order to investigate the influence of the surface-to-volume ratio on phase separation, we also performed simulations of a three-dimensional system of hard parallel platelets (size $6 \times 6 \times 2$) and cubes (size $2 \times 2 \times 2$) on a cubic lattice of $30 \times 30 \times 30$. For the sake of comparison, we also simulated a two-dimensional mixture of hard squares (size 6×6 and 2×2) and a two-dimensional system of hard squares (size
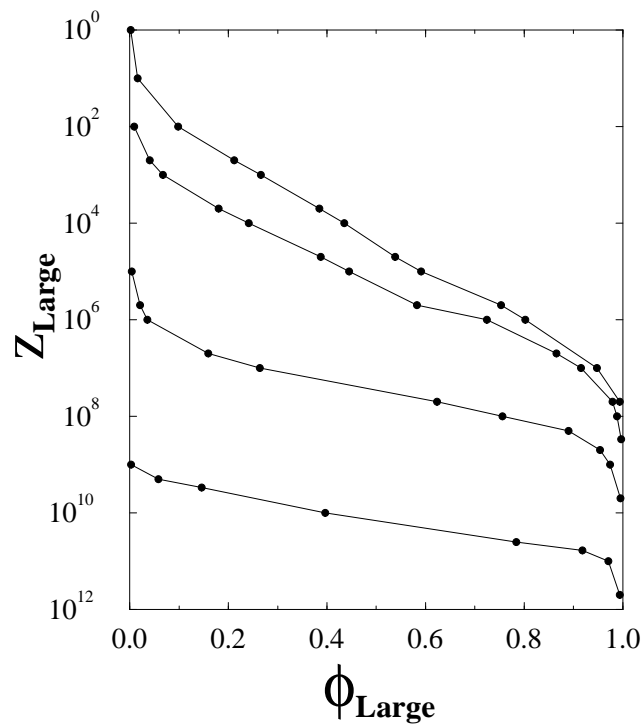
FIGURE 6.4   The fugacity of the large cubes (size $4{\times}4{\times}4$) versus the volume fraction of the large cubes at different fugacities (z_s=100, 1 10^3, 1 10^4, and 1 10^5, from top to bottom) of the small particles (size $2{\times}2{\times}2$).

$2{\times}2$) and parallel hard rods ($18{\times}2$).

6.2.2   Results

GCMC simulations were performed on a mixture of large and small cubes for a range of different values for the fugacities z_l and z_s. In each simulation, we computed the volume fractions of the large and small cubes. For a faster equilibration, subsequent runs were started from previously equilibrated configurations at a higher or lower fugacity. Most runs consisted of $1 \times 10^5 - 1 \times 10^6$ cycles per particle. In each cycle, we attempt a displacement of a particle in the box, and we try to change the identity of a random particle. Once every ten cycles, a removal or insertion of a particle in the box is attempted. In Figs. 6.2 and 6.3, the fugacity of the large cubes is plotted versus the volume fraction of the large cubes and versus the volume fraction of the small cubes for a mixture of cubes with side ratio 3. The different curves in the figures are computed at constant fugacity of the small cubes. In Fig. 6.4, we plot the fugacity of the large cubes

versus the volume fraction of the large cubes for a mixture of cubes with size $4 \times 4 \times 4$ and $2 \times 2 \times 2$ (volume ratio 2). For a side ratio of 3, we observed that upon increasing the fugacity of the solvent (i.e., of the small particles) the slope of the curves of constant solvent fugacity tends to zero at the inflection point. For still higher solvent fugacity, we find *two* different volume fractions of the large cubes for the *same* fugacity of the large particles (see Fig. 6.2). In Fig. 6.3, we observe the same flattening of the isofugacity curves. For still higher solvent fugacity, we again find *two* different volume fractions of the small cubes for the *same* fugacity for the large cubes.

This is exactly what we expect for a demixing transition. The critical point can now be derived from a global fit of all isofugacity curves. When we take this into account, we can sketch the demixing region, as shown in Fig. 6.2. As the cubes are equally likely to be found on all lattice sites in both phases (i.e., there is no sublattice ordering), the present phase transition corresponds most closely to liquid-liquid coexistence in an off-lattice system. The simulations in the demixing region are very time consuming and therefore we have not attempted to locate the binodal curve more accurately. For a side ratio of 2, we find no evidence for a similar flattening of the isofugacity curves and we did not find two different volume fractions of the large cubes for the same fugacity of the large particles. Thus we find no evidence for a demixing transition in the less asymmetric system. However, if instead of cubes, we consider platelets, with a comparable volume ($6 \times 6 \times 2$, instead of $4 \times 4 \times 4$), we again observe demixing (see Fig. 6.5). This is plausible as the clustering of the particles is controlled by depletion forces: in the case of two large cubes far from each other, the small cubes are excluded from a depletion layer with thickness $\sigma_1 / 2$ around the large cubes (see Fig. 6.6). When the two large particles are brought into contact, the depletion zones overlap and the volume accessible to the small particles increases by an amount that is proportional to the sidelength of the small particles and the area of contact of the large particles. The resulting gain in entropy of the solvent is the driving force that makes the large particles cluster. The larger the surface-to-volume ratio of the large particles, the stronger is the tendency to demix.

In a two-dimensional mixture of squares with size 6×6 and 2×2, we did not find demixing. At the same "volume ratio" but with rods of size 18×2 instead of the large squares (larger surface), the system appeared to approach a spinodal, but we were not able to reach it.

6.3 Simulations of an Athermal Polymer

The driving force that makes the particles cluster depends on the surface-to-volume ratio of the large particles. This argument should apply not only to rigid particles,
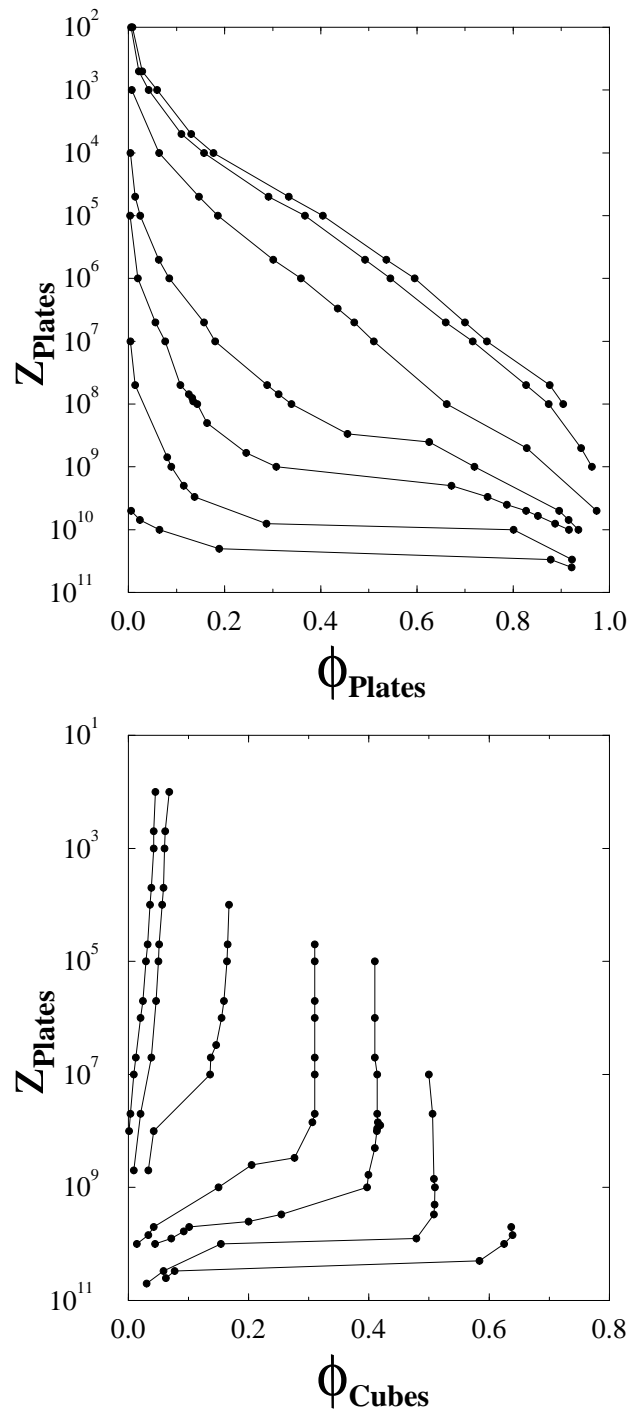
FIGURE 6.5   The fugacity of the platelets (size $6 \times 6 \times 2$) versus their volume fraction (top) and versus volume fraction of the small cubes (bottom) at different fugacities (z_s=5 10^2, 10^3, 10^4, 5 10^4, 10^5, 2 10^5 and 5 10^5, from top to bottom) of the small particles (cubes of size $2 \times 2 \times 2$).

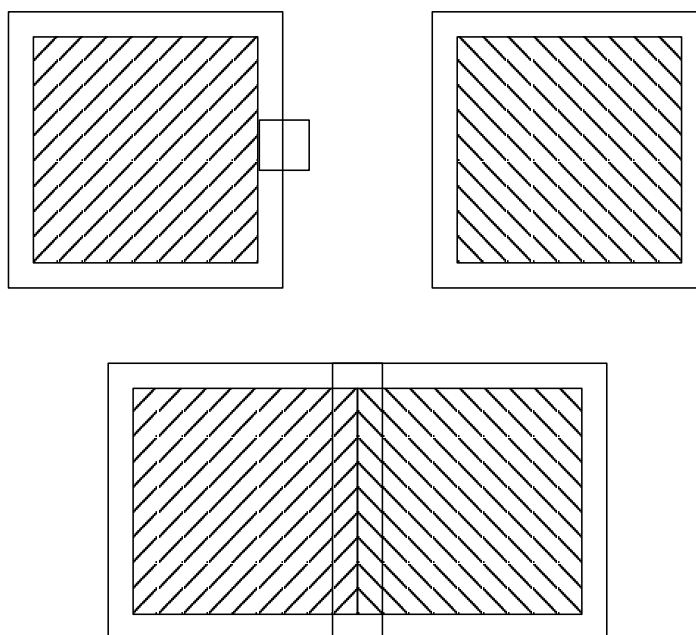FIGURE 6.6   When the two large particles are brought together, the depletion
zones overlap and the accessible volume for the small particles increases.

such as rods and disks, but also to flexible particles, such as linear polymers. We
therefore also looked for entropic demixing in an athermal polymer solution. In fact,
in this case, we did not study the demixing directly. Rather, we looked for a closely
related phenomenon, namely, the solvent-induced collapse of an isolated polymer. This
collapse signals the transition from the good-solvent to the poor-solvent regime. There
are compelling theoretical arguments to assume that a polymer collapse must occur in an
athermal polymer solution when the polymer-solvent interaction is *nonadditive* [80]. In
order to investigate if such a collapse can also occur in an "additive" athermal polymer
solution, we performed simulations of a single hard-core polymer in a solvent of cubes,
where the size of the cubic monomers of the polymer is the same as the size of the
solvent molecules, namely, $2 \times 2 \times 2$ in units of the lattice spacing.

For the simulation of the hard-core polymer in a solvent, we used the configurational-
bias Monte Carlo (CBMC) method [61] for generating polymer conformations and the
GCMC method for the solvent. Thus we performed the simulations on a system with
fixed volume and temperature and at constant chemical potential of the solvent. The
following trial moves have been performed:

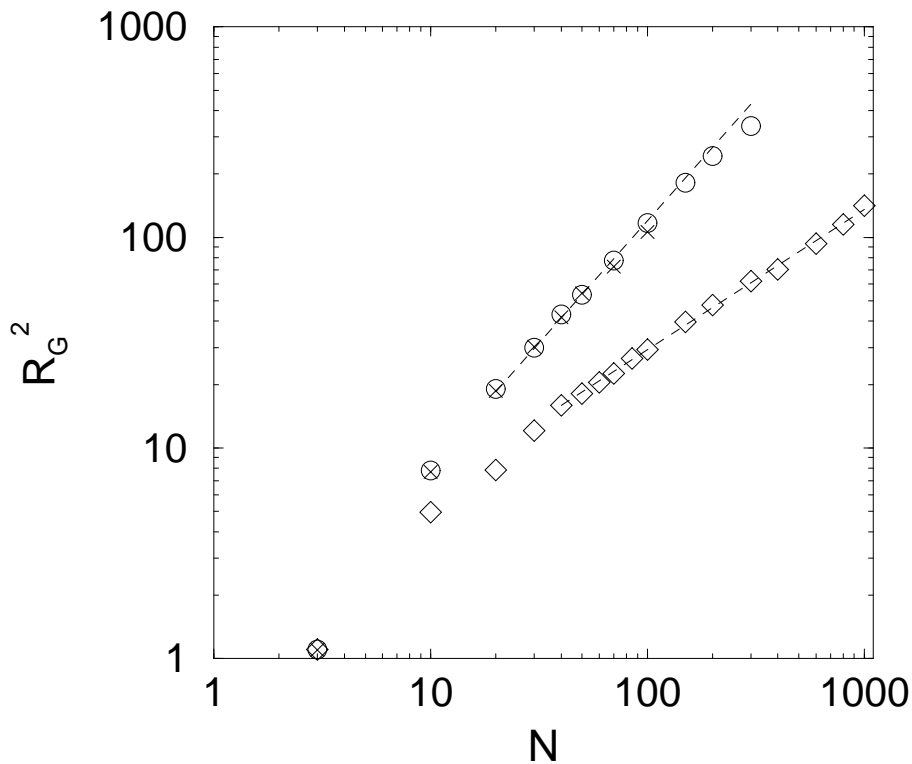- Random displacement of a solvent molecule in the box.

FIGURE 6.7   The mean square of the radius of gyration (R_g^2) of a polymer with cubic monomers (cubes of size 2×2×2) with and without solvent (cubes of size 2×2×2) versus the number of segments. Average solvent volume fraction: 0.0 (circles), 0.3 (crosses) and 0.7 (open diamonds). Note that R_g^2 scales as $N^{2\nu}$, with the number of monomers (N). For the two low density runs, we find $\nu=0.56\pm0.02$ (for a polymer in a good solvent $\nu \approx 0.58$). The high density run yields $\nu = 0.34 \pm 0.02$. For a collapsed polymer, we expect 'Euclidian' scaling: $\nu=1/3$.

- Removal or insertion of a solvent molecule.

- Regrowing a fraction of the polymer at either end of the chain.

- Regrowing a fraction of the polymer that does not include a free chain-end.

The last trial move was essential for a faster equilibration of the polymer and is explained in more detail in Appendices B and C of this chapter. The dependence of the radius of gyration R_g on the number of monomers N is shown in Fig. 6.7 at different chemical potentials of the solvent. Fig. 6.7 shows that when the chemical potential and hence the volume fraction of the solvent is increased, the polymer undergoes a collapse transition. We find that the square of the radius of gyration R_g^2 scales as $N^{2\nu}$. For the two low
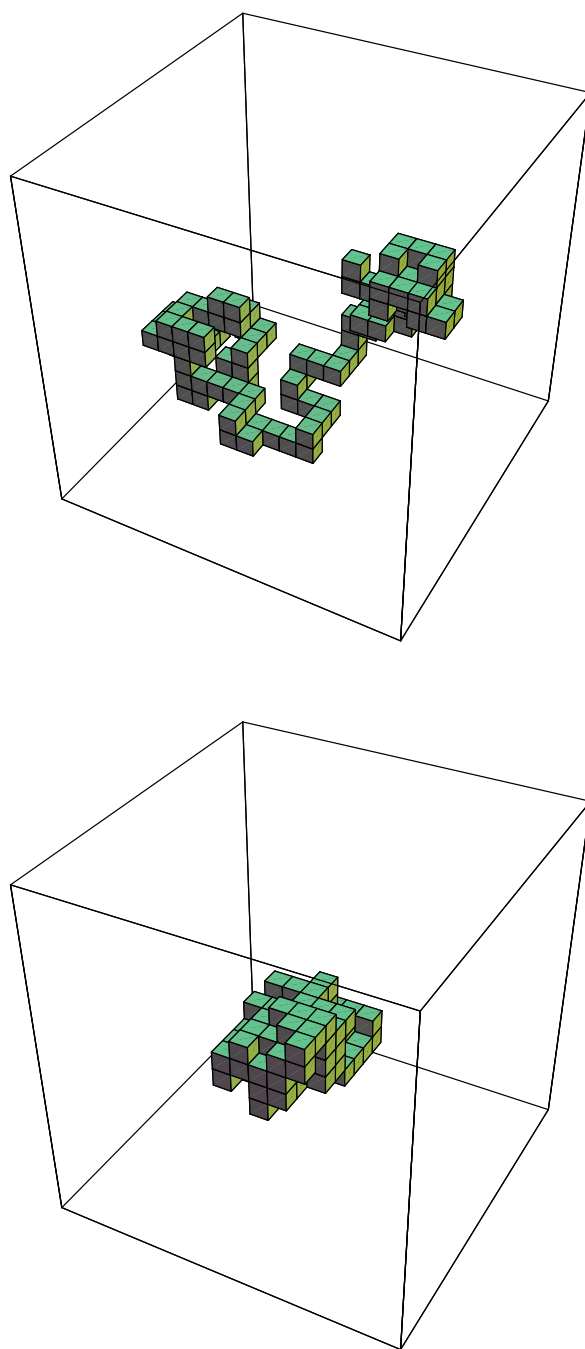
FIGURE 6.8 A snapshot of a conformation of a hard-core lattice polymer
(N=100) *without* hard-core solvent (top) and in a solution of hard-core monomers
with a volume fraction of 0.7 (bottom). Note the solvent-induced collapse.

chemical potentials, that correspond to solvent volume fractions of 0 and about 0.3, we find $\nu = 0.56 \pm 0.02$, which corresponds to the case of a polymer in a good solvent ($\nu \approx 0.58$). For high chemical potential (average solvent volume fraction of 0.7), we find $\nu = 0.34 \pm 0.02$. For a collapsed polymer, we expect 'Euclidian' scaling $\nu = 1/3$. Fig. 6.8 shows the very drastic change in the polymer shape when we go to high chemical potential of the solvent.

6.4   Virial Expansions for a Binary Mixture of Hard Parallel Cubes

6.4.1   Continuous System: Behaviour of g(r) for $\lambda \to 0$

In order to gain a better understanding of the physical origin of phase separation in a hard cube mixture, we analyse the density expansions of the pair-distribution function of a closely related model, viz., parallel hard cubes off lattice. For the one-component parallel hard cube model, the virial expansion of the pressure and the pair correlation function has been reported in the literature up to terms of order ρ^7 [113–115]. Here we consider the virial expansion of the same quantities for the binary mixture. For two cubes with side length σ_1 and σ_2 at $\mathbf{r_1}$ and $\mathbf{r_2}$ the Mayer function is defined by

$$f_{12}(\mathbf{r_1}, \mathbf{r_2}) = -\prod_{i=1}^{3} \Theta(\sigma_{12} - |r_{1,i} - r_{2,i}|) \tag{6.2}$$

where $\Theta(x)$ is the Heavyside step function and $\sigma_{12} = (\sigma_1 + \sigma_2)/2$. We computed the virial coefficients, up to the fourth, for the pair distribution function of the large particles, i.e., $g_{22}(x, y, z)$, as the latter quantity is expected to show evidence of incipient clustering that precedes demixing. If we define $\phi \equiv \phi(x, y, z)$ as the potential energy of a pair of particles, one at the origin and the other at (x, y, z), the virial expansion for $g_{22}(x, y, z) \exp(\beta\phi)$ in the densities ρ_1 and ρ_2 is [44]

$$
\begin{aligned}
g_{22}(x, y, z)\exp(\beta\phi) \quad = \quad & 1 + \rho_1 \;\; \text{⟨diagram⟩} \\
& + \rho_2 \;\; \text{⟨diagram⟩} \\
& + \frac{\rho_1^2}{2} \; (2\,\text{⟨diagram⟩} + 4\,\text{⟨diagram⟩} + \text{⟨diagram⟩} + \text{⟨diagram⟩}) \\
& + \frac{\rho_1 \rho_2}{2} \; (4\,\text{⟨diagram⟩} + 4\,\text{⟨diagram⟩} + 4\,\text{⟨diagram⟩}) \\
& + \frac{\rho_1 \rho_2}{2} \; (2\,\text{⟨diagram⟩} + 2\,\text{⟨diagram⟩})
\end{aligned}
$$

$$+ \frac{\rho_2^2}{2} \; (\; 2 \; \text{◖◗} \; + 4 \; \text{◣} \; + \; \text{◢◣} \; + \; \text{◢◣} \;)$$

$$+ \cdots \cdots \tag{6.3}$$

The diagrams consist of circles and bonds. The circles represent the particle co-ordinates and the sizes of the circles denote the sizes of the particles. Open circles correspond to coordinates that are not integrated over, the black circles represent the variables of integration. The bonds between the circles are associated with the Mayer function. For example, the first diagram in the pair distribution function denotes

$$\int d\mathbf{r}_3 f_{13}(\mathbf{r}_1, \mathbf{r}_3) f_{23}(\mathbf{r}_2, \mathbf{r}_3) \tag{6.4}$$

where particles 1 and 2 are large cubes and particle 3 is a small cube. Note that the three-dimensional integral factorises into a product of three one-dimensional integrals. We calculated $g_{22}(\sigma_2, \sigma_2, \sigma_2) \exp(\beta\phi)$ and $g_{22}(0,0, \sigma_2) \exp(\beta\phi)$ up to the fourth virial coefficient. The expressions for these pair distribution functions in terms of the packing fractions $\eta_1 = \sigma_1^3 \rho_1$ and $\eta_2 = \sigma_2^3 \rho_2$ are

$$
\begin{aligned}
g_{22}(\sigma_2, \sigma_2, \sigma_2) \exp(\beta\phi) \;=\; & 1 + \eta_1 + \eta_2 \\
& + \eta_1^2 (-6 + \frac{3}{\lambda} + \frac{3}{2\lambda^2} + \frac{1}{4\lambda^3}) \\
& + \eta_1\eta_2(-\frac{3\lambda}{4} - 1 - \frac{3}{4\lambda}) + \eta_2^2(-\frac{5}{4}) \quad (6.5)
\end{aligned}
$$

$$
\begin{aligned}
g_{22}(0,0, \sigma_2) \exp(\beta\phi) \;=\; & 1 + \eta_1(1 + \frac{1}{\lambda} + \frac{1}{\lambda^2}) \\
& + 4\eta_2 + \eta_1^2(\frac{1}{\lambda} + \frac{5}{\lambda^2} + \frac{6}{\lambda^3} + \frac{1}{2\lambda^4}) \\
& + \eta_1\eta_2(\frac{\lambda^2}{4} - 2\lambda + 5 + \frac{11}{\lambda} + \frac{19}{4\lambda^2}) \\
& + 9\eta_2^2, \quad (6.6)
\end{aligned}
$$

where $\lambda = \sigma_1/\sigma_2$. For cubes facing each other $(0,0, \sigma_2)$ the divergence in $g_{22}(x, y, z)$ for $\lambda \to 0$ already appears in the third virial coefficient while for cubes diagonal to each other $(\sigma_2, \sigma_2, \sigma_2)$, the divergence only appears at the fourth virial coefficient. This is plausible because depletion forces are stronger when the area of contact of the large particles is larger. Thus in the first case, the depletion effect is stronger. In table 6.1, the values of the one-dimensional integrals are listed that correspond to the graphs.

graph	value for $x = \sigma$	value for $x = 0$
(graph)	σ_1	$2\sigma_{12}$
(graph)	σ_2	$2\sigma_2$
(graph)	$-2\sigma_1^2$	$-\sigma_1^2 - 2\sigma_1\sigma_2$
(graph)	$-\frac{1}{2}\sigma_1^2 - \frac{1}{2}\sigma_2^2 - \sigma_1\sigma_2$	$\frac{1}{2}\sigma_1^2 - \frac{3}{2}\sigma_2^2 - 2\sigma_1\sigma_2$
(graph)	$-2\sigma_2^2$	$-3\sigma_2^2$
(graph)	$\sigma_1^2 + \frac{1}{2}\sigma_1\sigma_2$	$\sigma_1^2 + 2\sigma_1\sigma_2$
(graph)	$\frac{1}{2}\sigma_1^2 + \sigma_1\sigma_2$	$-\frac{1}{2}\sigma_1^2 + \frac{3}{2}\sigma_2^2 + 2\sigma_1\sigma_2$
(graph)	$\frac{1}{2}\sigma_2^2 + \sigma_1\sigma_2$	$-\frac{1}{2}\sigma_1^2 + \frac{3}{2}\sigma_2^2 + 2\sigma_1\sigma_2$
(graph)	$\frac{3}{2}\sigma_2^2$	$3\sigma_2^2$
(graph)	σ_1^2	$4\sigma_{12}^2$
(graph)	$2\sigma_1\sigma_2$	$4\sigma_{12}\sigma_2$
(graph)	σ_2^2	$4\sigma_2^2$
(graph)	$-\sigma_1^2$	$-\sigma_1^2 - 2\sigma_1\sigma_2$
(graph)	$-2\sigma_1\sigma_2$	$\frac{1}{2}\sigma_1^2 - \frac{3}{2}\sigma_2^2 - 2\sigma_1\sigma_2$
(graph)	$-\sigma_2^2$	$-3\sigma_2^2$

TABLE 6.1   Values of the one-dimensional integrals that correspond to the graphs with $\sigma_{12} = (\sigma_1 + \sigma_2)/2$

r	graph 1	graph 2	graph 3	graph 4	graph 5	graph 6	graph 7	graph 8	graph 9	graph 10	graph 11	graph 12	graph 13	graph 14	graph 15
0	7	11	-19	-47	-91	19	47	47	91	49	77	121	-19	-47	-91
1	6	10	-18	-46	-90	17	45	41	85	36	60	100	-16	-40	-80
2	5	9	-15	-43	-87	14	42	34	78	25	45	81	-13	-33	-69
3	4	8	-12	-39	-82	11	38	27	70	16	32	64	-10	-26	-58
4	3	7	-9	-34	-75	8	33	20	61	9	21	49	-7	-19	-47
5	2	6	-6	-28	-66	5	27	13	51	4	12	36	-4	-12	-36
6	1	5	-3	-21	-55	2	20	6	40	1	5	25	-1	-5	-25
7		4	-1	-15	-45		14		30			16			-16
8		3		-10	-36		9		21			9			-9
9		2		-6	-28		5		13			4			-4
10		1		-3	-21		2		6			1			-1
11				-1	-15										
12					-10										
13					-6										
14					-3										
15					-1										

TABLE 6.2   The values of the one-dimensional integrals that correspond to the graphs for $g_{22}(r)\exp(\beta\phi)$ are given for a discrete binary mixture of hard cubes with side lengths 6 and 2 in units of the lattice spacing.

6.4.2   Discrete Systems: Computation of g(r)

In order to make contact with the simulations described before, we also calculated the virial coefficients of $g_{22}(r)$ for the discrete model of a binary hard cube mixture, i.e., a cubic lattice with parallel hard cubes occupying σ_1^3 or σ_2^3 lattice points. As the virial coefficients are computed by counting lattice sites, it was necessary to fix the absolute size of the cubes rather than just their size ratio. We computed $g_{22}(r)$ for a system of cubes with size ratio 3 and size ratio 2. In both cases, the sidelength of the small cubes was equal to 2. In tables 6.2 and 6.3, the values for the one-dimensional integrals are listed that correspond to the graphs. We define a suitably averaged pair-distribution function by averaging over all values of $g_{22}(r)$ on the surface of a cube with side length r, analogous to the one used in Ref. [115]

$$g_{\mathrm{av}}(r) = \frac{1}{(2r+1)^2} \sum_{x=-r}^{r} \sum_{y=-r}^{r} g_{22}(x,y,z=r) \qquad (6.7)$$

r															
0	5	7	-13	-23	-37	13	23	23	37	25	35	49	-19	-23	-37
1	4	6	-12	-22	-36	11	21	19	33	16	24	36	-10	-18	-30
2	3	5	-9	-19	-33	8	18	14	28	9	15	25	-7	-13	-23
3	2	4	-6	-15	-28	5	14	9	22	4	8	16	-4	-8	-16
4	1	3	-3	-10	-21	2	9	4	15	1	3	9	-1	-3	-9
5		2	-1	-6	-15		5		9			4			-4
6		1		-3	-10		2		4			1			-1
7				-1	-6										
8					-3										
9					-1										

TABLE 6.3   The values of the one-dimensional integrals that correspond to the graphs for $g_{22}(r)\exp(\beta\phi)$ are given for a discrete binary mixture of hard cubes with side lengths 4 and 2 in units of the lattice spacing.

In Figs. 6.9 and 6.10, we have plotted $g_{\mathrm{av}}(r)$ versus r at different packing fractions and different size ratios. We see in Fig. 6.9 that for the binary mixture of hard parallel cubes with sizes $\sigma_1 = 2$ and $\sigma_2 = 6$, $g_{\mathrm{av}}(r = \sigma_2)$ for the large cubes is significantly higher than for a system with only large cubes at the same total packing fraction. Thus the addition of small cubes has the effect that the large cubes tend to stick together. On the contrary, for a binary mixture of cubes with size length $\sigma_1 = 2$ and $\sigma_2 = 4$, $g_{\mathrm{av}}(r = \sigma_2)$ is some what lower than for the pure system and the large particles are not prone to clustering when small cubes are added (see Fig. 6.10). However, if we consider a mixture of parallel platelets (size $6\times6\times2$) and cubes (size $2\times2\times2$) with a volume ratio comparable to the previous system, we see in table 6.5 that $g_{\mathrm{av}}(r = \sigma_2)$ in the binary mixture is larger than for a pure system of platelets. This can be explained by the larger surface-to-volume ratio of the platelets. The depletion effect is stronger when the area of contact of the two large particles that stick together is larger. The averaged $g_{\mathrm{av}}(r)$ is now obtained by averaging over all values for $g_{22}(r)$ on the surface of a platelet. In table 6.2 and 6.4, the values for the one-dimensional integrals are listed that correspond to the graphs that are needed to compute $g(r)$ in this binary system of platelets and cubes. In table 6.6, we see that for a two-dimensional system of squares with a side ratio of 3, $g_{\mathrm{av}}(r = \sigma_2)$ is not larger for a binary mixture, compared with a pure system at the same total packing fraction.

r					
0	3	-7	7	9	-7
1	2	-6	5	4	-4
2	1	-3	2	1	-1
3		-1			

TABLE 6.4   The values of the one-dimensional integrals that correspond to the graphs $g(r)\exp(\beta\phi)$ are shown here for a discrete system of hard cubes with side length 2 in units of the lattice spacing.

6.5   Conclusions

In section 6.4.1, we showed that for a binary hard-core mixture of parallel hard cubes with side lengths σ_1 and σ_2, the pair distribution function for the large particles diverges at contact in the limit $\sigma_1/\sigma_2 \to 0$. Thus, we expect, on the basis of these calculations a demixing transition for mixtures with sufficiently large size asymmetry. In a binary mixture of hard spheres with sidelengths σ_1 and σ_2, a similar divergence of the pair distribution function was found within the Percus-Yevick approximation in the limit $\sigma_1/\sigma_2 \to 0$ [116]. By computer simulations, we do indeed see a demixing transition in a lattice model of such a mixture provided that the size asymmetry of the large and small particles is larger than 2. When the size ratio of the cubes equals 3, we found clear evidence of a demixing transition in our simulations, but such demixing was not observed for a cube side ratio of two. However, if we consider platelets instead of the large cubes of comparable volume, the system will again become unstable with respect to phase separation. This can be explained by a stronger depletion effect for platelets. In a two-dimensional mixture of squares of size 6×6 and 2×2, we found no evidence for demixing. At the same "volume ratio", but with rods of size 18×2 instead of the large squares (larger surface), the system appeared to approach a spinodal. The simulations support the theoretical predictions by Sanchez [117] of the existence of entropy-driven demixing in binary solutions. He showed that the compressible nature of binary solutions and differences in the pure-component equation of state properties play an important role in solution thermodynamics. For instance, the description of phase stability separates into a constant volume (incompressible) contribution and a volume fluctuation (compressible) contribution. In most theories, the latter quantity has been neglected. However, this is only correct when the pure components have identical equation of state properties and interact neutrally with one another. When we take volume

$\eta_2 + \eta_1$	$\eta_1 = 0.0$	$\eta_1 = 0.2$	$\eta_1 = 0.4$	$\eta_1 = 0.6$	$\eta_1 = 0.8$
0.1	1.08883				
0.2	1.18029				
0.3	1.27436	1.46528			
0.4	1.37105	1.55950			
0.5	1.47037	1.65635	1.98181		
0.6	1.57230	1.75581	2.07880		
0.7	1.67685	1.85789	2.17842	2.63843	
0.8	1.78402	1.96260	2.28065	2.73819	
0.9	1.89381	2.06992	2.38551	2.84058	3.43513

TABLE 6.5   The values for the averaged $g_{\mathrm{av}}(r=6)$ are tabulated for a discrete system of hard parallel platelets of size 6×6×2 and packing fraction η_2 and with cubes of side length 2 and packing fraction η_1.

fluctuations into account, the system is able to explore other regions of configuration space corresponding to larger volumes and lower free energies. A compressible solution is, hence, thermodynamically less stable than an incompressible solution. In binary hard-core mixtures with sufficiently large size asymmetry, the equation of state properties of the pure components will be sufficiently different, so that compressibility contributions will play an important role in the description of phase stability.

In this context, it is interesting to consider what happens in the high-density limit. In that case, every lattice site will be occupied by either a large or a small particle. This can only be achieved if all particles order on a sub-lattice. However, once this spatial ordering has taken place, there is no longer any gain in entropy associated with demixing. Hence, at high densities, the two-dimensional system will mix again. In section 6.4.2, we computed the averaged pair distribution function at contact $g_{\mathrm{av}}(\sigma_2)$ for the large particles up to the fourth virial coefficient for several systems. We found that a comparison of the computed values for $g_{\mathrm{av}}(\sigma_2)$ for a binary mixture and for a pure system with only large particles at the same total packing fraction provides an indication of the tendency of the system to demix. In particular, we found a larger value of $g_{\mathrm{av}}(\sigma_2)$ only for the binary mixture of cubes with size ratio 3 and the mixture of platelets and small cubes compared with the pure system. By computer simulations, we indeed observed *only* in these systems a demixing transition. For the mixture of cubes with size ratio 2 and the 2-dimensional system of hard squares, we found a lower value for the pair distribution functions at contact in comparison with the pure systems. In

$\eta_2 + \eta_1$	$\eta_1 = 0.0$	$\eta_1 = 0.2$	$\eta_1 = 0.4$	$\eta_1 = 0.6$	$\eta_1 = 0.8$
0.1	1.11693				
0.2	1.25190				
0.3	1.40491	1.36601			
0.4	1.57597	1.53391			
0.5	1.76508	1.71985	1.67047		
0.6	1.97222	1.92384	1.87130		
0.7	2.19741	2.14586	2.09017	2.03032	
0.8	2.44065	2.38594	2.32708	2.26408	
0.9	2.70192	2.64405	2.58204	2.51587	2.44556

TABLE 6.6   The values for the averaged $g_{av}(r = 6)$ are tabulated for a two-dimensional discrete system of hard squares of size 6×6 and packing fraction η_2, and squares with side length 2 and packing fraction η_1.

the simulations of these systems, we found no phase separation. Thus the calculation of the pair distribution functions of the large particles at contact gives a rough estimate, whether the mixture is stable for phase separation.

Finally, we performed simulations of a hard-core polymer in a hard-core solvent. By increasing the solvent fugacity in this athermal polymer solution, we can make the polymer collapse. It is important to note that the collapse of the polymer chain in a solvent is, in a sense, counterintuitive. If one considers exclusively the polymer chain, there is a large amount of entropy lost by the collapsed polymer. However, the increase in entropy of the solvent molecules overrides this apparent loss. The observation of such a solvent-induced polymer collapse immediately implies the existence of a demixing transition in this athermal polymer solution. Also, in this case the polymer will expand again at high densities, as the gain in entropy associated with the polymer collapse will disappear for the same reason as mentioned above. The present simulations support existing theoretical predictions of the occurence of entropy-driven demixing in polymer blends and solutions. In particular, Freed and Bawendi [118] have argued on theoretical grounds that polymer blends in which monomers extend over several lattice sites, and therefore have different sizes and shapes, can demix. Similarly, Sanchez [117] has considered the inclusion of compressibility effects into the theory of polymer mixtures. Again, an entropy-driven phase separation is predicted. Hariharan and Kumar [119] studied the effect of compressibility in an athermal mixture of short and long chains in the vicinity of a hard wall by computer simulations. In such a mixture, the short
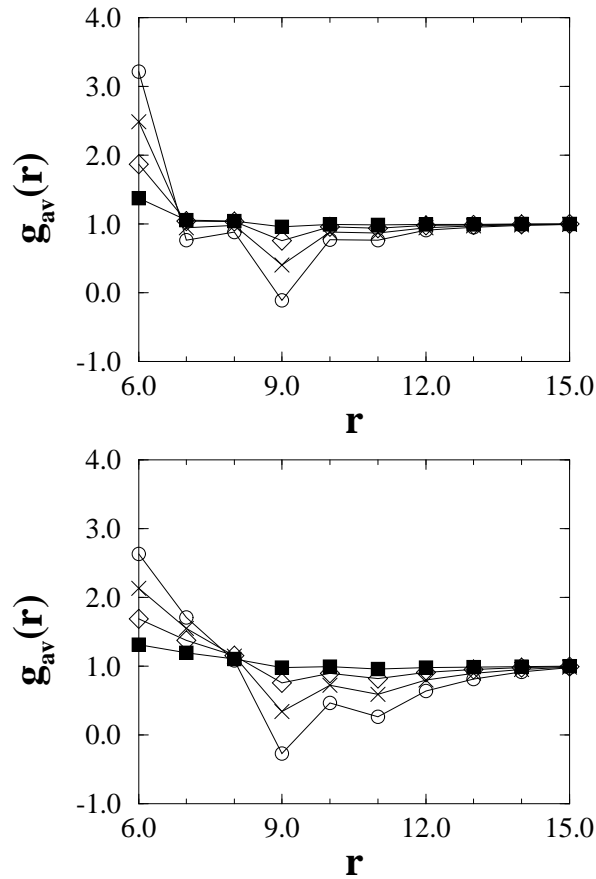
FIGURE 6.9   Top: $g_{\mathrm{av}}(r)$ versus r for a binary mixure of cubes (size $6\times6\times6$ and $2\times2\times2$) at equal packing fractions for the large and small cubes. Bottom: $g_{\mathrm{av}}(r)$ versus r for a system with only large cubes. In both pictures, the total packing fraction η is (black square) $\eta=0.2$, (open diamond) $\eta=0.4$, (cross) $\eta=0.6$, and (circle) $\eta=0.8$.

chains (which lose less entropy per segment) partition preferentially to the surface in order to minimize the entropy loss due to the presence of the wall and, Hariharan and Kumar find that the compressibility of the mixture enhances this effect. Simulations of athermal polymer solutions have been reported before [120], but a purely entropic polymer collapse has, to our knowledge, not been observed.
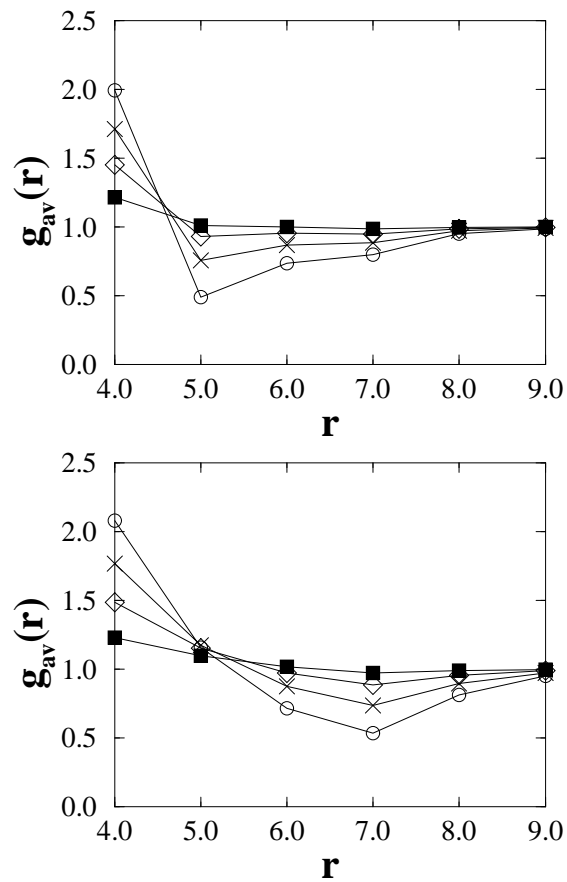
FIGURE 6.10 Top: $g_{\mathrm{av}}(r)$ versus r for a binary mixure of cubes (size $4\times4\times4$ and $2\times2\times2$) at equal packing fractions for the large and small cubes. Bottom: $g_{\mathrm{av}}(r)$ versus r for a system with only large cubes. In both pictures, the total packing fraction is (black square) $\eta=0.2$, (open diamond) $\eta=0.4$, (cross) $\eta=0.6$, and (circle) $\eta=0.8$.

Appendix A

In a dense system of small cubes, random displacement of a large particle, is difficult. To overcome this problem, we remove the small particles that hinder the displacement of the large particle and reinsert them into the space vacated by the large particle. The algorithm for moving a big particle goes as follows:

1. Choose a random displacement for the large particle.

2. If the large particle at its new position overlaps with another large particle, this move will immediately be rejected.

3. If there is no such overlap, the n small particles that will have overlap with the large particle at its new position will be determined.

4. The n small particles will be inserted in the volume that will become free when we displace the large particle to its new position.

The insertion of the n small particles into the free volume is not simple as the probability of random insertion of n particles in a restricted volume is small. We therefore used a method similar to the one proposed by Siepmann and Frenkel for polymer systems [64]. We will describe the method below. When we have already inserted $i-1$ small particles, we will attempt to insert the ith particle.

- For all k lattice sites that become free after displacement of a large particle, the external Boltzmann factor $\exp(-\beta u_{\mathbf{w}_i})$ for inserting a small particle on that lattice point will be computed. The external energy is the energy of the small particle due to interaction with all the large and small particles in the system. For hard-core particles, this Boltzmann factor is either zero in the case of overlap, or one when there is no overlap with other particles.

- One of the k lattice sites, say $\mathbf{w}_i$, is selected with a probability

$$P_{\mathbf{w}_i} = \frac{\exp(-\beta u_{\mathbf{w}_i})}{Z_{\{\mathbf{w}\}_i}} \qquad (6.8)$$

with

$$Z_{\{\mathbf{w}\}_i} = \sum_{j=1}^{k} \exp(-\beta u_{\mathbf{w}_j}) \qquad (6.9)$$

The subscript $\{\mathbf{w}\}_i$ means that $\mathbf{w}_i$ is one of the k trial lattice sites, i.e., $\mathbf{w}_i \in \{\mathbf{w}\}_i$. The ith small particle will be inserted at this lattice point and the corresponding partial "Rosenbluth weight" will be stored.

$$\omega_i = \frac{Z_{\{\mathbf{w}\}_i}}{k} \qquad (6.10)$$

- These steps will be repeated until we have inserted all n small particles.

For the configurational-bias method, we used the detailed balance condition in the Metropolis form [61] to determine the probability of acceptance

$$\text{acc}(a \mid b) = \min\left(1, \frac{P_a/\exp(-\beta U_a)}{P_b/\exp(-\beta U_b)}\right) \tag{6.11}$$

where P_a and P_b are, respectively, the probabilities that the system is in the original conformation a and in the new conformation b, and U_a and U_b are the total energies of these two conformations. The probability that the system is found in the new conformation b is equal to the probability of inserting the n small particles into the free volume

$$P_b = \prod_{i=1}^{n} \frac{\exp(-\beta u_{\mathbf{w}_{b_i}})}{Z_{\{\mathbf{w}\}_{b_i}}} \tag{6.12}$$

We can now write $U_b = \sum_{i=1}^{n} u_{\mathbf{w}_{b_i}} + u_{\mathbf{w}_{\text{large},b}} + u_{\mathbf{w}_{\text{rest}}}$, i.e., the external energy of the n reinserted small particles, the external energy of the replaced large particle and the rest of all the particles, that are not changed from position. Since the Rosenbluth factor is equal to

$$W_b = \prod_{i=1}^{n} \frac{Z_{\{\mathbf{w}\}_{b_i}}}{k} \tag{6.13}$$

we arrive at

$$P_b/\exp[-\beta U_b] = \left(\exp\left[-\beta(u_{\mathbf{w}_{\text{large},b}} + u_{\mathbf{w}_{\text{rest}}})\right] k^n W_b\right)^{-1} \tag{6.14}$$

Substitution of Eqn. 6.14 in Eqn. 6.11 gives

$$\text{acc}(a \mid b) = \min\left(1, \frac{W_b}{W_a}\exp\left[-\beta(u_{\mathbf{w}_{\text{large},b}} - u_{\mathbf{w}_{\text{large},a}})\right]\right) \tag{6.15}$$

Appendix B

For a faster equilibration of the polymer during the simulations, we regrow parts in the middle of the chain with a modified CBMC method [14]. In this case, we have to take care, that the end parts of the chain will be connected again. We shall first describe how we regrow a part in the middle of the chain within a modified Rosenbluth scheme. Then we shall decribe how to implement this in a CBMC scheme, such that detailed balance is satisfied.

1. Choose a part at random in the middle of the chain, say L segments, and remove this part.

2. Regrow this part of the chain segment by segment. When $i-1$ segments have already been grown, we try to add segment i. For all k possible directions of segment i we compute the external and the internal energies. Note that the number of trial directions k is equal to 6 on a cubic lattice. The external energy $\exp(-\beta u_{\mathbf{w}_i})$ is the energy of the trial segment due to interaction with the polymer and the solvent molecules. As we have only hard-core interactions in our system, the external energy is either zero for an unoccupied lattice site or infinity for an occupied one. The internal energy is equal to the number of ideal random walks $N_{\mathbf{w}_i}^{\mathbf{RW}}$ that connect the trial segment with the other end part of the chain in $L-i$ steps. This number can be calculated easily (see Appendix C of this chapter) and for the sake of efficiency we have tabulated these numbers. The role of this internal energy is to ensure that the end parts of the chain will be connected again.

3. Select one of the trial segments, say $\mathbf{w}_i$, with probability

$$P_{\mathbf{w}_i} = \frac{N_{\mathbf{w}_i}^{\mathbf{RW}} \exp(-\beta u_{\mathbf{w}_i})}{Z_{\{\mathbf{w}\}_i}} \tag{6.16}$$

where we have defined

$$Z_{\{\mathbf{w}\}_i} = \sum_{j=1}^{k} N_{\mathbf{w}_j}^{\mathbf{RW}} \exp(-\beta u_{\mathbf{w}_j}) \tag{6.17}$$

The subscript $\{\mathbf{w}\}_i$ means that $\mathbf{w}_i$ is one of the segments of the trial directions, i.e., $\mathbf{w}_i \in \{\mathbf{w}\}_i$. We add this segment to the chain and store the corresponding partial "Rosenbluth weight":

$$\omega_i = \frac{Z_{\{\mathbf{w}\}_i}}{k} \tag{6.18}$$

4. We repeat step 2 and 3 until the chain is connected again.

For the configurational-bias method, we used the detailed balance condition in the Metropolis form given by Eq. 6.11, where P_a and P_b are now, respectively, the probabilities that the part of the chain is in conformation a or b. The probability that the regrown part of the chain, consisting of L segments, has conformation b is equal to

$$P_b = \prod_{i=1}^{L} \frac{N_{\mathbf{w}_{b_i}}^{\mathbf{RW}} \exp(-\beta u_{\mathbf{w}_{b_i}})}{Z_{\{\mathbf{w}\}_{b_i}}} \tag{6.19}$$

As $U_b = \sum_{i=1}^{L} u_{\mathbf{w}_{b_i}}$ and the Rosenbluth factor is equal to

$$W_b = \prod_{i=1}^{L} \frac{Z_{\{\mathbf{w}\}_{b_i}}}{k} \tag{6.20}$$

we arrive at

$$P_b / \exp(-\beta U_b) = \frac{G_b}{k^L W_b} \tag{6.21}$$

with

$$G_b = \prod_{i=1}^{L} N_{\mathbf{w}_{b_i}}^{\mathbf{RW}} \tag{6.22}$$

Substitution of Eqn. 6.21 in Eqn. 6.11 gives

$$\mathrm{acc}\,(a \mid b) = \min\left(1, W_b G_b^{-1} / W_a G_a^{-1}\right) \tag{6.23}$$

In words, this modified configurational-bias Monte Carlo (CBMC) scheme works as follows

1. Generate a trial conformation for the selected part of the chain by using the Rosenbluth scheme, as described above.

2. Compute the Rosenbluth weights times the weightfunctions

$$W_{\mathrm{old}} G_{\mathrm{old}}^{-1} \text{ and } W_{\mathrm{trial}} G_{\mathrm{trial}}^{-1}$$

   of the trial conformation and of the old conformation.

3. Accept the trial move with probability

$$\min\left(1, W_{\mathrm{trial}} G_{\mathrm{trial}}^{-1} / W_{\mathrm{old}} G_{\mathrm{old}}^{-1}\right)$$

Appendix C

The number of ideal random walks from lattice point $(0,0,0)$ to lattice point $(\Delta x, \Delta y, \Delta z)$ in N steps can be computed as follows: we start with the expression for the number of possible ideal random walks consisting of N steps with a fixed number of steps in all directions

$$N^{\mathrm{RW}}(x, \bar{x}, y, \bar{y}, z, \bar{z}; N) = \frac{N!}{x!\, \bar{x}!\, y!\, \bar{y}!\, z!\, \bar{z}!} \qquad (6.24)$$

The number of steps in the positve x, y, and z-directions are given by x, y, and z, while $\bar{x}$, $\bar{y}$, and $\bar{z}$ are the number of steps in the negative directions. Note that the sum of all steps must be equal to N

$$x + \bar{x} + y + \bar{y} + z + \bar{z} = N \qquad (6.25)$$

To obtain the required number of ideal random walks from $(0,0,0)$ to $(\Delta x, \Delta y, \Delta z)$, we have to sum over the number of random walks with N steps with all possible values of $x, \bar{x}, y, \bar{y}, z$, and $\bar{z}$, subject to the constraints that

$$\begin{aligned}
\Delta x &= x - \bar{x} \\
\Delta y &= y - \bar{y} \\
\Delta z &= z - \bar{z}
\end{aligned} \qquad (6.26)$$

The number of ideal random walks of N steps resulting in displacements Δx, Δy, and Δz in the x, y, and z-directions then reduces to

$$N^{\mathrm{RW}}(\Delta x, \Delta y, \Delta z; N) =$$

$$\sum_{\bar{x}=0}^{N^- - \bar{y}} \sum_{\bar{y}=0}^{N^-} \frac{N!}{\bar{x}!\, (\bar{x}+\Delta x)!\, \bar{y}!\, (\bar{y}+\Delta y)!\, (N^- - \bar{x} - \bar{y})!\, (N^+ - \bar{x} - \bar{y})!} \qquad (6.27)$$

with $N^- = (N - \Delta x - \Delta y - \Delta z)/2$ and $N^+ = (N - \Delta x - \Delta y + \Delta z)/2$.

REFERENCES

1. J.C. MAXWELL, Phil.Mag.[4], **19**, 19, (1860).
2. J.C. MAXWELL, Phil.Mag.[4], **20**, 21, (1860).
3. L. BOLTZMANN, Wien. Ber., **66**, 275, (1872).
4. J.W. GIBBS, "*Thermodynamische Studien*", Engelmann, Leipzig, (1902).
5. S.N. BOSE, Zeit. für Phys., **26**, 178, (1924).
6. A. EINSTEIN, Sitzungsberichte der Preussischen Akademie der Wissenschaften, 261, (1924).
7. E. FERMI, Zeit. für Phys., **36**, 902, (1926).
8. P.A.M. DIRAC, Proc. Roy. Soc. of London, Ser. A, **112**, 661, (1926).
9. P. DEBYE and E. HÜCKEL, Zeit. für Phys., **24**, 185, (1923).
10. P. LANGEVIN, J. de Physique, **4**, 678, (1905).
11. P. DEBYE, Phys. Zeit., **13**, 97, (1912).
12. L. BRILLOUIN, J. de Physique, **8**, 74, (1927).
13. W. HEISENBERG, Zeit. für Physik, **49**, 619, (1928).
14. J.D. VAN DER WAALS, "*Ph.D. Thesis*", Hoogeschool te Leiden, The Netherlands, (1873).
15. L.S. ORNSTEIN and F. ZERNIKE, Proc. Akad. Sci.(Amsterdam), **17**, 793, (1914).
16. J. YVON, "*La Théorie Statistique des Fluides et l'Equation d'Etat*", Actualités Scientifiques et Industrielles, Hermann, Paris, **203**, (1935).
17. J.G. KIRKWOOD, J. Chem. Phys., **3**, 300, (1935).
18. N.N. BOGOLYUBOV, J. Phys. USSR, **10**, 257, (1946).
19. M. BORN and M.S. GREEN, "*A General Kinetic Theory of Liquids*", Cambridge University Press, Cambridge, (1949).
20. L. ONSAGER, Phys. Rev., **62**, 558, (1942).
21. L. ONSAGER, Ann. N.Y. Acad. Sci., **51**, 627, (1949).
22. W. KUHN, Kolloid Z., **68**, 2, (1934).
23. P.J. FLORY, J. Chem. Phys., **9**, 660, (1941).
24. P.J. FLORY, J. Chem. Phys., **10**, 51, (1942).
25. H.B. CALLEN, "*Thermodynamics and an Introduction to Thermostatistics*", John Wiley & Sons, Singapore, (1985).
26. W.W. WOOD and J.D. JACOBSON, J. Chem. Phys., **27**, 1207, (1957).
27. B.J. ALDER and T.E. WAINWRIGHT, J. Chem. Phys., **27**, 1208, (1957).
28. J.K. PERCUS, "*The Many-Body Problem*", Interscience, New York, (1963).
29. B.J. ALDER and T.E. WAINWRIGHT, Phys. Rev. A, **1**, 18, (1970).

30. F. REINITZER, Monatsh. Chem., **9**, 421, (1888).
31. P.S. PERSHAN, "*Structure of Liquid Crystal Phases*", Singapore: World Scientific, (1988).
32. D. FRENKEL, B.M. MULDER, and J.P. MCTAGUE, Phys. Rev. Lett., **52**, 287, (1984).
33. D. FRENKEL and B.M. MULDER, Mol. Phys., **55**, 1171, (1985).
34. D. FRENKEL, J. Phys. Chem. (erratum:**92**, 5314 (1988)), **91**, 4912, (1987).
35. D. FRENKEL, Mol. Phys., **60**, 1, (1987).
36. D. FRENKEL, J. Phys. Chem. (erratum:**92**, 5314 (1988)), **92**, 3280, (1988).
37. D. FRENKEL, H.N.W. LEKKERKERKER, and A. STROOBANTS, Nature, **332**, 882, (1988).
38. D. FRENKEL, Liq. Cryst., **5**, 929, (1989).
39. M.P. ALLEN, D. FRENKEL, and J. TALBOT, Comput. Phys. Rep., **9**, 301, (1989).
40. J.A.C. VEERMAN and D. FRENKEL, Phys. Rev. A, **41**, 3237, (1990).
41. G.J. VROEGE and H.N.W. LEKKERKERKER, Rep. Prog. Phys., **55**, 1241, (1992).
42. A.R. KHOKHLOV and A.N. SEMENOV, Physica A, **108**, 546, (1981).
43. A.R. KHOKHLOV and A.N. SEMENOV, Physica A, **112**, 605, (1982).
44. J.P. HANSEN and I.R. MCDONALD, "*Theory of Simple Liquids*", 2nd edition, London: Academic Press, (1986).
45. J.E. MAYER and M.G. MAYER, "*Statistical Mechanics*", John Wiley, New York, (1977).
46. F.C. BAWDEN, N.W. PIRIE, J.D. BERNAL, and I. FANKUCHEN, Nature, **138**, 1051, (1936).
47. O. KRATKY and G. POROD, Rec. Trav. Chim., **68**, 1106, (1949).
48. H. YAMAKAWA, "*Modern Theory of Polymer Solutions*", Harper & Row, (1971).
49. H. YAMAKAWA, Ann. Rev. Phys. Chem., **35**, 23, (1984).
50. T. ODIJK, Macromolecules, **16**, 1340, (1983).
51. T. ODIJK, Macromolecules, **19**, 2313, (1986).
52. W. HELFRICH and W. HARBICH, Chem. Scr., **25**, 32, (1985).
53. I.M. LIFSHITZ, Z. Eksp. Teor. Fiz. (Sov.Phys.-JETP **28** 1280), **55**, 2408, (1969).
54. I.M. LIFSHITZ, A. YU GROSBERG, and A.R. KHOKHLOV, Rev. Mod. Phys., **50**, 683, (1978).
55. R. HENTSCHKE, Macromolecules, **23**, 1192, (1990).
56. K.F. FREED, Adv. Chem. Phys., **22**, 1, (1972).
57. R.P. FEYNMAN and A.R. HIBBS, "*Quantum Mechanics and Path Integrals*", McGraw-Hill, New York, (1965).
58. M. WARNER, J.M.F. GUNN, and A.B. BAUMGÄRTNER, J. Phys. A: Math. Gen., **18**, 3007, (1985).
59. W. HELFRICH, Z. Naturforsch. A, **33**, 305, (1978).
60. W. HELFRICH and R.M. SERVUSS, Nuovo Cimento D, **3**, 137, (1984).
61. D. FRENKEL, G.C.A.M. MOOIJ, and B. SMIT, J. Phys.: Condens. Matter, **3**, 3053, (1991).
62. H. YAMAKAWA and M. FUJII, J. Chem. Phys, **59**, 6641, (1973).
63. B. WIDOM, J. Chem. Phys., **39**, 2808, (1963).
64. J.I. SIEPMANN and D. FRENKEL, Mol. Phys., **75**, 59, (1992).
65. X. AO, A. WEN, and R.B. MEIJER, Physica A, **176**, 63, (1991).
66. G.M. TORRIE and J.P. VALLEAU, J. Comp. Phys., **23**, 187, (1977).

67. P.J. FLORY, Proc. R. Soc. London, Ser. A, **234**, 60, (1956).

68. E.A. DIMARZIO, J. Chem. Phys., **36**, 1563, (1962).

69. P.J. FLORY and G. RONCA, Mol. Cryst. Liq. Cryst., **54**, 289, (1979).

70. G. RONCA, J. Polym. Sci. Pt. B, **27**, 1795, (1989).

71. J.F. NAGLE, Proc. R. Soc. London, Ser. A, **337**, 569, (1974).

72. A. MALAKIS, J. Phys. A, **13**, 651, (1980).

73. A. BAUMGÄRTNER, J. Chem. Phys., **84**, 1905, (1986).

74. A. KOLINSKY, J. SKOLNICK, and R. YARIS., Macromolecules, **19**, 2560, (1986).

75. A.L. RODRIGUEZ, H.P. WITTMANN, and K. BINDER, Macromolecules, **23**, 4327, (1990).

76. R. DICKMAN, Computational Polym. Sci., **1**, 206, (1991).

77. Z.Y. CHEN, Phys. Rev. Lett., **71**, 93, (1993).

78. M.P. ALLEN and D.J. TILDESLEY, "*Computer Simulations of Liquids*", Clarendon, Oxford, (1987).

79. D. FRENKEL and R. EPPENGA, Phys. Rev A, **31**, 3, (1985).

80. D. FRENKEL and A.A. LOUIS, Phys. Rev. Lett., **68**, 3363, (1992).

81. M. DIJKSTRA, D. FRENKEL, and H.N.W. LEKKERKERKER, Physica A, **193**, 374, (1993).

82. C.H. BENNETT, J. Comput. Phys., **22**, 245, (1976).

83. R. EPPENGA and D. FRENKEL, Mol. Phys., **52**, 1303, (1984).

84. M.P. ALLEN and D. FRENKEL, Phys. Rev. A, **37**, 1813, (1988).

85. M.P. ALLEN and D. FRENKEL, Phys. Rev. A, **42**, 3641, (1990).

86. S. OSTLUND and B.I. HALPERIN, Phys. Rev. B, **23**, 335, (1981).

87. J.V. SELINGER and R.F. BRUINSMA, Phys. Rev. A, **43**, 2910, (1991).

88. M.R. WILSON and M.P. ALLEN, Mol. Phys., **2**, 277, (1993).

89. G. LASHER, J. Chem. Phys., **53**, 4141, (1970).

90. R.F. KAYSER and H.J. RAVECHÉ, Phys. Rev. A, **17**, 2067, (1978).

91. H.N.W. LEKKERKERKER, PH. COULON, R. VAN DER HAEGEN, and R. DEBLIECK, J. Chem. Phys., **80**, 3427, (1984).

92. G.J. VROEGE and T. ODIJK, Macromolecules, **21**, 2848, (1988).

93. S.J. LEE, J. Chem. Phys., **87**, 4972, (1987).

94. R. HENTSCHKE and J. HERZFELD, Phys. Rev. A, **44**, 1148, (1991).

95. D.A. KOFKE, Mol. Phys., **78**, 1331, (1993).

96. D.A. KOFKE, J. Chem. Phys., **98**, 4149, (1993).

97. W.H. PRESS, B.P. FLANNERY, S.A. TEUKOLSKY, and W.T. VETTERLING, "*Numerical Recipes in Fortran*", Cambridge University Press, New York, (1992).

98. M.P. ALLEN, G.T EVANS, D. FRENKEL, and B.M. MULDER, "*Advances in Chemical Physics, Volume LXXXVI*", John Wiley & Sons, Inc., Cambridge, **9**, 301, (1989).

99. J.S. ROWLINSON and F. SWINTON, "*Liquids and Liquid Mixtures*", Butterworths Scientific Publications, London, (1982).

100. M.L. HUGGINS, J.Phys.Chem., **46**, 151, (1942).

101. T.W. MELNYK and B.L. SAWFORD, Mol. Phys., **29**, 891, (1975).

102.   D.J. ADAMS and I.R. MCDONALD, J. Chem. Phys., **63**, 1900, (1975).

103.   V. EHRENBERG, H.M. SCHAINK, and C. HOHEISEL, Physica A, **169**, 365, (1990).

104.   J.L. LEBOWITZ and J.S. ROWLINSON, J. Chem. Phys., **41**, 133, (1964).

105.   E.B. SMITH and K.R. LEA, Trans. Faraday Soc., **59**, 1535, (1963).

106.   B.J. ALDER, J. Chem. Phys., **40**, 2724, (1964).

107.   A. ROTENBERG, J. Chem. Phys., **43**, 4377, (1965).

108.   P.H. FRIES and J.P. HANSEN, Mol. Phys., **48**, 891, (1983).

109.   G. JACKSON, J.S. ROWLINSON, and F. VAN SWOL, J. Phys. Chem., **91**, 4907, (1987).

110.   T. BIBEN and J.P. HANSEN, Phys. Rev. Lett., **66**, 2215, (1991).

111.   H.N.W. LEKKERKERKER and A. STROOBANTS, Physica A, **195**, 387, (1993).

112.   T. BIBEN, "*Ph.D. Thesis*", Université Claude Bernard-Lyon 1, France, (1993).

113.   T.R. KIRKPATRICK, J.Chem.Phys., **85**, 3515, (1986).

114.   W.G. HOOVER and A.G. DE ROCCO, J.Chem.Phys., **36**, 3141, (1962).

115.   W.G. HOOVER and J.C. POIRIER, J.Chem.Phys., **38**, 327, (1963).

116.   T. BIBEN and J.P. HANSEN, Europhys. Lett., **12**, 347, (1990).

117.   I.C. SANCHEZ, Macromolecules, **24**, 908, (1991).

118.   K.F. FREED and M.G. BAWENDI, J. Phys. Chem., **93**, 2194, (1989).

119.   A. HARIHARAN and S.K. KUMAR, J. Chem. Phys., **99**, 4041, (1993).

120.   A. YETHIRAJ and R. DICKMAN, J. Chem. Phys., **97**, 4468, (1992).

Samenvatting

De meeste materialen, die wij in de chemie en de fysica bestuderen, bestaan uit heel veel moleculen. Een liter water bevat al gauw 10^{25} moleculen. Het is dus ondoenlijk om alle deeltjes afzonderlijk te bekijken en volstrekt onmogelijk om de fysische eigenschappen van een vloeistof met pen en papier uit te rekenen. Reeds in de achttiende eeuw was het bekend dat een systeem met slechts 3 deeltjes al niet exact geanalyseerd kon worden. Gelukkig kreeg men in de jaren vijftig, het begin van het computertijdperk, de beschikking over een methode waarmee we een systeem met veel deeltjes uitstekend konden bestuderen, nl. computersimulaties.

In een computersimulatie proberen we de *echte* wereld na te bootsen. We maken eerst een model van het systeem dat we willen bestuderen en we vertellen dan de computer welke fysische wetten er gelden. Door middel van de computer laten we nu alle moleculen kris kras door elkaar bewegen afhankelijk van enkele opgelegde grootheden, zoals de temperatuur of druk. We kunnen nu het systeem bij deze opgelegde grootheden bestuderen en zo iets meer te weten komen over de macroscopische toestand van het systeem, bijv. of het vloeibaar of vast is.

Op school leren we al dat moleculen in een vaste stof netjes gerangschikt zijn, terwijl ze in een vloeistof kris kras door elkaar bewegen. We zeggen: vloeistoffen zijn ongeordend en vaste stoffen zijn geordend. De natuurkunde kwantificeert de mate van wanorde met het begrip entropie: gewoonlijk is de entropie groot als de wanorde groot is. Het is een ervaringsfeit, verwoord in de tweede hoofdwet der thermodynamica, dat processen zonder invloed van buitenaf alleen plaatsvinden indien de entropie (lees: wanorde) hierbij toeneemt. Denk hierbij aan een bureau, waarop de wanorde alleen maar toeneemt.

Een ander ervaringsfeit is dat systemen de neiging hebben om zo weinig mogelijk energie te bezitten. Een baksteen, losgelaten vanaf 1 meter boven de grond, zal naar beneden vallen, omdat zijn energie op de grond kleiner is dan op de oorspronkelijke hoogte. De combinatie van deze twee ervaringsfeiten leert ons nu dat een systeem de neiging heeft om zijn energie te minimaliseren en tegelijkertijd zijn entropie te maximaliseren. Vaak zijn deze twee 'doelstellingen' niet tegelijkertijd te verwezenlijken. Er is dan sprake van een competitie tussen energieminimalisatie en entropiemaximalisatie, waarbij soms de entropie 'wint' en soms de energie. Het bekendste voorbeeld van zo'n

competitie is misschien wel het bevriezen van water tot ijs. Bij temperaturen boven $0°C$
wint de entropie, zodat we een wanordelijke vloeistof hebben, onder het vriespunt wint
de energie en hebben we een geordende vaste stof, waarvan de energie laag is. Althans,
dit is het beeld dat alle gangbare theorieën, die dit vriesproces beschrijven, schetsen.
Deze door de temperatuur gedreven overgang van water naar ijs gaat dus gepaard met
een (grote) energie afname, veroorzaakt door de onderlinge aantrekking of afstoting van
de deeltjes, en een (kleine) entropie afname (zichtbare orde groter). Het feit dat de
entropie niet meer maximaal is, wordt ruimschoots gecompenseerd door de zeer lage
energie van het ijs.

Het feit dat de energie van het ijs kleiner is dan die van het water heeft direct te
maken met de aantrekkende en afstotende krachten die de watermoleculen op elkaar
uitoefenen. Men heeft dan ook erg lang verondersteld dat aantrekking of afstoting van
de moleculen essentieel is voor bevriezing. Het was daarom ook zeer verrassend dat
er in 1957 een overgang gevonden werd van een ongeordende ('vloeibare') naar een
geordende ('vaste') toestand in computersimulaties van harde bollen ('biljartballen'),
die elkaar niet aantrekken of afstoten. In tegenstelling tot de water-ijs overgang, die
door de temperatuur gedreven wordt, wordt de overgang in het harde bollen systeem
gedreven door de dichtheid. Bij lage dichtheden vinden we een vloeistof, bij hoge
dichtheden een vaste stof. Een tweede verschil met de water-ijs overgang is dat door
de afwezigheid van onderlinge deeltjes interacties de bevriezing van de biljartballen
niet toegeschreven kan worden aan een enorme energie afname gecombineerd met een
kleine entropie toename. De enig overgebleven verklaring is nu dat de entropie van de
geordende biljartballen groter is dan die van de ongeordende biljartballen. In andere
woorden: bij hoge dichtheid is de entropie van de geordende toestand groter dan die van
de ongeordende toestand.

Hoe is dit in overeenstemming te brengen met onze eerdere definitie van entropie
als maat voor de hoeveelheid *wanorde*? Het blijkt dat ons intuïtief begrip van de relatie
tussen wanorde en entropie niet toereikend meer is. Een betere definitie van entropie is
afkomstig van Boltzmann (1872). Deze zegt dat de entropie een maat is voor het aantal
microtoestanden. Een microtoestand is één specifieke rangschikking van de moleculen.
Als een systeem in veel microtoestanden kan zitten, hebben we weinig gedetailleerde
kennis van het systeem en is de wanorde groot. In het algemeen zal een vloeistof veel
microtoestanden hebben: molecuul A kan 'overal' zitten, zo ook B en C etc. In een
vaste stof, daarentegen, moeten A, B, C etc. netjes geordend op een rooster zitten,
hetgeen op veel minder manieren gerealiseerd kan worden, zodat de entropie klein is.
Tot zo ver is de definitie van Boltzmann dus consistent met onze intuïtie betreffende
wanorde. Echter, wanneer de dichtheid van harde bollen voldoende groot is, is toch het

aantal microtoestanden van de geordende toestand groter dan die van de ongeordende toestand. Dit is aan de hand van Fig. s.1 in te zien. In de ongeordende vloeistof fase, waar alle moleculen kris kras door elkaar zitten, zullen alle moleculen elkaar in de weg zitten. Er is geen beweging meer mogelijk. Echter als alle moleculen netjes geordend zitten, zoals in de vaste toestand, kunnen alle bollen nog net een beetje bewegen. Er zijn dan meer microtoestanden voor het systeem mogelijk en de entropie en de wanorde is daardoor bij deze dichtheid groter. Dit lijkt vreemd, want er kan dus een geordende toestand verkregen worden doordat deze in feite meer wanorde bevat. De toename in wanorde onstaat doordat de moleculen in deze toestand meer kunnen bewegen, wat ze erg prettig vinden.
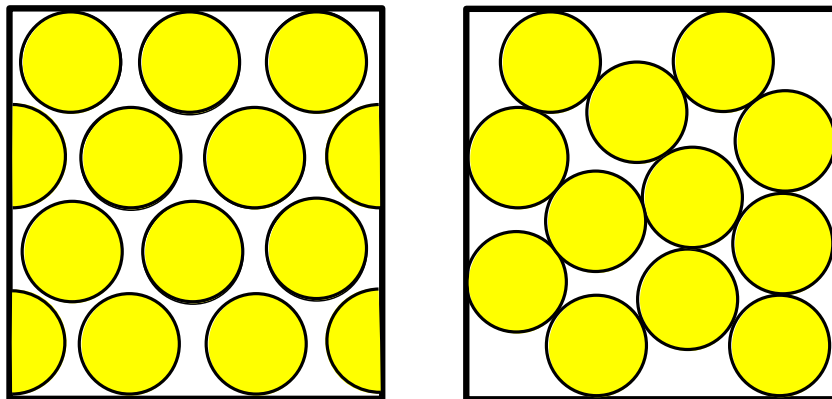

FIGURE 6.11 Schematische representatie van een vaste stof (links) en een vloeistof (rechts). Links kunnen alle moleculen nog een beetje bewegen. Rechts zitten alle moleculen elkaar in de weg.

Twee elementen uit de voorgaande discussie over ijs, water, orde en wanorde zijn van belang voor de inhoud van dit proefschrift. Op de eerste plaats is nu aangetoond dat computersimulatie inderdaad een belangrijke rol kan spelen in de bestudering van systemen met veel deeltjes. Het tweede belangrijke element is het verkregen extra *inzicht* in het aloude begrip entropie. Doordat we nu weten dat bevriezing niet persé veroorzaakt hoeft te worden door het minimum energie principe, maar ook veroorzaakt kan worden door het maximum entropie principe, is het de moeite waard geworden om te kijken naar de invloed van entropie op andere vormen van ordening die we in de natuur tegen kunnen komen. Immers, bevriezing is maar één van de mogelijkheden waarop een systeem kan ordenen. In dit proefschrift hebben we twee andere vormen

van orde bestudeerd, nl. orde die ontstaat doordat langwerpige moleculen evenwijdig aan elkaar gaan staan en orde veroorzaakt doordat moleculen van verschillende grootte ontmengen. Beide ordeningsprocessen zijn zowel fundamenteel als industrieel relevant, zoals we hieronder zullen aangeven. Tevens zijn beide vormen van orde, net als in het geval van bevriezing, meestal beschreven met het minimum energie principe en niet met het maximum entropie principe. In dit proefschrift laten we zien dat ook het maximum entropie principe gebruikt kan worden om deze ordeningsverschijnselen te verklaren.

De eerste vorm van orde die we bestudeerd hebben is oriëntatie orde (zie Fig. 2.1). Deze vorm van orde treedt op wanneer we langwerpige deeltjes bekijken, zeg maar sigaren in plaats van bollen. Als we heel weinig van deze langwerpige moleculen in een grote doos stoppen, wat overeenkomt met een lage dichtheid, kunnen we de deeltjes kris kras door elkaar leggen. Bij vergroting van de dichtheid van zo'n systeem is het voordeliger om alle deeltjes in één richting te leggen. De langwerpige moleculen liggen nu evenwijdig aan elkaar en we hebben dan te maken met een zogenaamde 'nematische fase'. Bij verdere vergroting van de dichtheid gaan de moleculen evenwijdig aan elkaar in laagjes zitten ('smectische fase'). Bij zeer grote dichtheid wordt weer een vaste, kristallijne fase gevormd. Deze nematische en smectische fasen zitten dus tussen de vloeibare en de vaste fase in en worden daarom ook wel vloeibaar kristallijn genoemd. Vloeibare kristallen zijn technologisch relevant omdat ze voorkomen in de zgn. LCD's (Liquid Crystal Displays), die veelvuldig gebruikt worden in horloges, rekenmachines etc. Als de moleculen in een ongeordende toestand zitten laten ze licht door. We zien dan geen cijfertje op het display. Als de moleculen nu geordend worden met een electrische veld, kan het licht er niet door heen en er verschijnt een donker cijfertje op het scherm. Er is al erg veel onderzoek gedaan naar het gedrag van langwerpige moleculen. Hierbij is de invloed van de buigzaamheid van de moleculen meestal buiten beschouwing gelaten. Echter, in de natuur zijn de meeste lange moleculen, ook wel polymeren genoemd, altijd enigszins flexibel. In dit proefschrift staat beschreven hoe de flexibiliteit van de polymeren de oriëntatie orde beïnvloedt. Men kan zich eenvoudig voorstellen dat flexibele polymeren, die enigszins op kluwentjes wol lijken, veel moeilijker te ordenen zijn dan hun minder flexibele soortgenoten. Of anders: ongekookte spaghetti is veel eenvoudiger evenwijdig neer te leggen dan gekookte. In fysische termen betekent dit dat het relatief veel energie kost om een nematische fase te maken van zeer flexibele moleculen. Als eerste aanzet van het onderzoek hebben we in hoofdstuk 3 gekeken hoeveel energie het nu kost om één flexibel polymeer in een smalle rechte buis te stoppen (zie Fig. 3.1). Dit is natuurlijk afhankelijk van de dikte van de buis en de flexibiliteit van het polymeer. Hoe dikker de buis, hoe gemakkelijker het is om een polymeer er in te krijgen. Zeer flexibele polymeren zijn moeilijk in het gareel te houden en het zal dus veel

energie kosten om deze in een buis te krijgen. Onze simulatieresultaten kwamen goed overeen met de bestaande theorieën. De volgende stap van het onderzoek, beschreven in hoofdstuk 4, is de bestudering van de invloed van de flexibiliteit op de oriëntatie ordening in een 2-dimensionaal polymeer systeem. Dus bijv. een systeem met stukjes draad, die we op tafel willen leggen zonder dat ze over elkaar heen gaan liggen (zie Fig. 4.8 en 4.9). In het verleden is er, ondanks enkele pogingen, nooit iemand in geslaagd om in computersimulaties van polymeren in 2 dimensies oriëntatie orde te vinden. In onze computersimulaties laten wij wel oriëntatie orde zien voor niet te flexibele polymeren. Bovendien waren we in staat elastische constanten te meten, die bleken te voldoen aan theoretisch voorspelde schaalwetten. De ontwikkelde technieken hebben we uiteindelijk gebruikt in hoofdstuk 5 bij de bestudering van flexibele polymeren in 3 dimensies (zie Fig. 5.7). De resultaten van onze simulaties wijzen uit dat de bestaande theorieën ontoereikend zijn.

De tweede klasse van ordeningsverschijnselen die we hebben bekeken is ontmenging van mengsels. Lange tijd was het onduidelijk wat de oorzaak was van ontmenging. Als je bijv. olie op water gooit, zal de olie niet met het water mengen, maar als een laagje er boven op blijven liggen. Komt dit nu omdat de watermoleculen en de oliemoleculen elkaar afstoten of omdat de watermoleculen elkaar aantrekken? Kennis van de oorzaken van ontmenging is technologisch relevant. De margarine industrie, bijvoorbeeld, is geïnteresseerd in de vraag hoeveel (goedkoop!) water ze in haar margarine kan stoppen zonder dat dit er bovenop komt te liggen. De verf industrie wil weten hoe ze homogene, goed gemengde en niet klonterende verf kan maken. Deze vragen hangen allemaal samen met de vraag hoe goed verschillende stoffen, dus verschillende moleculen, mengbaar zijn. In 1964 is dit fenomeen onderzocht aan de hand van een mengsel van grote en kleine harde bollen (biljartballen), die elkaar niet afstoten of aantrekken. De conclusie was dat grote en kleine bollen altijd in alle proporties mengbaar zijn. Dit komt wederom prima overeen met onze intuïtieve notie van maximum entropie: de wanorde is groot als alle bollen, groot en klein, door elkaar zitten. In 1991, echter, werden de resultaten van een hernieuwde studie naar dit systeem gepubliceerd. De auteurs van dit recente artikel laten zien dat ontmenging optreedt indien de grote bollen minstens 5 keer zo groot zijn als de kleine. Dit druist dus weer in tegen onze intuïtie van entropie. In een poging om uit te maken wie nu gelijk heeft, hebben wij computersimulaties gedaan aan soortgelijke systemen, waarbij we voor de eenvoud kubussen i.p.v. bollen beschouwd hebben. Wij vonden perfecte menging bij een grootte verhouding van 2. Echter, bij een grootte verhouding van 3 vonden we ontmenging in een gedeelte met veel grote en weinig kleine kubussen en een gedeelte met veel kleine en weinig grote kubussen. Net als in het geval van de bevriezing van het biljartballen systeem, druist deze ordening

(grote en kleine deeltjes 'netjes' gescheiden) in tegen onze notie van maximale entropie. Wederom blijkt, echter, dat de interpretatie van entropie als een maat voor het aantal microtoestanden een verklaring biedt voor dit ontmengingsfenomeen: hoewel de grote deeltjes samenklonteren en daarbij entropie verliezen, winnen de kleine deeltjes veel ruimte en daarmee entropie. Netto is de entropie winst voor de kleine deeltjes groter dan het verlies van de grote. Het systeem bezit dus meer microtoestanden wanneer het ontmengd is.

Samenvattend kunnen we zeggen dat we in dit proefschrift overgangen hebben bestudeerd van ongeordende naar geordende toestanden (lange moleculen netjes in één richting, grote en kleine deeltjes netjes gesorteerd). In de gebruikelijke beschrijvingen van zulke overgangen, gaat men uit van het minimum energie principe. De overgangen, die in dit proefschrift beschreven staan, vinden plaats doordat de totale entropie of wanorde van de nieuwe toestand groter is. De nieuwe toestand lijkt globaal meer geordend, maar als we in meer detail kijken, zien we dat de moleculen in deze toestand meer ruimte hebben om te bewegen. Er zijn dus meer microtoestanden van het systeem mogelijk en de entropie is daardoor groter. Kortom we kunnen dus orde krijgen door wanorde.

NAWOORD

In dit nawoord zal ik heel anders dan gebruikelijk, niet beginnen met het bedanken van mijn promotor Daan Frenkel, maar zal ik eerst verder terug gaan in de tijd. Dat dit proefschrift tot stand is gekomen is nogal verbazingwekkend, gezien de vele mensen die er in het verleden op tegen waren dat ik natuurkunde ging studeren. Allereerst werd ik op de middelbare school volledig ontmoedigd door mijn natuurkundeleraar, die de vergelijking maakte met een amateurvoetballer die profvoetballer wilde worden. Na het eerste jaar in Wageningen raadde de faculteit natuur- en sterrenkunde in Utrecht het me ten zeerste af, omdat natuurkunde in de verste verte niet leek op koeien melken of landbouwgrondbewerking. Toch zette ik na het derde jaar het plan door om voor een jaar natuurkundevakken te gaan volgen in Utrecht. Echter dit maal gaf de vakgroep natuur- en weerkunde in Wageningen mij geen toestemming, aangezien men vond dat ik die vakken door zelfstudie wel in Wageningen kon doen. In Utrecht waren de meningen erg verdeeld over mijn komst. Sommigen wilden me meteen terug sturen, anderen waren erg verrast door het tempo waarin ik alle vakken afliep. Het buro inschrijving was echter om financiële redenen niet blij en wilde me dan ook niet aan de universiteit inschrijven. Al mijn tentamens, die ik inmiddels had gedaan, waren hierdoor ongeldig. Het heeft 18 maanden geduurd voordat ik als student erkend werd. Toch kon dit mijn enthousiasme voor de natuurkunde niet verminderen, en ik besloot ook deze studie af te maken. Door Liesbeth ben ik gestimuleerd om mijn afstudeervak natuurkunde op het Amolf te doen. Frans Saris en Daan Frenkel hadden zoveel vertrouwen in mij, dat zij me meteen als onderzoeker in opleiding aannamen. Het heeft mij uiteindelijk zeer verbaasd dat ik in de tijd van de 'kies exact' campagnes toch veel weerstand heb ondervonden om een studie natuurkunde te volbrengen.

Ik wil hier allen bedanken, die mij geholpen en gesteund hebben op mijn weg naar Amolf. Met name wil ik hierbij mijn ouders noemen, die altijd achter mijn beslissingen gestaan hebben. Verder wil ik dhr. M.A. Hemminga, dhr. W. Norde, mevr. A. Arnoldussen, dhr. T.J. Hollander, dhr. A. v.d. Vegt en Frans Saris bedanken, die mij indirect of direct bij het voltooien van mijn studies veel geholpen hebben en tevens veel vertrouwen in mij hadden.

Vervolgens wil ik nu mijn promotor Daan Frenkel bedanken. Zijn continue stroom van altijd goede ideeën en zijn gave om de fysica met simpele voorbeelden en of

tekeningen duidelijk te maken heb ik altijd zeer bewonderd. Ik beschouw het als een voorrecht om met een wetenschapper van zijn formaat samengewerkt te hebben. Verder wil ik Henk Lekkerkerker bedanken voor zijn hulp bij mijn promotie onderzoek. Zijn kritische kanttekeningen, maar vooral zijn belangstelling en enthousiasme heb ik altijd zeer stimulerend gevonden.

I also like to thank Jean-Pierre Hansen for my stay at the "Ecole Normale Supérieure de Lyon". In these months, I have learned a lot about simple fluids. I always enjoyed our bilingual discussions, for which he was never too busy.

Verder wil ik mijn groep bedanken met name Ali, Bela, Evert Jan, Germonda, José, Liesbeth, Maarten, Maria, Martin, Matthew, Paulo, Peter (3 ×), Pierluigi, Pieter Rein, Ronald en Thierry voor de plezierige werksfeer. Ook de buitenwerktijdse activiteiten, zoals de (zeil)weekenden etc., heb ik altijd erg leuk gevonden. Als laatste wil ik René noemen, omdat zijn enthousiasme voor de statistische fysica en computersimulaties mij hebben gestimuleerd deze richting van de natuurkunde in te gaan. Maar vooral bedank ik hem voor zijn onontbeerlijke steun, die hij mij al die jaren heeft gegeven.

CURRICULUM VITAE

Op 26 september 1967 ben ik geboren te 's-Gravenhage. Na het behalen van het Atheneum-B diploma ben ik in september 1985 begonnen met de studie Moleculaire Wetenschappen aan de Landbouwuniversiteit Wageningen. Ik behaalde in september 1986 het propaedeutisch examen (Cum Laude). In september 1988 begon ik met de studie Natuurkunde aan de Rijksuniversiteit Utrecht. Het propaedeutische examen Natuurkunde werd in augustus 1989 behaald. In het kader van het afstudeerwerk Moleculaire Wetenschappen, heb ik onder leiding van Dr. E.E. van Faassen en Dr. G. van Ginkel onderzoek verricht naar de invloed van Gramicidine A op lipide systemen met behulp van electronspinresonantie. Het doctoraalexamen in de Moleculaire Wetenschappen legde ik af op 25 juni 1990. In september 1990 ben ik als onderzoeker in opleiding begonnen op het FOM-Instituut voor Atoom- en Molecuulfysica. In de groep van Prof. dr. D. Frenkel heb ik in het kader van mijn afstudeerscriptie Natuurkunde, computerberekeningen gedaan aan de snelheidsautocorrelatiefunctie in een vier-dimensionaal roostergasmodel en tevens computersimulaties van semiflexibele polymeren. Het doctoraalexamen Natuurkunde is afgelegd op 26 augustus 1991. Vervolgens ben ik met mijn promotieonderzoek begonnen, waarvan de resultaten beschreven zijn in dit proefschrift. Gedurende deze periode heb ik 3 maanden doorgebracht aan de "Ecole Normale Supérieure de Lyon", waar ik samengewerkt heb met Prof. dr. J.P. Hansen.